ABSTRACT

EXTENSION TO PV OPTICS TO INCLUDE FRONT ELECTRODE DESIGN IN SOLAR CELLS

by
Debraj Guhabiswas

Proper optical designing of solar cells and modules is of paramount importance towards achieving high photovoltaic conversion efficiencies. Modeling softwares such as *PV OPTICS*, *BIRANDY* and *SUNRAYS* have been created to aid such optical designing of cells and modules; but none of these modeling packages take the front metal electrode architecture of a solar cell into account

A new model, has been developed to include the front metal electrode architecture to finished solar cells for optical calculations. This has been implemented in C++ in order to add a new module to PV OPTICS (NREL's photovoltaic modeling tool) to include front metallization patterns for optical design and simulation of solar cells. This new addition also calculates the contribution of light that diffuses out of the illuminated (non-metallized) regions to the solar cell current. It also determines the optical loss caused by the absorption in the front metal and separates metallic losses due to front and back contacts. This added capability also performs the following functions:

- calculates the total current that can be generated in a solar cell due to optical absorption in each region, including the region beneath the front metal electrodes for the radiation spectrum of AM 1.5,
- calculates various losses in the solar cell due to front electrode shading, metal absorption, and reflectance,
- makes a plot of how light is absorbed in the metal as well as silicon under the shaded region in the solar cell.

Although Finite Difference Time Domain (FDTD) is the numerical technique of choice to solve Maxwell's equations for a propagating electromagnetic wave, it is both time consuming and very demanding on the computer processors. Furthermore, for complicated geometric structures, FDTD poses various limitations. Hence, ray tracing has been chosen as the means of implementing this new model.

This new software has been used to carry out a detailed investigation on the effect of various parameters of the front electrode architecture on the performance of alkaline anisotropically texture etched (100) oriented single crystal silicon solar cells. These parameters include:

- the thickness of the silicon absorber layer,
- the texture height,
- width of the front metal fingers,
- height of the front metal fingers, and
- the effect of encapsulation of a solar cell in a module.

The results show that the front metal architecture used in commercial silicon solar cells has minimal effect on its performance. A decline in the total current derived from the cell encapsulated in a module is also observed. This has helped to narrow down the design variables of commercial silicon solar cells with the standard front electrode grid of fingers and busbars to only the electrical transport.

EXTENSION TO PV OPTICS TO INCLUDE FRONT ELECTRODE DESIGN IN SOLAR CELLS

by
Debraj Guhabiswas

A Dissertation
Submitted to the Faculty of
New Jersey Institute of Technology and
Rutgers, the State University of New Jersey-Newark
in Partial Fulfillment of the Requirements for the Degree of
Doctor of Philosophy in Applied Physics

Federated Department of Physics

January 2013

.

APPROVAL PAGE

EXTENSION TO PV OPTICS TO INCLUDE FRONT ELECTRODE DESIGN IN SOLAR CELLS

Debraj Guhabiswas

Dr. N.M. Ravindra, Dissertation Advisor — Date
Professor and Chair, Department of Applied Physics, NJIT

Dr. B. Sopori, Dissertation Co-advisor — Date
Principal Engineer, NCPV, NREL, CO

Dr. Anthony Fiory, Committee Member — Date
Research Professor of Physics, NJIT

Dr. Tao Zhou, Committee Member
Date
Associate Professor of Physics, NJIT

Dr. Martin Schaden, Committee Member — Date
Associate Professor of Physics, Rutgers, Newark

Dr. Ken Ahn, Committee Member — Date
Assistant Professor in Physics, NJIT

BIOGRAPHICAL SKETCH

Author: Debraj Guhabiswas

Degree: Doctor of Philosophy

Date: January 2013

Undergraduate and Graduate Education:

- Doctor of Philosophy in Applied Physics,
  New Jersey Institute of Technology and Rutgers, Newark, NJ, 2012

- Master of Science in Material Science and Engineering,
  New Jersey Institute of Technology, Newark, NJ, 2007

- Bachelor of Engineering in Polymer Science and Chemical Technology,
  Delhi College of Engineering, New Delhi, India, 2004

Major: Applied Physics

Peer Reviewed Publications

Guhabiswas, D., Sopori, B. *A Ray-trace Analysis for Calculating Reflectance of Individual Grains and the Total Reflectance of a Textured Multicrystalline Silicon Wafer*. (Submitted to EMR)

Guhabiswas, D., Sopori, B., Ravindra, N.M. *The Effect of Front Electrode Architecture on the Optical Performance of Silicon Solar Cells*. (submitted to Progress in Photovoltaics)

Sopori, B., Guhabiswas, D., Rupnowski, R., Shet, S., Devayajanam, S., Moutinho, M. *An Optical Technique for Measurement of Grain Orientation and Sizes in Multicrystalline Silicon Wafers*. (To be submitted Progress in Photovoltaics)

Conference Presentations/Proceedings

Guhabiswas, D., Sopori, B., Rivero, R., Ravindra, N.M. *Extension of PV Optics to include front electrode design*. Poster Presentation delivered at 22nd *Workshop on Crystalline Silicon Solar Cells & Modules: Materials and Processes*, Vail, CO, July, 2012.

Sopori, B., Guhabiswas, D., Rupnowski, P.; Moutinho, H. *New Method for Rapid Measurement of Orientations and Sizes of Grains in Multicrystalline Silicon Wafers*. Conference Proceedings, 37th IEEE PVSC ; 2011, page(s) 001680 – 001685. Poster Presentation delivered at IEEE PVSC, Seattle, WA, June 2011.

Sopori, B., Guhabiswas, D., Rupnowski, P., Shet, S., Devayajanam, S., Helio Moutinho, H., and Ravindra, N.M. *Rapid measurement of orientations and sizes of grains in multicrystalline silicon wafers: A new technique*. Poster presentation delivered at *21st Workshop on Crystalline Silicon Solar Cells & Modules: Materials and Processes,* Breckenridge, CO, August, 2011.

Sopori, B., Guhabiswas, D., Rupnowski, P., Shet, S., Devayajanam, S., Helio Moutinho, H., and Ravindra, N.M. *Characterization of Grains in Multicrystalline Si Wafers Using an Optical Reflectance Technique*. Poster presented at the *2nd MRS workshop on Photovoltaic Materials and Manufacturing Issues II*, Denver, CO, October, 2011.

Sopori, B., Sahoo, S., Mehta, V, Guhabiswas, D., Moutinho, H. *High Quality Cross-Sectioning Method: Examples of Applications in Optimizing Solar Cell Contact Firing*. Conference Proceedings, 37th IEEE PVSC; 2011, page(s) 001674 – 001679. Poster Presentation delivered at IEEE PVSC, Seattle, WA, June 2011.

Sopori, B., Sahoo, S., Mehta, V, Guhabiswas, D., Sean Spiller, S., Helio Moutinho, H.; *A method for cross-sectioning large lengths of Solar Cells*. *2nd MRS workshop on Photovoltaic Materials and Manufacturing Issues II*, Denver, CO, October 2011.

Sopori, B.; Devayajanam, S.; Shet, S.; Guhabiswas, D., Sahoo, S.; *Characterizing Damage on Si Wafer Surfaces*. *22nd Workshop on Crystalline Silicon Solar Cells & Modules: Materials and Processes,* Vail, CO, July, 2012.

Sopori, B.L.; Sahoo, S.; Mehta, V.; Guhabiswas, D.; Spiller, S.; Moutinho, H. *Cross-Sectioning Silicon Solar Cell*. Poster presented at *21st Workshop on Crystalline Silicon Solar Cells & Modules: Materials and Processes,* Breckenridge, CO, August, 2011.

Sopori, B., Rupnowski, P., *Guhabiswas, D.*, Devayajanam, S., Shet, S., Khattak, C. P., Albert, M. (2010). *Reflectance Spectroscopy-Based Tool for High-Speed Characterization of Silicon Wafers and Solar Cells in Commercial Production*. Conference Proceedings, 35th IEEE PVSC, June, 2010, pp. 002238-002241.

Sopori, B.; Mehta, V.; *Guhabiswas, D.*; Reedy, R.; Moutinho, H.; To, B.; Shaikh, A.; Rangappan, A. (2009*). Formation of a Back Contact by Fire-Through Process of Screen-Printed Si Solar Cells*. Conference Proceedings, 34th IEEE PVSC, June, 2009, pp. 001963-001968.

Young, J.L., Mehta, V., Guhabiswas, D., Moutinho, H., Bobby To, Ravindra, N.M., & Sopori, B. (2009 August). *Back contact formation in Silicon solar*

cells: Investigations using a novel cross-sectioning technique. 19th *Workshop on Crystalline Silicon Solar Cells & Modules and Processes*, Vail, CO, August, 2009.

Mehta, V., Sopori, B., Guhabiswas, D., Reedy, R., Moutinho, H., To, B., Liu, F., Shaikh, A., Young, H., & Rangappan, A. (2009, August*). A new approach to overcome some limitations of back Al contact formation of screen printed silicon solar cells*. *19th Workshop on Crystalline Silicon Solar Cells & Modules: Materials and Processes*, Vail, CO, August, 2009.

Sopori, B.; Rupnowski, P.; Appel, J.; *Guhabiswas, D.*; Anderson-Jackson, L. (2009). *Light-Induced Passivation of Si by Iodine Ethanol Solution*. Materials Research Society Symposium Proceedings, Vol. 1123. Warrendale, PA: Materials Research Society, pp. 137-144

To my beloved family

ACKNOWLEDGMENT

I am deeply grateful to my advisors, Dr. Bhushan Sopori at NREL and Dr. N.M. Ravindra at NJIT for suggesting and supervising the work presented in this dissertation. They have been enormously supportive of me throughout the course of my PhD. I would extend a special thanks to Dr. Bhushan Sopori for sharing his wide range of knowledge and experience with me during my work at NREL.

This work was supported by the U.S. Department of Energy under Contract No. DE-AC36-08-GO28308. I am also very grateful to Robert White at NREL for patiently helping me out with computer programming. Marty Scott at NREL also deserves a special acknowledgement for teaching me how to use various optical characterization instruments.

I am especially grateful to my colleagues- Przemyslaw Peter Rupnowski, Vishal Mehta, Sudhakar Shet, Srinivasmurthy Devayajanam, and Vinay Budhraja, for all their support at various stages during my stay at NREL.

I benefitted greatly from the advice and insights of the members of my Dissertation and Oral Examination Committees- Dr. Anthony Fiory, Dr. Tao Zhou, and Dr. Ken Ahn of NJIT, and Dr. Martin Schaden of Rutgers.

I would like to acknowledge my deepest gratitude towards my family for supporting me all this while. I owe all this to my dear parents, Mr. Debashish Guhabiswas and Mrs. Anita Guhabiswas.

Last, but not the least, I would especially like to thank my dear wife, Mrs. Garima Guhabiswas, for being my greatest support and source of encouragement.

TABLE OF CONTENTS

TABLE OF CONTENTS
(Continued)

TABLE OF CONTENTS
(Continued)

TABLE OF CONTENTS
(Continued)

LIST OF TABLES

LIST OF TABLES
(Continued)

LIST OF FIGURES

LIST OF FIGURES
(Continued)

LIST OF FIGURES
(Continued)

LIST OF FIGURES
(Continued)

LIST OF FIGURES
(Continued)

LIST OF FIGURES
(Continued)

LIST OF FIGURES
(Continued)

CHAPTER 1

INTRODUCTION

1.1 Background

Can you imagine a world without energy? Each and every scientific and technological development that helps us to improve our standard of living, to connect to people around us via smart-phones or do the most basic things in our lives such as travelling would be meaningless if we did not have the energy to make it work. At present, the staple sources of energy for mankind are fossil fuels. We burn fossil fuels to drive our cars, to generate electricity and to do every thing that requires energy. The major side effect of burning such huge amounts of fossil fuels each day is the exhaust of many harmful gases such as carbon dioxide, carbon monoxide, sulphur oxides etc. into the earth's atmosphere. These man-made additions to our atmosphere have led to air pollution and global warming. It is common knowledge that global warming, over the period of next many years, will have catastrophic effects on our ecosystems. This, along with the fact that fossil fuels will not last forever, makes it imperative for us to look for clean and renewable sources of energy and technologies to harness them efficiently.

The Sun contains the largest reservoir of energy that can be used by mankind. It is abundant, freely available and renewable in nature. The interaction of light with matter has long been studied with enormous interest. Becquerel, in 1839, first reported the *photovoltaic effect* when he observed an increase in the

electricity generation rate in an electrolytic cell made up of two metal electrodes placed in an electrically conducting solution upon exposure to light. Willoughby Smith discovered photoconductivity of selenium in 1873. William Grylls Adams and Richard Evans Day, in 1876, were the first to discover that selenium produced electricity when exposed to light while an American inventor, Charles Fritts, described the first solar cells made out of selenium wafers in 1883. In 1887, Heinrich Hertz observed that ultraviolet light altered the lowest voltage capable of causing a spark to jump between two metal electrodes. Albert Einstein first proposed the *photoelectric effect* in 1905, which was experimentally verified later by Robert Millikan in 1916. 1932 was a defining period when Audobert and Stora discovered the *photovoltaic effect* in cadmium sulfide (CdS). The first silicon solar cell was reported in 1941; but it was only in 1954 when Daryl Chapin, Calvin Fuller, and Gerald Pearson, at Bell Labs, developed the forerunner of the present silicon solar cells. Since then, the use of solar cells has expanded from space to terrestrial applications. All this has been accompanied by a huge reduction in the manufacturing cost of commercial solar cells. The complete timeline on the discoveries and developments relating to solar energy can be found at the US Department of Energy's website cited in reference [1] while a comprehensive history on the development of solar cells can be found in reference [2].

The ability to utilize the energy from the Sun is the key to the future well-being of mankind. In this respect, the solar cell is considered to be the most

promising technology that can help use this form of energy efficiently and in a meaningful manner. Hence, it is essential that a brief introduction to the physics of semiconductors and the p-n junction in both dark and illuminated conditions be discussed. This will lead to a much better understanding of the technology of solar cells. A brief introduction to the fundamentals of optics used in this work including ray-tracing will be provided in this chapter to facilitate a better understanding of the model developed in this dissertation.

1.2 Introduction to Solar Cells

A brief introduction to the functioning of solar cells will be given in this section. In order to highlight the concepts of photovoltaics used in this dissertation, this section will be broken up into the following sub-sections:

1) Semiconductors
2) P-N Junction
3) The Solar Spectrum
4) Solar Cells: Functioning and Structure

The first topic will give an overview of the physics of the building block of solar cells: semiconductors. Basically, a solar cell is a large area diode with metal contacts at both ends to extract the photo-generated carriers that flow due to a concentration gradient within it. The second topic will focus on a basic explanation of a *p-n junction*, without which there would be no solar photovoltaic technology. The third topic will outline the characteristics of the solar irradiance received on earth. This is most vital since all the optical modeling in this

dissertation is based on the solar irradiance. The fourth topic will enunciate the functioning of solar cells along with a brief description of the structure of a standard crystalline solar cell that has been used for calculations in this thesis. For those interested in other technologies as well, relevant references to review articles pertaining to those topics will be provided for further reading.

1.2.1 Semiconductors

Solid-state materials are classified into three groups according to their electrical properties- insulators, semiconductors, and conductors. Insulators are materials that have very low conductivities while conductors are materials that have very high conductivities. Semiconductors are materials that have conductivities in between those of insulators and conductors. It is important to note that the conductivity of a semiconductor is generally sensitive to illumination, impurities, and magnetic field. This sensitivity of the conductivity of a semiconductor to illumination and impurities is exploited in a solar cell through what is called as the *photovoltaic effect*.

Semiconductors can be elements, e.g. silicon and germanium, as well as compounds, e.g. GaAs, CdTe, CdS etc. in nature. Such pure semiconductors are also called *intrinsic* semiconductors. When impurities, also called dopants, are added to a semiconductor, they introduce excess electrons or holes in the crystal lattice. For example, Group V elements from the periodic table, such as phosphorus or arsenic are added to silicon, silicon behaves as an "*n-type*" semiconductor with electrons being the majority charge carriers. Introduction of impurities that makes a semiconductor deficient in electrons, e.g. Group III

elements from the periodic table such as boron, aluminum or gallium in silicon, makes it "*p-type*" with "holes" being the majority carriers. Such semiconductors are also called *extrinsic* semiconductors. Extrinsic or doped semiconductors have much larger conductivity compared to the intrinsic semiconductors. Their conductivity is proportional to the concentration of impurities in it. Doping plays an essential role in all semiconductor devices.

Figure 1.1 shows the bond diagram of silicon lattice with an n-type dopant, and a p-type dopant. Note the valence electrons in the yellow regions and the dopant-introduced conduction electron outside of that region in the n-type silicon doped with phosphorous in Figure 1.1, and the dopant-introduced mobile hole in the p-type silicon doped with boron in the same Figure. Both of them, being more mobile than the valence electrons, conduct more easily. A band structure diagram, shown in Figure 1.2, can also represent the bond structure shown below.

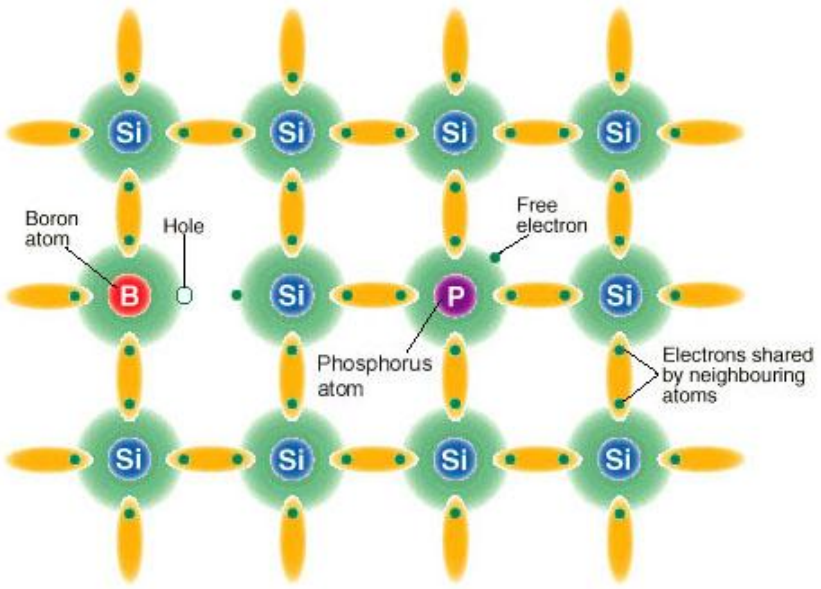

Figure 1.1 Silicon bond structure with an "n-type" dopant phosphorous and with a "p-type" dopant boron [3].

Figure 1.2 shows a simplified band diagram of intrinsic, n-type and p-type silicon. The electrons bound to the silicon atom lie in the valence band while the conduction electrons lie in the conduction band with E_g, the "Band Gap" between the valence band and the conduction band, being the "Forbidden Region" because no electrons can occupy these energy states. In the case of an undoped or intrinsic semiconductor, there is just the right number of electrons to fill the valence band completely. It is only when some of the valence band electrons are excited to the conduction band, due to thermal or optical excitation, that the semiconductor can start to conduct electricity. As can also be seen from Figure 1.2, introduction of impurities changes the effective gap between the conduction band and the valence band due to the introduction of a new *Donor Level* (E_c), the energy level of an n-type dopant, and the *Acceptor Level* (E_v), the energy level of a p-type dopant. This is of vital importance to not only to the functioning of solar cells but all semiconductor devices.

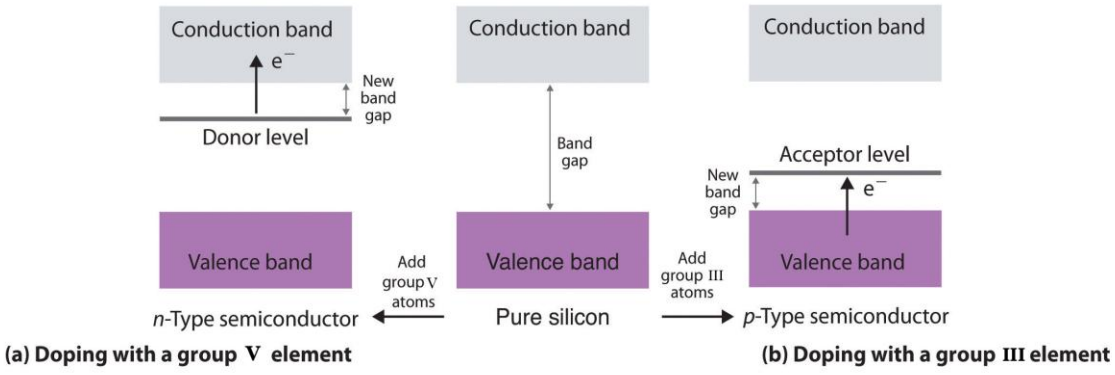

Figure 1.2 Band diagram (a) n-type semiconductor, and (b) p-type semiconductor [4].

The electron carrier density in an extrinsic semiconductor is given by:

$$n = N_C \ \exp[(E_F - E_C)/kT] \tag{1.1}$$

and similarly, the hole carrier density in an extrinsic semiconductor is given by

$$p = N_v \ \exp[(E_v - E_F)/kT] \tag{1.2}$$

where n is the electron density, p is the hole density, E_F is the intrinsic Fermi level, N_C and N_V are constants at fixed T known as the effective density of states in the conduction band and the effective density of states in the valence band, respectively, k is the Boltzmann constant and T is the temperature of the semiconductor in Kelvin.

The electron density, n, and the hole density, p, are related to each other in terms of the intrinsic carrier concentration, n_i, by:

$$np = {n_i}^2 \tag{1.3}$$

The resistivity and conductivity of a semiconductor is given by:

$$\rho = \frac{1}{\sigma} = \frac{1}{q(n\mu_n + p\mu_p)} \tag{1.4}$$

where, ρ is the resistivity of the semiconductor, σ is its conductivity, q is the electronic charge magnitude, n is the density of free electrons, p is the density of holes, μ_n is the mobility of a free electron and μ_p is the mobility of a free hole.

In case of such homogeneous semiconductors, transport or conduction of carriers has two components:

- *Drift Current*: Transport of carriers under the influence of an applied electric field - The electron drift current density, $\boldsymbol{J_n}$, and the hole drift current density, $\boldsymbol{J_p}$ are given by:

$$\boldsymbol{J_n} = qn\mu_n\boldsymbol{\xi} \tag{1.5}$$

$$\boldsymbol{J_p} = qp\mu_p\boldsymbol{\xi} \tag{1.6}$$

where, μ_n is the mobility of a free electron, μ_p is the mobility of a free hole and ξ is the applied electric field.

- *Diffusion Current*: Transport of carriers from a region of high concentration to a region of low concentration - The one dimensional electron diffusion current density, J_n, and the hole diffusion current density, J_p are given by:

$$\boldsymbol{J_n} = qD_n\frac{dn}{dx} \tag{1.7}$$

$$\boldsymbol{J}_p = q\boldsymbol{D_p}\frac{dp}{dx} \tag{1.8}$$

where, $\boldsymbol{D_n}$ and $\boldsymbol{D_p}$ are the electron and hole diffusion coefficients, respectively.

Hence, the cumulative current densities are:

$$\boldsymbol{J_n} = q\mu_n n\boldsymbol{\xi} + q\boldsymbol{D_n}\frac{dn}{dx} \tag{1.9}$$

$$\boldsymbol{J_p} = q\mu_p p\boldsymbol{\xi} + q\boldsymbol{D_p}\frac{dp}{dx} \tag{1.10}$$

$$\boldsymbol{J_{tot}} = \boldsymbol{J_n} + \boldsymbol{J_p} \tag{1.11}$$

where, $\boldsymbol{J_{tot}}$ is the total conduction current density.

The continuity equations for minority carriers are:

$$\nabla.\boldsymbol{J_p} = -\nabla.\boldsymbol{J_n} = q(G - R) \tag{1.12}$$

where, *G* is the generation rate while *R* is the recombination rate. A rigorous solution of these equations can be achieved throughout the semiconductor sample.

1.2.2 *pn* Junction

A *pn* junction results when a *p*-type semiconductor is doped with an *n*-type impurity or vice versa. Due to carrier concentration gradients between both the sides, excess electrons from the *n*-type side flow into the *p*-type side while excess holes from the *p*-type side flow into the *n*-type side, giving rise to the diffusion component of the current density. This migration of charges leaves behind charged ion cores near the junction of both the semiconductors creating the *pn junction*. The charged ion cores give rise to an electric field directed from

the *n*-doped region to the *p*-doped region, which in turn creates the drift component of the current. The charged region at the junction, also called the space charge region, is deficient in free carriers. At equilibrium, the drift current exactly cancels out the diffused current. Solving the continuity equations along with the Poisson equation for the material gives the thickness of the *pn* junction and the built-in voltage. The Poisson's equation is:

$$\nabla^2 \boldsymbol{\psi} = -\frac{q}{\varepsilon_s}(N_D - N_A + p - n) \tag{1.13}$$

where, $\boldsymbol{\varepsilon}_s$ is the relative permittivity of the medium.

The built-in potential (V_{bi}) due to the space charge region is given by:

$$V_{bi} = \psi_n - \psi_p = \frac{kT}{q}\ln\left(\frac{N_A N_D}{{n_i}^2}\right) \tag{1.14}$$

where, N_A is the acceptor dopant concentration and N_D is the donor dopant concentration.

The width of an abrupt *pn* junction width is given by:

$$W = \sqrt{\frac{2\varepsilon_s}{q}\left(\frac{N_A + N_D}{N_A N_D}\right)V_{bi}} \tag{1.15}$$

The formation of the *pn* junction is also accompanied by the bending of the valence and conduction energy bands near the junction. This bending is

proportional to the electric field across the *pn* junction. Figure 1.3 shows the direction of the electric field, the direction of the drift and diffusion currents for holes and electrons, the band bending and other details across an unbiased *pn* junction.

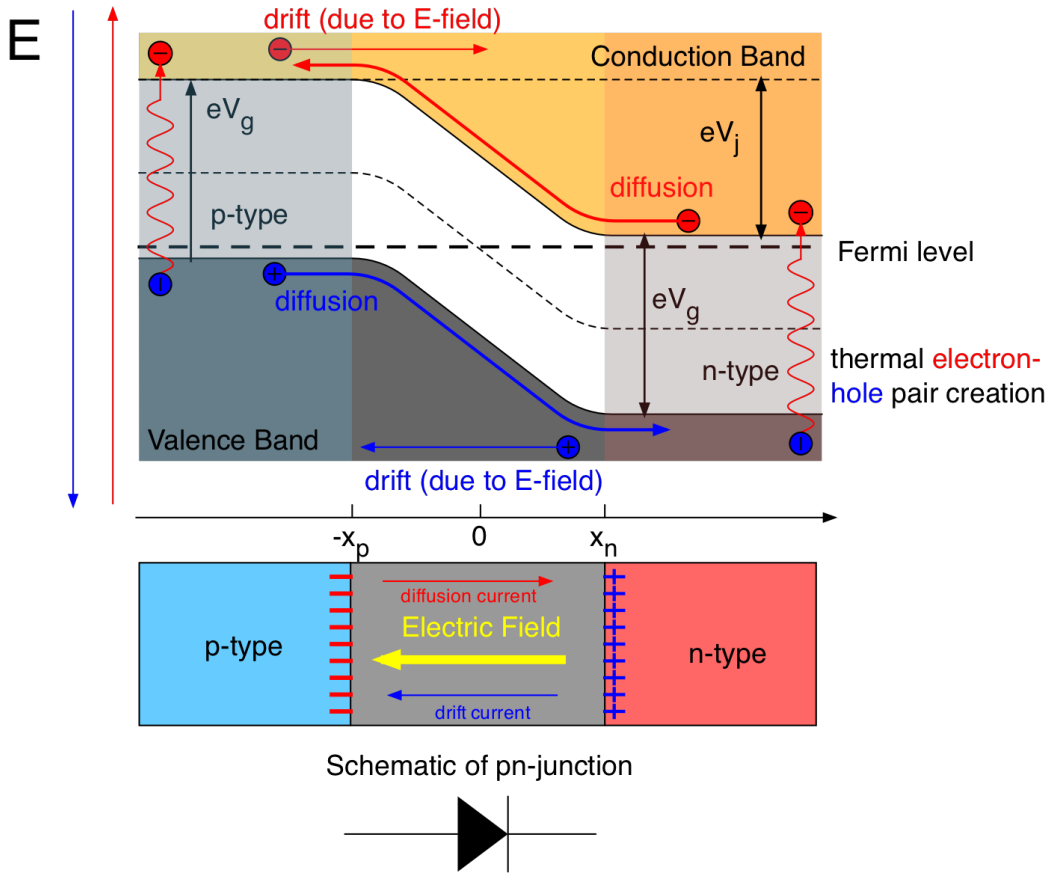

Figure 1.3 Trends of the carrier concentration, the direction of the electric field, and the direction of the drift and diffusion currents for both holes and electrons across an unbiased *pn* junction [5].

Figure 1.4 shows the effect of biasing on the bending of valence and conduction bands. In the Figure, V_J is the junction voltage and V is the applied voltage. The insets at the bottom also show the circuits for reverse and forward biasing. As can be seen, the depletion region increases during reverse biasing and it decreases during forward biasing.

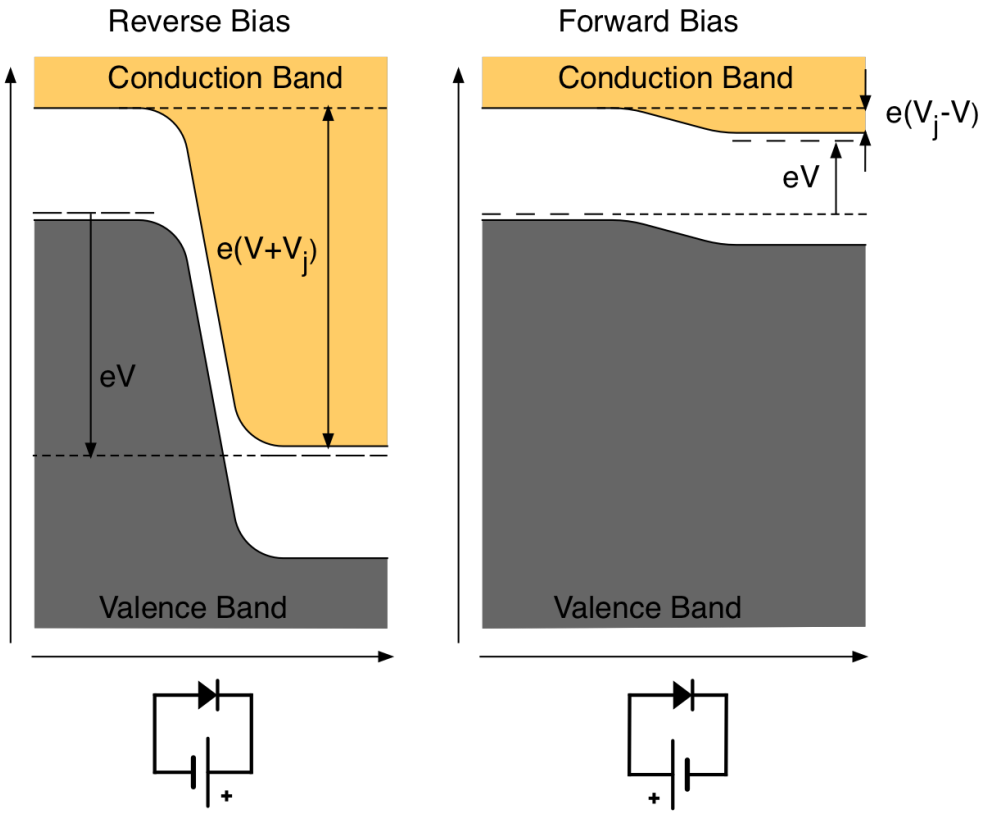

Figure 1.4 A *pn* junction with the depletion region, carrier concentration across the junction, and the electric field at thermal equilibrium [5] .

The J-V characteristics of an ideal diode are given by the diode equation:

$$\boldsymbol{J} = \boldsymbol{J_s}\left(e^{qV/kT} - 1\right) \tag{1.16}$$

where, $\boldsymbol{J}$ is the current density, $\boldsymbol{J_s}$ is the reverse saturation current density and q is the electronic charge.

Figure 1.5 shows the J-V characteristics of an ideal diode. The negative voltage at which the current increases abruptly is called the Breakdown Voltage. A detailed discussion on the operation of the diode can be found in the references [6-8].

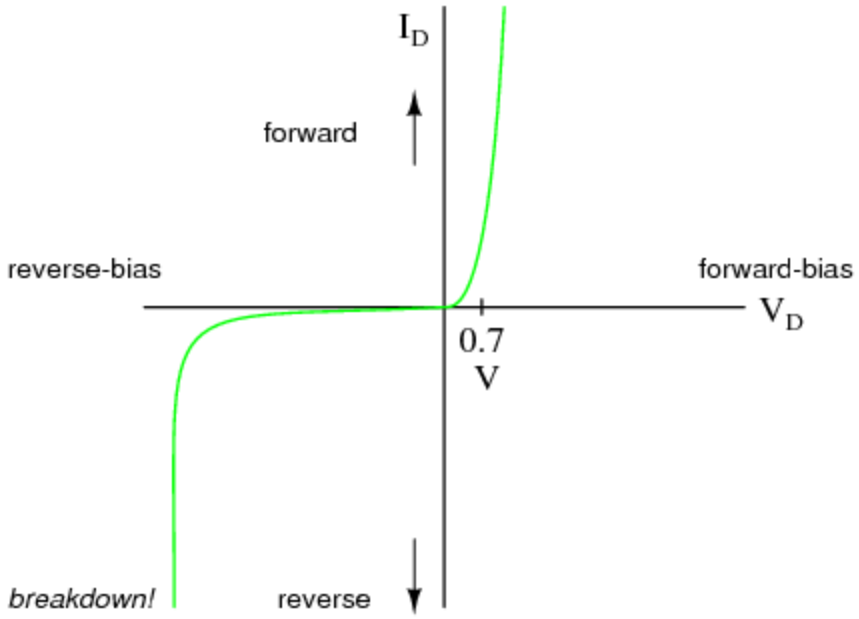

Figure 1.5 Standard J-V curve for an ideal diode [9].

1.2.3 The Solar Spectrum

The effective temperature on the surface of the Sun is 5778 K [10]. Figure 1.6 shows the radiation spectrum expected from a black body at 6000 K. The incident radiant power from the Sun, perpendicular to its direction, per unit area, outside the earth's atmosphere is constant for all practical purposes. This radiation intensity was measured to be 1.353 kW/m^2 [11] and is called *air mass zero* (AM0) *radiation*. As can be seen from Figure 1.6, the incident radiation from the sun is different from that of a black body at 6000K. This is attributed to the effects such as differing transmissivity of the sun's atmosphere at various wavelengths [12].

The radiation reaching the surface of the earth is reduced by more than 30% while travelling through the earth's atmosphere. This attenuation is due to Rayleigh scattering, scattering by aerosols and dust particles and absorption by

the atmosphere and its constituent gases [13, 14]. The total incident power reaching any point on the earth, at a given time under clear conditions, is dependent on the length of the light path through the atmosphere.

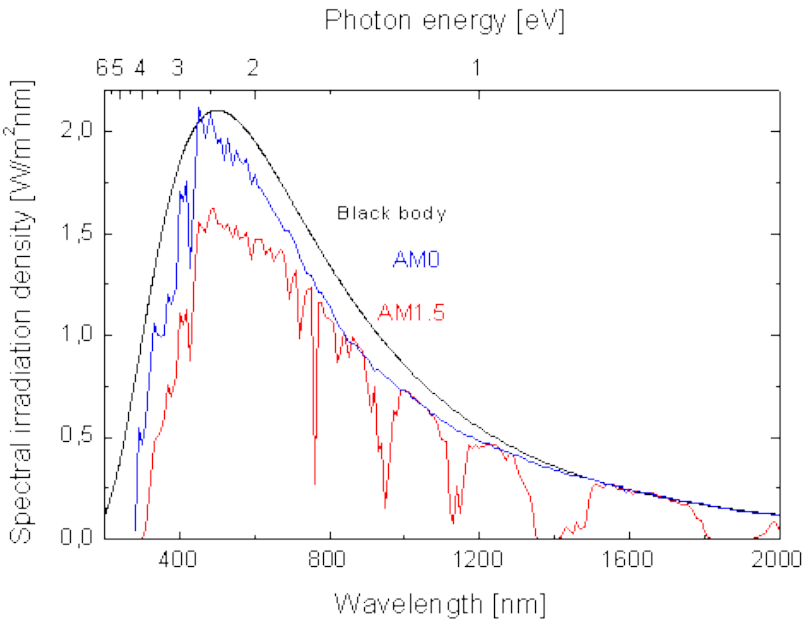

Figure 1.6 Spectral distribution of sunlight for a black body at 6000K, AM 0 and AM 1.5 [15].

The ratio of the actual path length to the minimum, i.e., when the sun is directly overhead, is called the *optical air mass*. Hence, when the sun is directly overhead, the optical air mass is 1. This is also denoted as *air mass one* (AM 1) *radiation*. This is written mathematically as:

$$Air\ Mass = \frac{1}{cos\theta} \tag{1.17}$$

where, θ is the angle of the sun with the vertical overhead.

This implies that, with increasing air mass but keeping all the other variables constant, the incident radiation decreases as the air mass increases. The most commonly used air mass for solar cell calculations and characterization is AM 1.5. In 1977, the U.S. government's photovoltaic program standardized this to a total power density of 1 kW/m^2 [16]. The ideal solar cell efficiencies at 300 K have also been calculated as a function of energy bandgap under one sun AM 1.5 irradiance [17]. Hence, all calculations in this dissertation have been done for an irradiance of AM 1.5.

1.2.4 Solar Cells

A solar cell is a semiconductor device that converts sunlight directly to electricity. It has the potential to provide power nearly permanently with low operating costs and create almost no pollution at all [18, 19]. Even though silicon solar cells have been the workhorse of the photovoltaic industry over the last many decades, other materials and technologies have also become relevant now [20-31].

The simplest design for a solar cell consists of a single shallow *pn* junction on the surface, a front ohmic contact stripe and fingers, a back ohmic contact covering the entire back surface, and an antireflection coating on the front [32] as shown in Figure 1.7. When a solar cell is illuminated with light, photons with energy higher than the band gap, E_g, are absorbed producing an electron-hole pair while photons with energy less than the band gap are not absorbed, thereby, making no contribution to the output current.

The output of a solar cell can be approximated using the one diode model. Figure 1.8 shows this circuit where I_L is the source current resulting from the

excitation of excess carriers by solar radiation, I_s is the diode saturation current, and R_L is the load resistance. This model can be made more complicated for better approximation. But the one diode model has proven to be quite satisfactory.

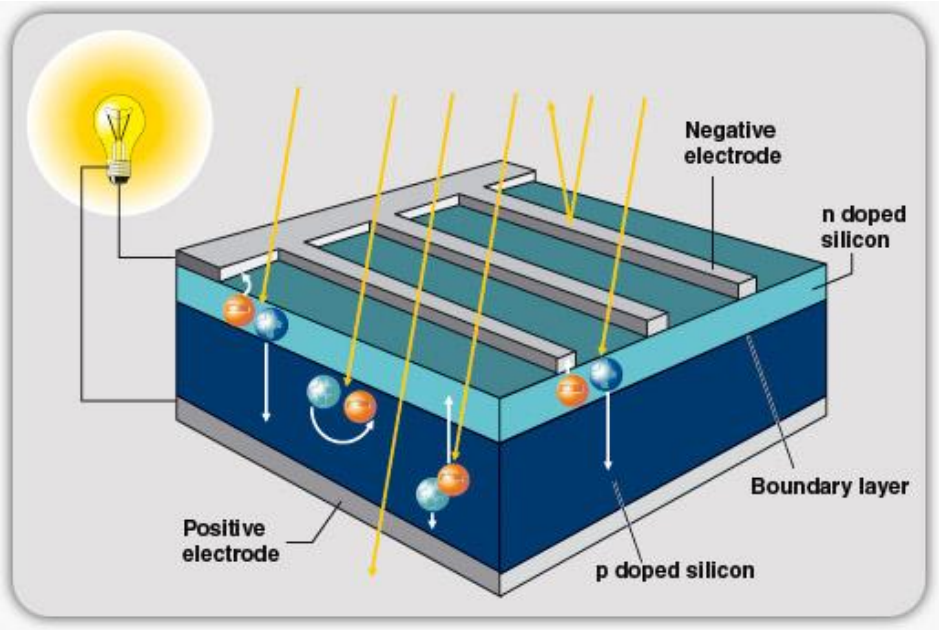

Figure 1.7 A standard single junction silicon solar cell structure [33].

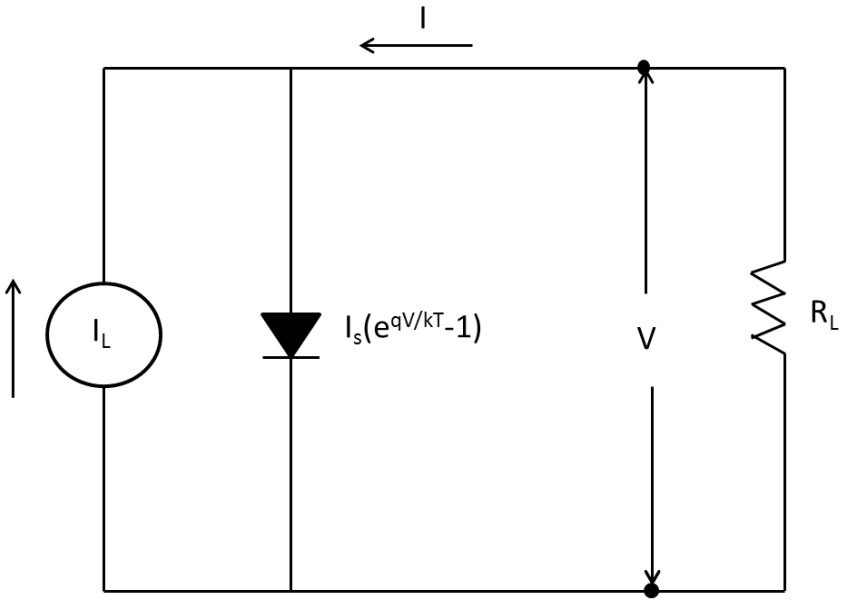

Figure 1.8 The idealized equivalent circuit of a solar cell.

The ideal I-V characteristics of such a single junction solar cell is given by:

$$I = I_S\left(e^{qV/kT} - 1\right) - I_L \tag{1.18}$$

$$I_S = AqN_C N_V \left(\frac{1}{N_A}\sqrt{\frac{D_n}{\tau_n}} + \frac{1}{N_D}\sqrt{\frac{D_P}{\tau_P}}\right).e^{-E_g/kT} \tag{1.19}$$

$$I_L = AqG(L_e + W + L_h) \tag{1.20}$$

where, *A* is the device area, D_n and D_p are the diffusivities of electron and hole in p and n-type regions respectively, L_e and L_h are the minority carrier diffusion length in the p and n-type regions respectively and *W* is the depletion region width.

During the functioning of a solar cell, the I-V curve passes through the fourth quadrant allowing power to be extracted from the device. Generally, this curve is inverted and represented in the first quadrant. Figure 1.9(a) shows the general I-V curve for a solar cell and Figure 1.9(b) shows the inverted curve in the first quadrant. From Figure 1.9, the yellow triangle shows the maximum power (P_{max}) rectangle of a solar cell.

$$P_{max} = I_{max}\,.V_{max} \tag{1.21}$$

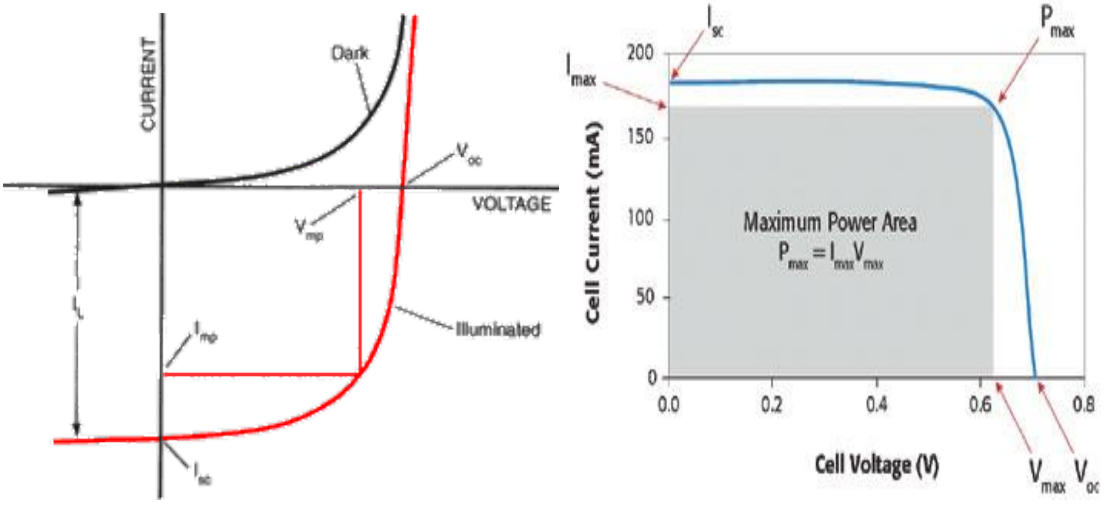

(a) (b)

Figure 1.9 (a) I-V characteristics for a solar cell [34], (b) the curve in the first quadrant [35].

The I-V curve provides important parameters about a solar cell that have a significant effect on its performance.

- Open Circuit Voltage (V_{oc}): This is the voltage across a solar cell when I=0. Its expression can be evaluated from Eq. 1.18 by equating I_L=0. As can be seen from the equation above, V_{oc} is inversely proportional to I_S.

$$V_{OC} = \frac{kT}{q} ln\left(\frac{I_L}{I_S} + 1\right) \tag{1.22}$$

- Short Circuit Current (I_{SC}): This is the current across the solar cell at zero voltage. The short circuit current depends on the minority carrier lifetimes and the total number of photo-generated carriers in the cell.

- Fill Factor (*FF*): The higher the fill factor of a solar cell, the higher is its efficiency. The fill factor of a solar cell can be calculated by the following formula:

$$FF = \frac{I_{max}V_{max}}{I_{SC}V_{OC}} \tag{1.23}$$

Efficiency of energy conversion (η):

$$\eta = \frac{FF.I_L.V_{OC}}{P_{in}} \tag{1.24}$$

where, P_{in} is the incident optical power on the solar cell. As can be seen from Eq. (1.24), the higher the short circuit current (I_{SC}) and the open circuit voltage V_{OC}, the higher is the efficiency of the solar cell. Other than the above-mentioned parameters, two types of resistances: series (R_S) and shunt (R_{SH}) are also important parameters affecting the performance of a solar cell. A thorough discussion on the topic of solar cells can be found in reference [36].

1.3 Introduction to Ray-Tracing

Ray-tracing is the solution of Maxwell's equations for the propagation of an electromagnetic wave within the regime of geometrical optics, i.e., the wavelength of the incident ray is much smaller than the object dimensions. The following is a brief introduction to the relevant optics. This includes optics of non-absorbing media, absorbing media, the concept of total reflection and an introduction to 3- dimensional plane waves.

1.3.1 Maxwell's Equations

Maxwell's equations form the backbone of electrodynamics as well of optics. This calls for a brief review of these equations and their significance. The Maxwell's equations, in SI units, are given by [37]:

$$\nabla . \boldsymbol{D} = \rho \tag{1.25}$$

$$\nabla . \boldsymbol{B} = 0 \tag{1.26}$$

$$\nabla \times \boldsymbol{H} - \frac{1}{c}\frac{\partial \boldsymbol{D}}{\partial t} = \boldsymbol{j} \tag{1.27}$$

$$\nabla \times \mathbf{E} + \frac{1}{c}\frac{\partial \boldsymbol{B}}{\partial t} = 0 \tag{1.28}$$

where, ***j*** is the *electric current density*, ***D*** is the electric displacement, ***E*** is the *electric field*, ***B*** is the magnetic induction, and ***H*** is the magnetic vector.

These variables are further related to each other by:

$$\boldsymbol{j} = \sigma \boldsymbol{E} \tag{1.29}$$

$$\boldsymbol{D} = \epsilon \boldsymbol{E} \tag{1.30}$$

$$\boldsymbol{B} = \mu \boldsymbol{H} \tag{1.31}$$

where, σ is the specific conductivity, ε is the dielectric constant or permittivity and μ is the magnetic permeability. In a homogeneous medium, the Maxwell's equations reduce to [38]:

$$\nabla^2 \boldsymbol{E} - \frac{\epsilon\mu}{c^2}\frac{\partial^2 \boldsymbol{E}}{\partial t^2} = 0 \tag{1.32}$$

$$\nabla^2 \boldsymbol{H} - \frac{\epsilon\mu}{c^2}\frac{\partial^2 \boldsymbol{H}}{\partial t^2} = 0 \tag{1.33}$$

Eq. (1.32) and Eq. (1.33) are standard equations of a wave travelling with a velocity:

$$v = {}^{c}/_{\sqrt{\epsilon\mu}} \tag{1.34}$$

Optical waves are also governed by the same set of equations. The wave that has the least complicated field evolution pattern is a plane wave.

1.3.2 Plane Waves

If V(**r**, t) to represents each rectangular component of the field vectors in a region free of currents and charges, the solution to the Maxwell's field equations yield the following wave equation [39]:

$$\nabla^2 V - \frac{1}{v^2}\frac{\partial^2 V}{\partial t^2} = 0 \tag{1.35}$$

The simplest solution to the above equation of the form $V = V(\boldsymbol{r}.\boldsymbol{s}, t)$ is a plane wave because at each instant of time, V is a constant over each of the planes and

$$\boldsymbol{r}\,.\,\boldsymbol{s} = \text{constant} \tag{1.36}$$

where, ***r*** is the position vector of the point in consideration and ***s*** is the unit vector in the direction of propagation of the wave. The solution to Eq. (1.35) yields [39]:

$$V = V_1(\boldsymbol{r}.\boldsymbol{s} - vt) + V_2(\boldsymbol{r}.\boldsymbol{s} - vt) \tag{1.37}$$

where, V_1 and V_2 are arbitrary functions. V_1 represents a disturbance travelling in the positive direction while V_2 represents a disturbance travelling in the negative direction. The solution to Eq. (1.35), for *E* and *H*, yields:

$$\mathbf{E}=\mathbf{E_0}\,(\text{r.s-vt}) \quad \text{and} \quad \mathbf{H}=\mathbf{H_0}\,(\mathbf{r.s}\text{-vt}) \tag{1.38}$$

The solution of the Maxwell's field equations with the above expressions for *E* and *H* and setting $v/c = 1/\sqrt{\epsilon\pi}$ results in:

$$\boldsymbol{E} = -\sqrt{\frac{\mu}{\epsilon}}\boldsymbol{s} \times \boldsymbol{H}\ , \quad \boldsymbol{H} = \sqrt{\frac{\epsilon}{\mu}}\boldsymbol{s} \times \boldsymbol{E} \tag{1.39}$$

On closer inspection, it is found that $E.s = H.s = 0$ implying that the fields in this case are transversal in nature, i.e., electric and magnetic field vectors lie in planes normal to the direction of propagation. Fig 1.10 shows a graphical representation of a travelling 3D plane wave. The blue planes are the minima positions and red planes are the maxima positions of the amplitude of the plane wave. All the points on each plane have the same amplitude and propagation direction.

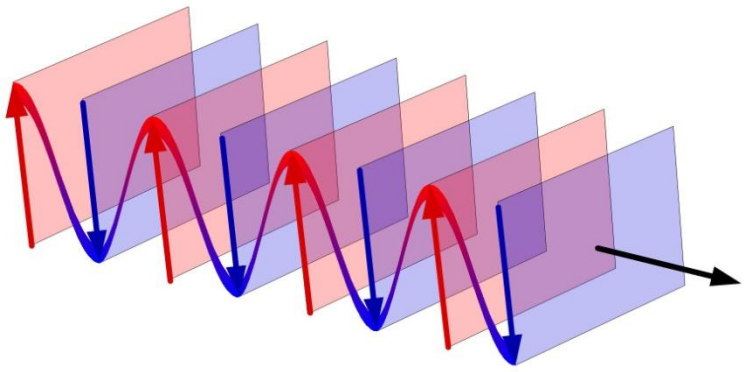

Figure 1.10 Oblique view of a 3D plane wave. The blue planes are minima and the red planes are the maxima of the wave amplitude. The black arrow shows the propagation vector of the wave [40].

1.3.3 Reflection and Refraction in Non-Absorbing Media

On solving the plane wave equations at the boundary between two media with different but real refractive indices gives [41]:

$$\frac{\sin\theta_i}{\sin\theta_t} = \frac{v_1}{v_2} = \sqrt{\frac{\epsilon_2\mu_2}{\epsilon_2\mu_2}} = \frac{n_2}{n_1} \tag{1.40}$$

$$\theta_i = \theta_r \tag{1.41}$$

Eq. (1.40) is the law of refraction and Eq. (1.41) is the law of reflection, also called Snell's law, of light at a surface. Figure 1.11 shows the refraction of light from one medium to the other.

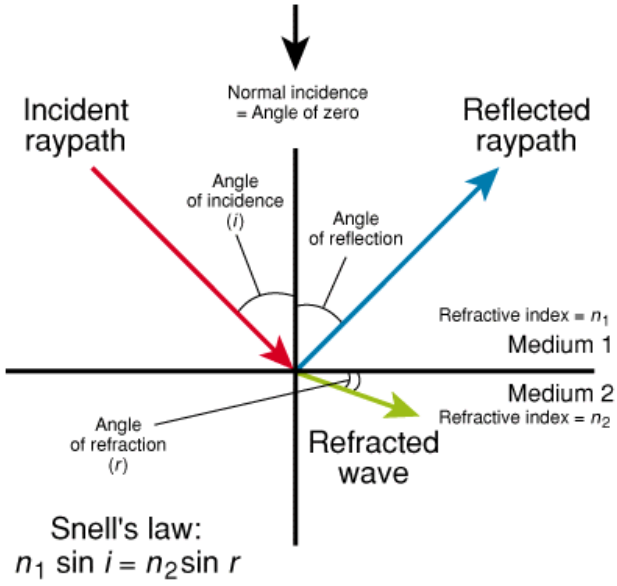

Figure 1.11 The refraction and reflection of light at an interface [42].

Similarly, solving the wave equations at the boundary gives the reflection and transmission coefficient of the wave, also called the Fresnel formulae [43]:

$$R_S = \frac{n_1\cos\theta_i - n_2\cos\theta_t}{n_1\cos\theta_i + n_2\cos\theta_t} A_s \tag{1.42}$$

$$R_p = \frac{n_2 \cos\theta_i - n_1 \cos\theta_t}{n_2 \cos\theta_i + n_1 \cos\theta_t} A_p \tag{1.43}$$

$$R = (R_s^2 + R_p^2)/2 \tag{1.44}$$

$$T_s = \frac{2n_1 \cos\theta_i}{n_1 \cos\theta_i + n_2 \cos\theta_t} A_s \tag{1.45}$$

$$T_p = \frac{2n_1 \cos\theta_i}{n_2 \cos\theta_i + n_1 \cos\theta_t} A_p \tag{1.46}$$

$$T = (T_s^2 + T_p^2)/2 \tag{1.47}$$

$$T = 1 - R \tag{1.48}$$

where, R is the reflection coefficient, T is the transmission coefficient, A_S is the amplitude component perpendicular to the propagation direction and A_P is the amplitude component in the parallel direction. The amplitude can be complex.

1.3.4 Total Reflection

The condition for total reflection can be deduced from the Snell's law [44]. When a wave is moving from an optically denser medium to an optically rarer medium, i.e., from Figure 1.11:

$$n_{12} = \frac{n_2}{n_1} = \sqrt{\frac{\varepsilon_2 \mu_2}{\varepsilon_1 \mu_1}} < 1 \tag{1.49}$$

If the sine of angle of refraction becomes more than 1, there is no transmittance and all the light is reflected back.

1.3.5 Optics of Absorbing Media

Till now, the propagation of a light wave in a non-absorbing medium has been discussed. It would be very pertinent to look at the case in which the medium is absorbing. In this case, Eq. (1.25) from the Maxwell's field equations can be written as [45]:

$$\nabla . \boldsymbol{E} = 0 \tag{1.50}$$

The wave equation for this case then becomes:

$$\nabla^2 \boldsymbol{E} = \frac{\mu\varepsilon}{c^2}\frac{\partial^2 \boldsymbol{E}}{\partial t^2} + \frac{4\pi\mu\varepsilon}{c^2}\frac{\partial \boldsymbol{E}}{\partial t} \tag{1.51}$$

where, the second term on the right hand side implies a damped wave suffering progressive attenuation. On taking $\boldsymbol{E}$ and $\boldsymbol{H}$ of the form $\boldsymbol{E} = \boldsymbol{E_o} e^{-i\omega t}$ and $\boldsymbol{H} = \boldsymbol{H_o}\, e^{-i\omega t}$, Eq. (1.51) becomes [46]:

$$\nabla^2 \boldsymbol{E} + \hat{k}^2 \boldsymbol{E} = 0 \tag{1.52}$$

In the above equation, $\hat{k}$ is complex. It is given by:

$$\hat{k}^2 = \frac{\omega^2 \mu}{c^2}\left(\varepsilon + i\frac{4\pi\sigma}{\omega}\right) \tag{1.53}$$

The dielectric constant, ε, in the above equation is the same as in the case of non-absorbing media. But for the case of absorbing media, Eq. (1.53) is replaced by:

$$\hat{\varepsilon} = \varepsilon + i\frac{4\pi\sigma}{\omega} \tag{1.54}$$

$$\hat{v} = \frac{c}{\sqrt{\mu\hat{\varepsilon}}}, \quad \hat{n} = \frac{c}{\hat{v}} = \sqrt{\mu\hat{\varepsilon}} = \frac{c}{\omega}\hat{k} \tag{1.55}$$

The refractive index, in this case, becomes [46]:

$$\hat{n} = n + ik \tag{1.56}$$

where ‘k’ is the extinction coefficient. The loss in the intensity of a plane wave in an absorbing medium is given by:

$$I = I_o e^{-\alpha r.s} \tag{1.57}$$

where, $\alpha = \frac{4\pi}{\lambda} k$ is the absorption coefficient. The reflection coefficient now becomes [47]:

$$R_s = \frac{\sin(\theta_i - \theta_t)}{\sin(\theta_i + \theta_t)} A_s \tag{1.58}$$

$$R_p = \frac{\tan(\theta_i - \theta_t)}{\tan(\theta_i + \theta_t)} A_p \tag{1.59}$$

Whenever a highly absorbing medium such as a metal is encountered by a plane wave, the above-mentioned equations are used.

1.3.6 Ray Tracing

The equations given in the preceding sections lay the foundations for ray-tracing simulations. Although ray tracing is mainly used for rendering computer graphics [48] and lens design [49], it has been used in solar cell calculations as well [50]. Figure 1.12 shows a schematic of the ray-tracing process. The tracking and labeling of the rays should be noted.

In this scheme of calculations, the incident optical wave is denoted by a large number of rays travelling in the same direction as the propagation vector and with the same intensity as that of the plane wave around that location. Each incident ray has a relative intensity of 1.0 at the start of the calculation. As these rays progress in space, they are tracked till their intensity is all absorbed or if they are captured by one of the detectors. The reflection and transmission coefficients are calculated at each interface in the path of the wave. The intensity

of the wave is updated at each interface and while it is absorbed. 'Daughter rays' are created each time a ray splits up into the reflected and the transmitted ray. Once all the rays have travelled their respective paths, the accumulated intensities for absorption, reflection and transmission are integrated and averaged over the entire spatial area of the calculations and over the entire wavelength range. The complications of ray tracing are not only limited to the optical effects but also include the geometric and material features of the region of interest.

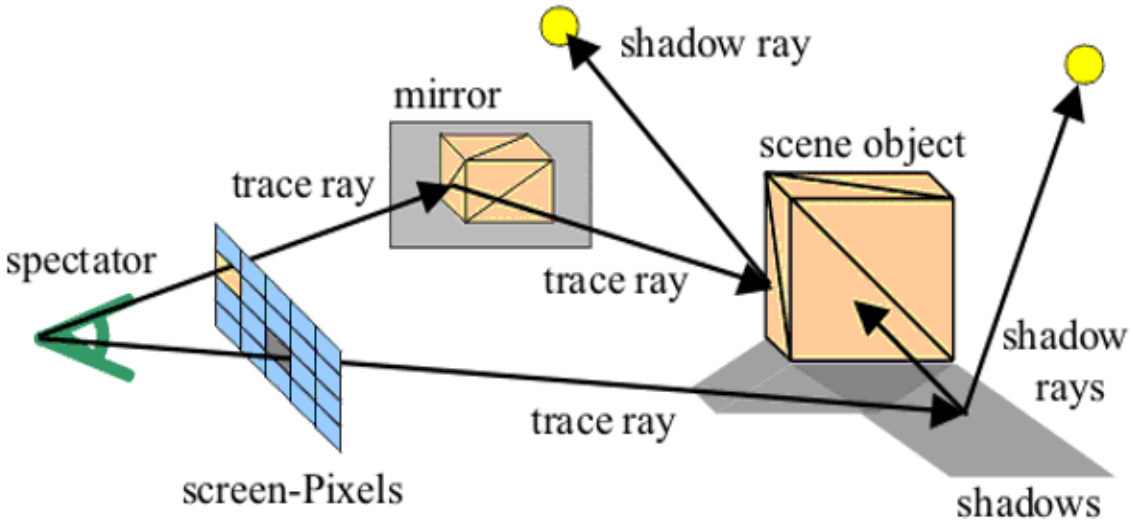

Figure 1.12 A rendering of the ray tracing from the eyes of the viewer to the surroundings. The state of the ray is updated all along till it is completely absorbed or captured [51].

1.4 DISSERTATION OUTLINE

Optical modeling of solar cells and modules is a very important process in optimizing cell efficiency by adjusting the cell architecture, and finding a compromise between efficiency and the production cost. Till now, all the softwares commercially available do not have the option to include front metal

electrode architecture during optical modeling. Due to this, no thorough investigations have been carried out to ascertain the effect of the front metal architecture on the optical performance of solar cells. This work has been successful in:

- Developing a new model to incorporate front metal structure under the purview of ray-tracing,
- Developing a new algorithm to incorporate into a software program,
- Writing a new code in C++ to handle these complex calculations, and
- Carrying out a detailed investigation into the effect of front metal architecture on the optical performance of solar cells.

The dissertation consists of a total six chapters. It will be organized as follows:

- The second chapter will present a review of the work done in this field till now and the approach taken by various groups.
- The third chapter will present the model and algorithm used in this work in detail.
- The fourth chapter will present the results for calculations done on single crystal, anisotropic texture etched, single junction and commercial silicon solar cells.
- The fifth chapter will present the results for calculations done with these cells encapsulated in a complete module and outline the effect of encapsulation on solar cells.
- The sixth chapter will outline the conclusions and future direction of work.

CHAPTER 2

OPTICAL CALCULATIONS AND LIGHT TRAPPING IN SOLAR CELLS: INTRODUCTION AND REVIEW

Optical calculations for solar cells, FDTD [52] or ray tracing [53], are done to examine their light trapping characteristics [54-56]. Since solar Cells work by capturing a part of the radiation incident on them and converting them to electricity, it means that any technology which helps a solar cell to increase the amount of light it captures would in turn increase the amount of power that we derive from it. The process of confining as much light as possible in a solar cell is termed as *Light Trapping*. The first suggestion of using light trapping by total internal reflection to increase the effective absorption in crystalline silicon were motivated by the prospect of increasing the response speed of silicon photodiodes while maintaining high quantum efficiency in the near infrared region [57, 58]. Many different techniques have been tried to make light trapping as efficient as possible. This chapter will present an overview of the various light trapping schemes that have been tried and adopted in the field of solar cells. The review will only focus on silicon based solar cell devices and will not digress into other material based technologies as that is not the focus of this dissertation.

As will be seen during the review of various light trapping schemes in silicon solar cells, surface roughening is a very important method of reducing the reflectance of light and increasing absorption in a solar cell. Hence, the first section of this chapter will present a review of the many methods used to

artificially roughen the surface of silicon wafers or films, also called *Texturing*. These methods include chemical texturing process as well as laser texturing processes. The second part of this chapter will be based on light trapping schemes that are not based on the texturing of the silicon substrate.

The last part of this chapter will be a review of the methodologies used in ray tracing calculations for solar cells and their results. The main reason for performing ray-tracing calculations is to understand the efficiency of light trapping schemes and the various optical losses taking place in a solar cell. They are also used to optimize the design and architecture of not just a solar cell but also of a complete module. This section will also investigate the various ray tracing optical modeling softwares presently available to specifically model solar cells. Lastly, a new method to calculate the reflectance of a potassium hydroxide etched complete multi-crystalline silicon wafer will be explained. This work was done by Guhabiswas during the course of his doctoral work and has led to the development of a new and ultra-fast grain orientation characterization technique [59].

2.1 Texturing Based Light Trapping Schemes for Silicon: A Review

It has been shown that texturization can increase the short circuit current in a solar cell due to three main reasons [60] :

- By reduction in reflectance of the solar cell,
- Light trapping in the volume of the device,

- Higher light absorption closer to the junction in comparison to a planar surface.

Hence, texturing of silicon has become an inseparable part of silicon solar cell manufacturing [61-67]. Following are the texturing processes that will be reviewed in this chapter:

- Anisotropic Etching
- Acid Etching
- Mechanical Texturing
- Reactive Ion Etching
- Laser Etching

2.1.1 Anisotropic Etching of Silicon

Even though wet chemical isotropic etching has been used in the silicon semiconductor industry during processing since the 1950's [68, 69], it took a little while longer for anisotropic etching of silicon to follow suit [70, 71]. But it was only during the mid-1970's that this process was first introduced for silicon solar cell processing [72].

The anisotropic etching process of silicon is orientation dependent, i.e., different crystal orientations have different etch rates. The most common chemical used for this is potassium hydroxide (KOH) [72], although other hydroxides such as sodium hydroxide (NaOH) and lithium hydroxide [73] as well as tetramethyl ammonium hydroxide (TMAH) [74] can be used. It is known that the (111) crystal plane has the minimum etch rate towards alkaline etching while etch rate along (331) is the fastest [69]. The planes, (100) and (110), have

intermediate etch rates with the etch rate along (100) being faster [75]. This leads to the exposure of the nearest (111) planes to crystal surface after a sufficiently long period of etching. Fig. 2.1 shows an image of an etched surface of (100) orientated silicon crystal surface.

Fig. 2.2 shows a simulated image of a unit texture on a (100) surface. These texture shapes, found on the surface, are shown in Fig. 2.1. This textured surface is of vital importance to light trapping in solar cells made on single crystal (100) oriented silicon substrates. Fig 2.3 shows the same textures in 2D along with a planar surface for comparison. Note how the incident light rays have multiple reflections from the textured surface.

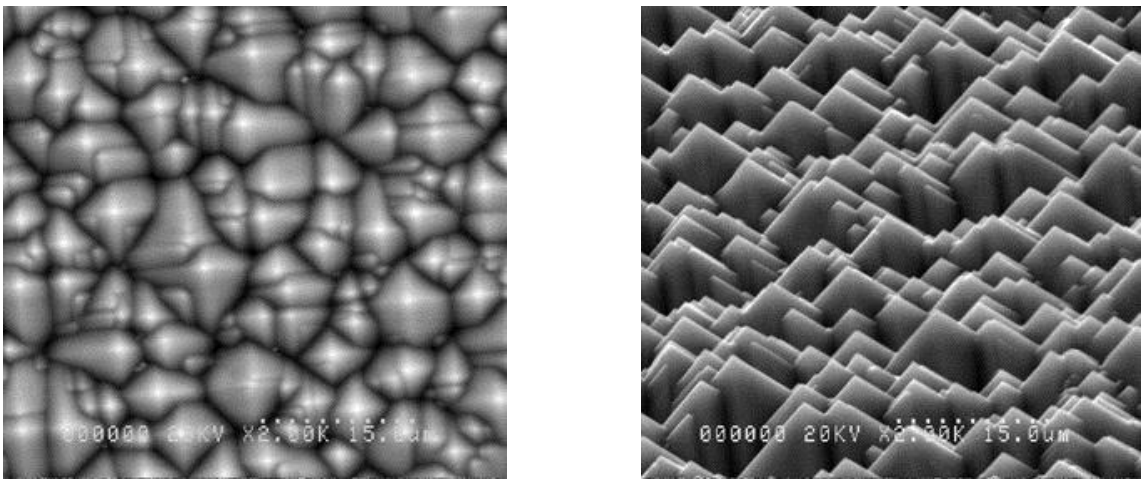

Figure 2.1 The top and angular side view of an SEM image of texture etched (100) silicon wafer surface (taken from [76]).

Every time a ray of light has a reflection from a surface, it loses some of its intensity to transmittance into the material. This implies that the more the number of bounces, the lower the reflectance and higher the transmittance and hence, absorption. This is the fundamental reason for the use of texturing as a means of light trapping in solar cells.

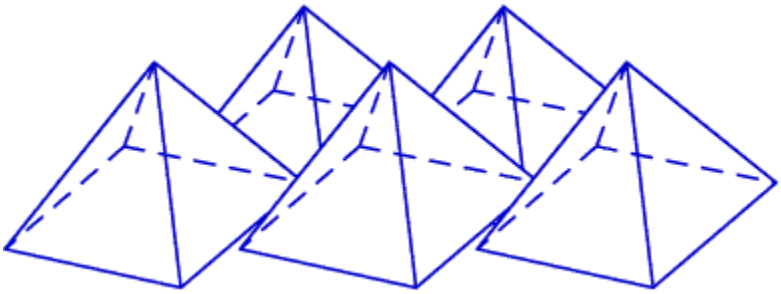

Figure 2.2 A simulated unit texture on (100) oriented silicon surface (taken from [77]).

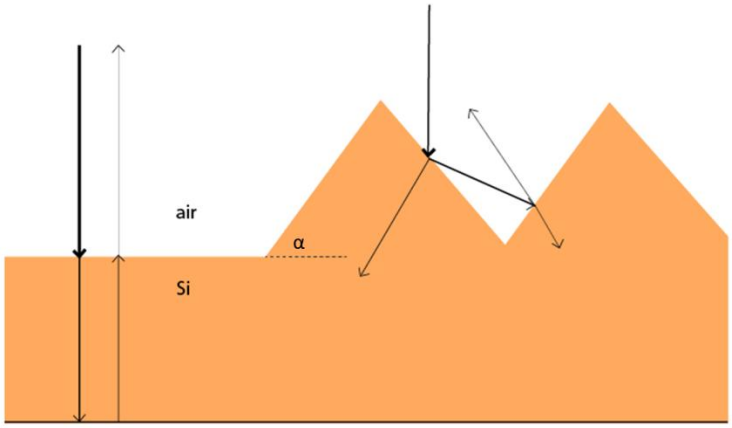

Figure 2.3 Reflection of light from a textured surface and a planar surface.

Fig. 2.4 shows the reflectance of total 200 micron thick silicon wafers for two cases (a) both sides planar, (b) both sides textured with a texture height of 3 microns, simulated in the new version of PV Optics. Note the large difference in reflectance in both the cases. Due to this very reason, potassium hydroxide etching has become an inseparable part of the production process of solar cells based on single crystal (100) silicon substrates. But, in the case of solar cells made on multicrystalline silicon substrates, a new surface texturing process has to be used due to the random orientation of the each grain.

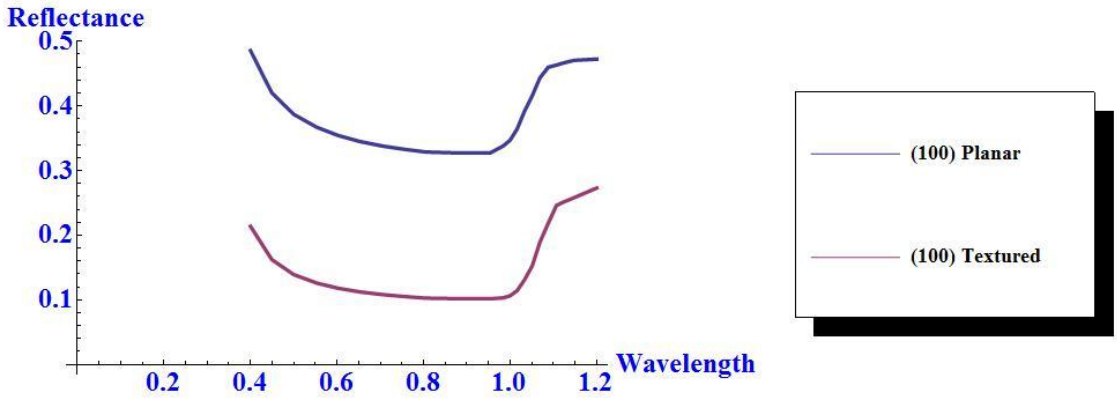

Figure 2.4 Reflectance for planar and textured silicon. Y-axis is the reflectance; X-axis is the wavelength of light.

It is generally believed that the active etching species for this process is the hydroxyl (OH^-) group [73, 78], derived from water in the etching solution. This group reacts with the hydrogen terminated silicon surface molecules [79-81] to form ionized hydroxyl terminated silicon complexes in water [73]. This step is achieved by the breaking of the back bonds of the surface silicon atom, which it forms with other silicon atoms in the crystal lattice. Thereupon, a silicate is formed which can then leave the crystal lattice into the etching solution and release hydrogen gas in the process [78, 82, 83].

Alcoholic moderators like isopropyl alcohol (IPA) have also been incorporated in the etching solution [84]. IPA causes a reversal in etch rates along the (100) directions and the (110) directions compared to the case when no IPA is added to the etch solution [85]. It has also been observed that the addition of IPA results in a higher density of textures on the silicon surface compared to without the addition of IPA [86]. The main problem while adding IPA to the etch solution is its low boiling point of 80°C. This is the temperature around

which texture etching is performed and hence, leads to the evaporation of IPA with time leading to a variable etch solution. The way to circumvent this problem is to conduct the etching process in a closed vessel with a condenser plate at the top.

Following is the electrochemical reaction for the etching process with the hydroxyl group as the reacting species [73]:

$$Si + 4OH^- \rightarrow Si(OH)_4 \quad (2.1)$$

$$Si(OH)_4 + 2OH^- \rightarrow SiO_2(OH)_2^{--} + 2H_20 \quad (2.2)$$

$$4H_20 + 4e^- \rightarrow 4OH^- + 2H_2 \quad (2.3)$$

Even though the above reactions spell out the surface chemistry of the etching process, there is no mention of the reasons for the anisotropic nature of the reaction itself. This can only be found out by considering the silicon crystal lattice itself. A detailed discussion on this can be found in ref [87] and the references therein. Fig 2.5 shows a ball and stick model for a diamond crystal unit cell.

It should be noted that the arrangement of the atoms in the silicon crystal lattice is of ultimate importance when it comes to defining the anisotropic nature of the etching process. The density of atoms on the surface, the number of nearest neighbor surface bonds, number of nearest neighbor bulk back bonds

and the number of secondary neighbor atoms has an impact on the etch rates [87].

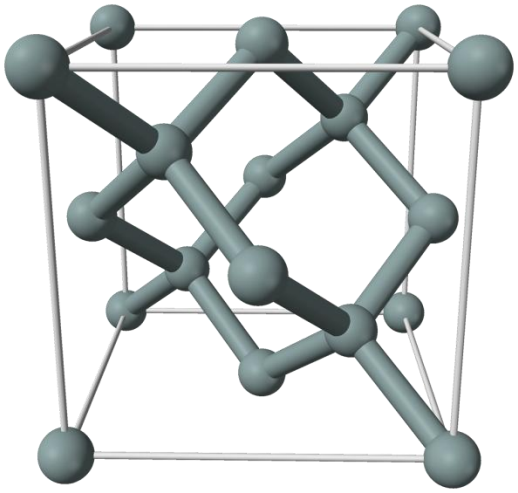

Figure 2.5 Unit cell for a diamond crystal lattice, e.g. Silicon (taken from [88]).

2.1.2 Acid Etching of Silicon

Multicrystalline solar cells, with lesser efficiencies than single crystal solar cells, have become the most important base material for solar cell production [89]. These cells need a texturing etchant that is not anisotropic. Since the crystal orientations of various grains in a multicrystalline silicon wafer are random, anisotropic etchants do not produce satisfactory light trapping properties [90]. Texturing with isotropic etchants have been found to produce much better light trapping properties for these solar cells [91].

Acidic etchants which are based on HF:HNO_3 systems are isotropic in nature. The etching reaction is an oxidation-reduction reaction in which the silicon is oxidized by HNO_3 (nitric acid), and HF serves to remove the oxide. The rate limiting factors are different for the HF rich regions and the HNO_3 rich regions. The oxidation of silicon by HNO_3 limits the etch rate in the HF rich

regions while the removal of oxygen by HF is the rate limiting step in the HNO_3 rich regions [86].

The texture shapes produced by acid etching include rough surfaces, concave *tub* shaped pits, and smooth surfaces. The rough surfaces, produced, have been of great utility and interest for the solar cell community as it can be used as a means for reflection reduction from the cell surfaces [91-93]. Since this etch is not orientation dependent, it results in the uniform texturization of the complete surface of a multicrystalline silicon wafer compared to only the near (100) oriented grains, as in the case of KOH etching.

The acid etching solution is made by diluting the HF:HNO_3 system either in water or acetic acid (CH_3COOH). Since this reaction is an oxidation-reduction reaction, i.e., it depends on electron transfer processes, the etch rate varies for n and p-type materials, and for different doping densities [69, 94-96]. HNO_2 is the active oxidizing species with the reaction being:

$$4\ HNO_2 + Si \rightarrow SiO_2 + 2\ H_2O + 4\ NO \qquad (2.4)$$

HNO_2 in the above reaction forms by an autocatalytic, two-step process, i.e., HNO_3 reduces to form HNO_2. This is the slow rate-determining step. The second reaction generates more HNO_2 by:

$$HNO_2 + HNO_3 \leftrightarrow N_2O_4 + H_2O \qquad (2.5)$$

$$N_2O_4 + 2\ NO + 2H_2O \leftrightarrow 4\ HNO_2 \quad (2.6)$$

The overall chemical reaction can be summarized as:

$$4\ HNO_3 + 2\ Si \rightarrow 2\ SiO_2 + 4\ HNO_2 \quad (2.7)$$

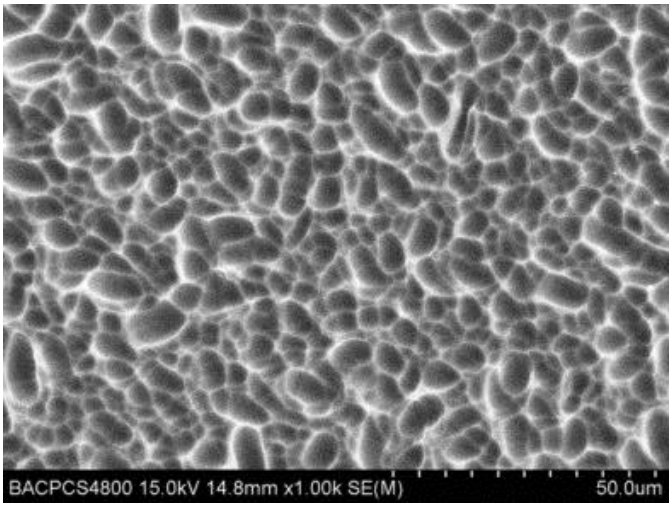

Figure 2.6 SEM image of the surface of an acid etched silicon wafer (taken from [97]).

Crystal imperfections and defects can also initiate the etching process. A detailed discussion on the surface morphology of acid etched wafers can also be found in [86]. Fig. 2.6 shows an SEM image of the surface of an acid etched silicon wafer [97].

2.1.3 Mechanical Texturing

Mechanical texturing of silicon wafers has been tried for light trapping purposes [98-102]. In this process, as the name suggests, the surface of a silicon wafer is grooved into V-shaped structures using a dicing saw with beveled blades. The

texturing can produce V grooves of various angles depending on the placement and angle of the blades. Fig 2.7 shows a standard structure of a mechanically grooved solar cell substrate [100].

This process was envisaged as an alternative to KOH and NaOH texture etching as potassium and sodium are detrimental to the performance of a semiconductor device and need subsequent cleaning steps. But with this advantage, this process has its own set of limitations as well. These disadvantages include low processing speed, tool wear, kerf loss and the sawing damage issues [99].

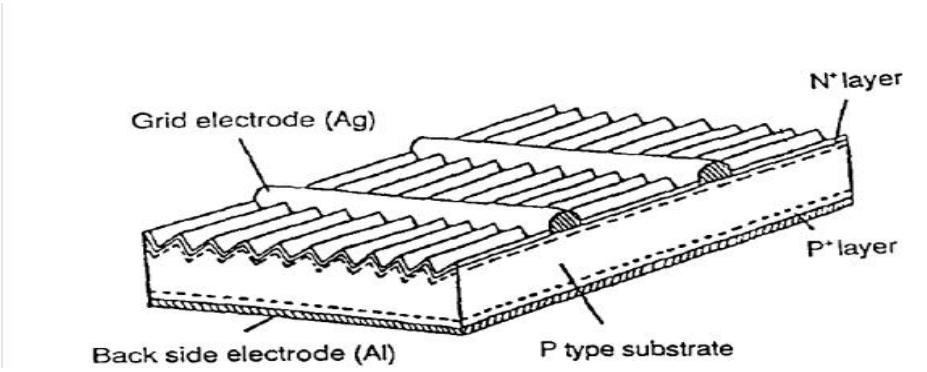

Figure 2.7 Standard solar cell made from mechanically grooved multicrystalline silicon (taken from [100]).

The mechanical grooving process, in many cases, is also followed by a one-step etching treatment of the substrate with $HF:HNO_3:CH_3COOH$ [102] solution to remove mechanically-damaged regions and to form porous silicon layers; or a step of isotropic etching for damage removal [99]. Fig. 2.8 shows a highly magnified SEM image of (a) 35° and (b) 60° mechanically grooved V structures on a silicon substrate [99].

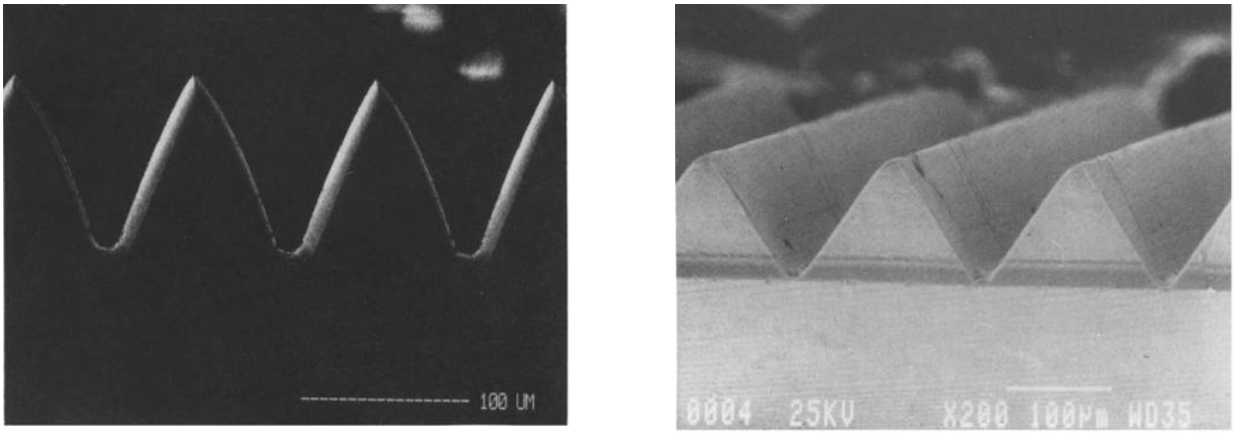

(a) (b)

Figure 2.8 Mechanically grooved structures at (a) 35° and (b) 60° (taken from [99]).

2.1.4 Reactive Ion Etching

Reactive ion etching (RIE), like acid etching, is also an isotropic etching process that produces uniform surface texture irrespective of the crystal orientation of the silicon substrate (e.g., [103]). In this process, a gas glow discharge is used to dissociate and ionize relatively stable molecules to form highly reactive chemical and ionic species [104]. Hence, unlike the acid or KOH etching, this is a dry etching process. These reactive species are then directed to the substrate surface where the etching takes place forming volatile products in the process. The etch gas consists of a chemical etchant for etching the substrate, a passivator for blocking the etching of sidewalls and an ion source for local removal of passivator at the bottom of the etch trenches [105]. In the case of silicon, a mixture of SF_6, O_2, and CHF_3 is widely used [106]. SF_6 provides F^- radicals for etching the silicon that leads to the formation of volatile SiF_6 as a reaction product. O_2 gives O^* radicals which passivate the silicon substrate with

SiO_XF_Y, while CHF_3 gives CF_X^+ ions which remove the passivating SiO_XF_Y to give CO_XF_Y. Fig 2.9 shows the setup for RIE.

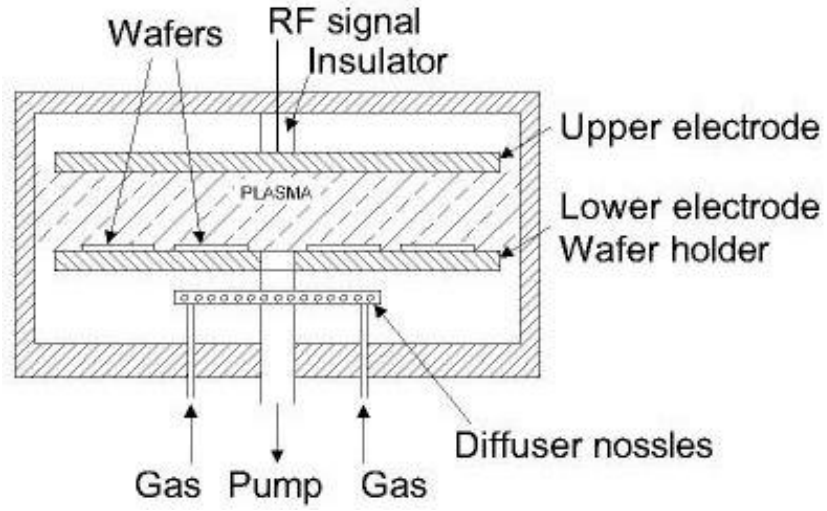

Figure 2.9 Setup for Reactive Ion Etching (taken from [107]).

Following are the steps that take place during RIE [108]:

- The gas mixture stated above is passed through a plasma chamber where a glow discharge, by electron-impact dissociation/ionization, creates the etching environment consisting of neutrals, electrons, photons, radicals (e.g. F*) and positive (e.g. SF_5^+) and negative (e.g. F^-) ions. Low energy ions (20-90eV) are used for a high etch selectivity and for low damage to the substrate and passivating layers.

- As shown in Fig. 2.9, silicon wafers are placed on an r.f. driven capacitatively coupled electrode. After ignition of the plasma, the electrode acquires a negative charge, i.e., the d.c. self-bias voltage, because the mobility of electrons is much greater than the mobility of ions.

- Due to diffusion, the reactive intermediates are transported from the bulk of the plasma to the silicon wafer surface. The positive ions too are forced to the surface from the glow region by the d.c. self-bias. These assist in the etching process as well.

- The reactive radicals adsorb on the silicon surface.

- Reaction between the adsorbed species and silicon takes place. SiF_6, a volatile compound, is produced as a byproduct of this reaction.

- The volatile byproduct is desorbed from the silicon surface into the gas phase.
- The desorbed species diffuse from the etching surface into the bulk of the plasma and are pumped out of the system.

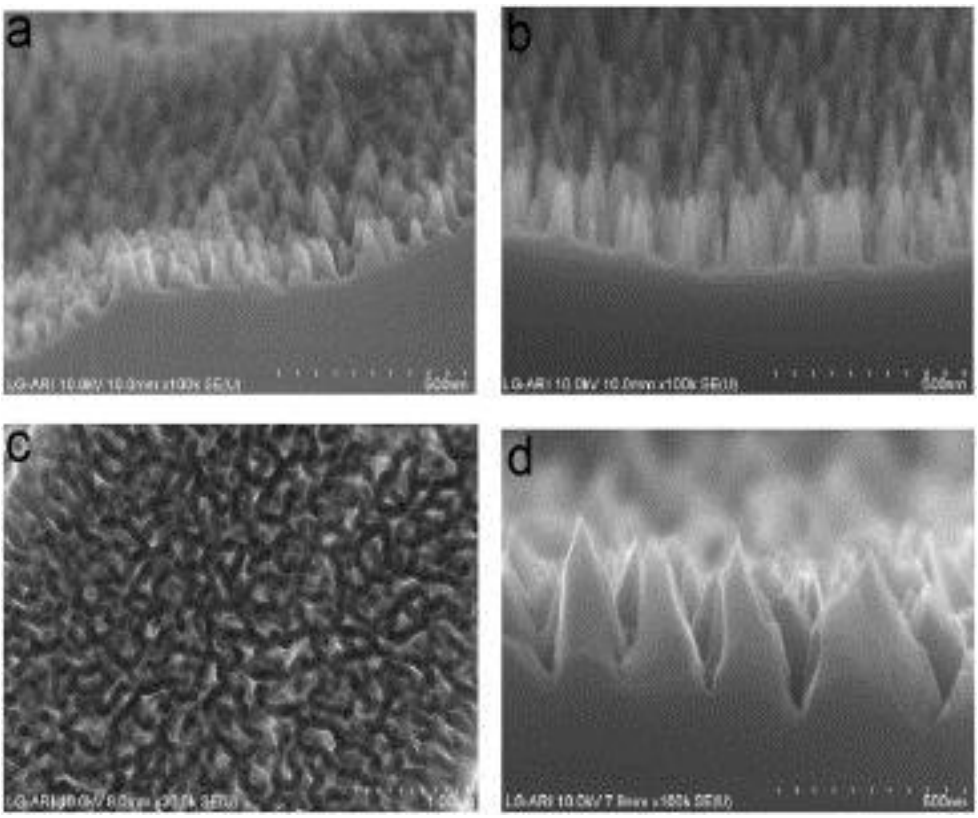

Figure 2.10 SEM pictures of surface structures on silicon wafers after RIE using (a) SF_6/O_2~ 1:0.7, (b) SF_6/O_2~ 1:1, (c) $SF_6/O_2/Cl_2$ mixture and (d) $SF_6/O_2/Cl_2$ mixture top view (taken from [109]).

This process leads to the formation of needle-like structures. The diameters of these structures and the separation between them are small compared to the useful solar wavelengths. Their heights are also comparable with or larger than these wavelengths [110]. This provides the adequate surface roughness to function effectively to trap light. Fig 2.10 shows an SEM image of these structures [109].

Even though this process is very potent in reducing the reflectivity of a silicon substrate and, thereby, increasing the absorbance, it increases the surface area by orders of magnitude. This creates a big challenge to passivate such a large surface area. Surface recombination of carriers can be a major problem in this case.

2.1.5 Laser Texturing

The method of using lasers to texture the surface of a silicon wafer was first published by Zolper *et al* [111]. This technique exploits the ablative properties of textures to remove small amounts of materials from the silicon wafer surface to produce grooves [111] or pits [112]. The pulse widths of these lasers are extremely small: generally in the range of tens of nanoseconds although femtosecond lasers have also been used for such texturing [113-117].

Laser texturing is a two-step process [112]. In the first step, the silicon surface is first sculpted by laser ablation. This gets rid of the bulk of the silicon required for texturing. The depth of the grooves or pits can be controlled by the power of the laser. In the second step, the surface is chemically etched to remove the slag. This leads to the smoothening of the surface and etching away of any residual layer of laser damage.

The etching process must remove all of the ablation slag from the textured surface and remove laser-damaged silicon to prevent the propagation of dislocations into the bulk of the wafer [118]. This etching is done first by an anisotropic etch (NaOH solution) followed by isotropic etching [113], although UV lasers have been used recently where this etching step is not required [119]. Fig.

2.11 shows the surface of a silicon wafer after laser texturing. Note the uniform spikes formed on the surface.

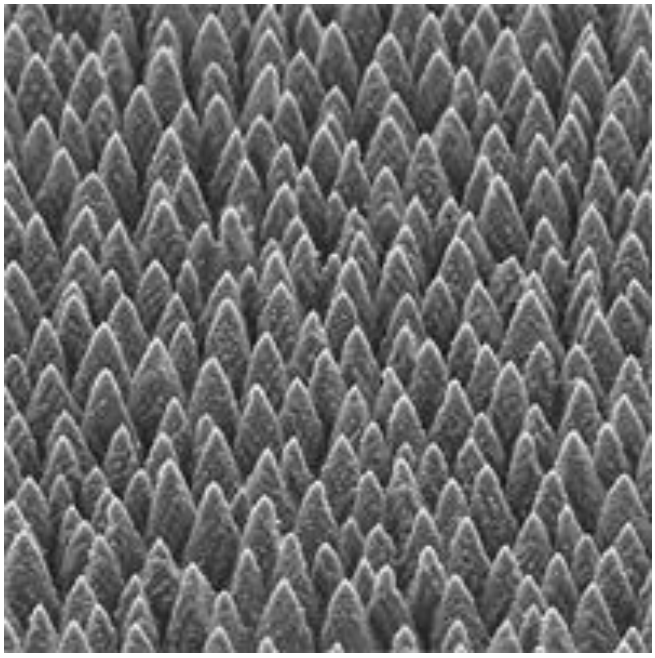

Figure 2.11 SEM image of the surface of a laser textured silicon wafer (taken from [120]).

2.2 Other Light Trapping Techniques

Light trapping techniques, discussed in the previous section, are based on roughening the surface of the silicon substrate to maximize absorption. Randomly roughened surfaces can theoretically enhance the path length of light by fifty [121] times while the best realized result around ten times [122]. These enhancements are sufficient for thick wafer based silicon solar cells. But due to the indirect band gap of silicon and hence, the low absorbance, this enhancement is entirely inefficient for thin film silicon solar cells.

Many light trapping techniques other than texturing have been developed for thin film silicon solar cells. This section will give a brief overview and review of these technologies relevant for silicon photovoltaics.

2.2.1 Diffraction Gratings

A repetitive array of diffracting elements, either apertures of obstacles, that has the effect of producing periodic alterations in the phase, amplitude, or both of an emergent wave is said to be a *diffraction grating* [123]. The grating equation states that:

$$m\lambda = np(\sin\alpha + \sin\theta), \tag{2.8}$$

where, m is the diffraction order in integers, λ is the incident wavelength, n is the refractive index of the material, p is the period of the grating, α and θ are the incidence and the diffraction angles, respectively.

In the case of rectangular gratings, for grating etch depth $t=\lambda/4n_{Si}$, n_{Si} being the refractive index of silicon, the zeroth order reflection is strongly suppressed while the 1-order diffractions are left intact, bent by 90°. Proper designing of diffraction gratings at the back side of a solar cell can bend the first order reflection exceeding the critical angle of total internal reflection of silicon (16.6°). This leads to total internal reflection at the front surface of the cell, thereby, enhancing the absorption in the active region.

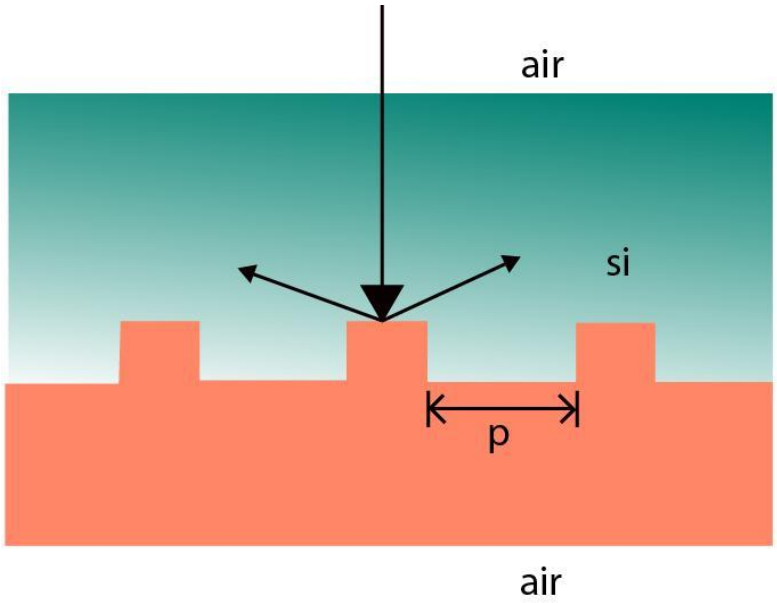

Figure 2.12 A solar cell design with diffraction grating at the back. '*p* 'is the period of the grating, 'si' is silicon while +1 and -1 are the respective order reflections from the back surface.

This technique has been employed by many research groups to enhance the absorption in thin film silicon solar cells (e.g.,[124-126]). Fig. 2.12 shows a standard structure with diffraction gratings at the back surface.

2.2.2 Photonic Crystals

A photonic crystal is a periodic arrangement of dielectric or metallic material with a lattice constant comparable to the wavelength of an electromagnetic wave. A detailed description on this can be found in [127]. This category of materials came into limelight after the publications by Yablanovitch [128, 129] and John [129]. Photonic crystals are regularly repeating areas of high and low dielectric constants. Photons, behaving as waves, either propagate through this structure or they do not, depending on their wavelength. Wavelengths of light that are allowed to travel are known as modes, and groups of allowed modes form bands.

Disallowed bands of wavelengths are called photonic band gaps. The repeating structures of dielectrics can be 1-D, 2-D or 3-D [130].

A typical back reflector in a silicon cell consists of aluminum. Such metallic back reflectors suffer from intrinsic losses from surface plasmon modes generated at the metal-dielectric interface. These losses accumulate rapidly and are even more severe at longer wavelengths. This can be overcome by using a distributed Bragg reflector at the back interface (e.g.,[131-133]). A distributed Bragg reflector (DBR) is an example of a 1-D photonic crystal that has been utilized for light trapping in thin film silicon solar cells. Such a reflector has a very high reflectance with a very low absorption loss.

A DBR has a wide stop band [134] expanding several hundred nanometers with almost 100% reflectivity. Simulations for DBR stacks of Si/Si_3N_4 (n_1/n_2=3.5/2.0) or Si/SiO_2 (n_1/n_2=3.5/1.46) have shown reflectivity of >99.8% for wavelength between 800 and 1100 nm with just a few quarter-wave pairs [133] in contrast to the standard aluminum back reflector with a reflectivity of <80%. A DBR, when coupled with a diffraction grating or a textured back surface gives even better light trapping capabilities. This is due to the simultaneous, almost total back reflectance coupled with almost total internal reflection at the front surface, thereby, increasing the optical path length of light inside silicon by 10^4 times [133]. Fig 2.13 shows these three cases [135].

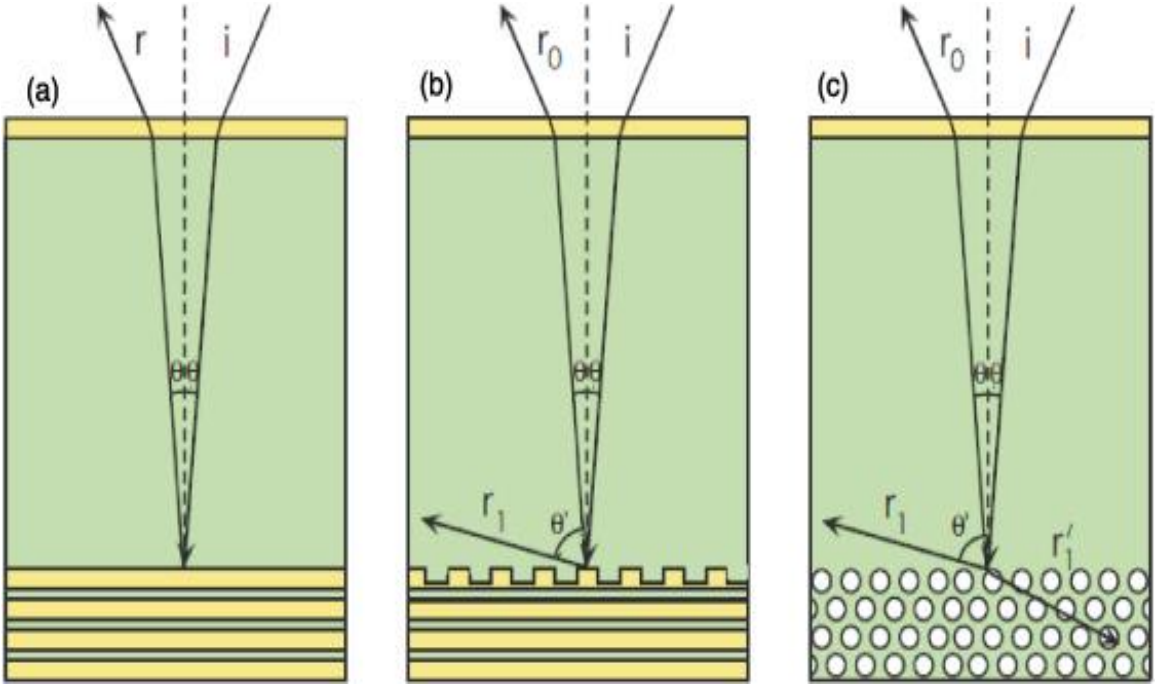

Figure 2.13 Illustration of three solar cell designs: (a) a simple design with a distributed Bragg reflector (DBR), which displays only spectral reflection, (b) a DBR plus a periodically etched grating, displaying spectral reflection and diffraction, and (c) a photonic crystal consisting of a triangular lattice of air holes, displaying simultaneous reflection, diffraction and refraction from the photonic crystal layer. Crystalline silicon is in the light green, low dielectric in light grey and air is transparent (taken from [135]).

2.2.3 Plasmonic Solar Cells

A novel method for increasing light absorption in thin film silicon solar cells that has emerged comparatively recently is the use of scattering from noble metal nanoparticles excited at their surface plasmon resonance. This is called the *Plasmonic Effect*.

Interest in the plasmonic effect has intensified over the last few decades, mainly due to the discovery that Raman scattering can be magnified many times through the use of metal nanostructures [136, 137]. Stuart and Hall [138] did pioneering work in the field of plasmonic enhancement of light-sensitive devices

when they showed that an enhancement in the photocurrent by a factor of 18 could be achieved for a 165 nm thick silicon-on-insulator photo-detector at a wavelength of 800nm using silver nanoparticles on the device surface. Later, Schaadt *et al*. [139] obtained enhancements of up to 80% at around 500nm wavelength of light in highly doped wafer based silicon solar cells deposited with gold nanoparticles. Derkacs *et al*. [140] also achieved an overall increase in conversion efficiency of 8% in thin-film amorphous silicon solar cells by depositing gold nanoparticles on the surface. Pillai *et al*. [141] reported a sevenfold enhancement for wafer-based cells at λ=1200 nm and up to 16-fold enhancement at λ=1050 nm for 1.25 μm thin silicon-on-insulator (SOI) cells when deposited with Ag. Figure 2.14 shows a schematic of the plasmonic effect.

The photocurrent enhancement by metal particles incorporated into or on solar cells has been explained by two main basic mechanisms:

- Light scattering by metal nanoparticles, and
- Near-field concentration of incident light.

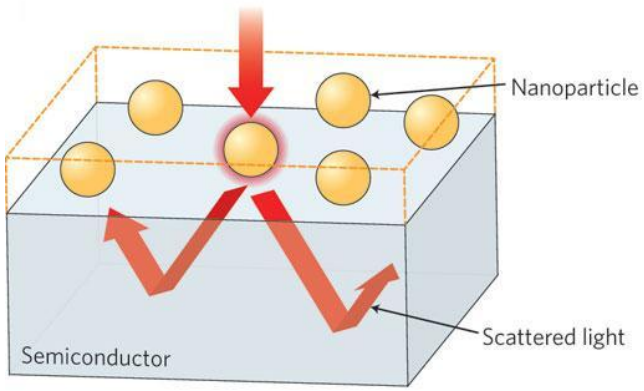

Figure 2.14 A schematic of the plasmonic effect (taken from [141]).

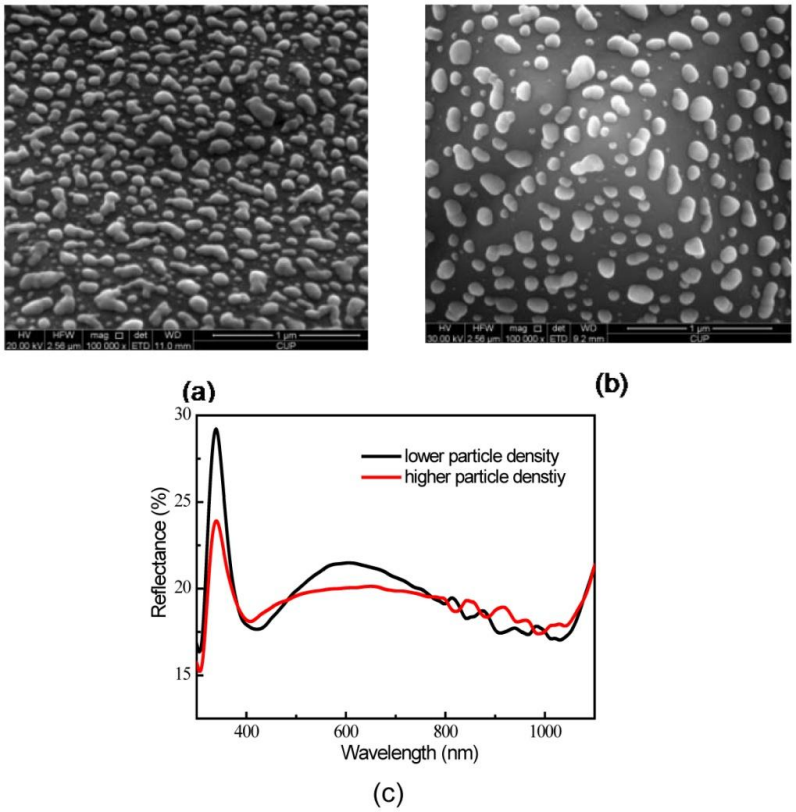

Figure 2.15 SEM results and surface reflectance properties of the structure with different densities of Ag nanoparticles on the surface. (a) SEM image of sample with higher particle density. (b) SEM image of sample with smaller particles density. (c) Surface reflectance with different particle densities. (taken from [142])

Out of these two, scattering by metal particles has been the main mechanism for enhancement of most reported experimental work. A detailed description of the theory behind the scattering of light by plasmonic effect can be found in ref. [143]. Figure 2.15 shows SEM images of silver nanoparticles on silicon along with the optical reflectance curves.

2.3 Ray Tracing Simulations for Solar Cells: A Brief Review

For solar cells to become economically competitive with the conventional sources of energy, optimizing their cost of production and efficiencies are of vital importance. Proper optical and electrical design of solar cells and modules is one

of the major methods of achieving a harmony between cost and efficiency. While there exist established commercial photovoltaic electrical modeling tools such as PC1D [144] and AFORE-HET [145, 146], such optical modeling tools that can handle complete solar cell structures do not exist. Some important photovoltaic optical modeling tools available include: ray tracing softwares such as PV Optics [50], BIRANDY [147], SUNRAYS [148], Texture [149], and APSYS [150, 151]. The first four software models can only handle 2-D structures using ray tracing and lack options to include front metal architecture. APSYS, on the other hand, integrates electrical and optical modeling for semiconductor devices including solar cells, integrating Finite Element Analysis for electrical modeling with ray tracing for optical modeling. Since this software is not photovoltaic specific, it is not widely used by the PV community. This leaves a lot of room for introducing front metal architecture into existing photovoltaic software packages.

Even though, as explained in the first chapter of this dissertation, ray tracing has been used extensively for rendering computer graphics and lens design, it has also found several applications in optical modeling of solar cells. The first mention of ray tracing to study absorption of light in solar cells was made by Redfield [152], which was followed by Yablanovitch [153] stating that an enhancement of $4n^2$ (n is the refractive index) could be achieved by efficient light trapping. The first study on light trapping of pyramidal textured silicon surfaces was done by Campbell *et al* [55]. This was preceded by a ray tracing study on light trapping of anisotropically etched III-V solar cells [154].

Texture, the ray tracing photovoltaic software mentioned in the beginning of this section was released subsequently [149]. Wang *et al* subsequently used ray tracing to study the light trapping capabilities of a PERL cell [155]. Smith *et al.* later conducted a ray trace study of inverted pyramid texturing geometry and reported its higher path length enhancement compared to pyramids and slats [53].

SUNRAYS was released later which was used by Brendel to study the light coupling into mechanically textured silicon solar cells [156]. Thorp *et al.* also studied the light trapping in thin-film crystalline silicon solar cells deposited on glass with a range of metal and detached reflectors at the back along with bifacial modules which led them to conclude that a J_{sc} of 34-35 mA/cm^2 could be achieved under real conditions for a 10µm thick silicon film [147].

During this time, PV Optics was released as well [157]. This revolutionized the field of software related to photovoltaics as it provided many more features than any others in the market. Along with many new features, PV Optics added the capability to model textured surfaces of varying angles with a two layer anti-reflection (AR) coating [158]. This was followed by Nishimoto *et al.* conducting an investigation into the light trapping characteristics of acid textured multicrystalline silicon solar cells and found that the reflectance is directly dependent on the quotient of the depth and the width of the texture [159].

Rodriguez *et al.* [160] were the first to propose a model for ray tracing calculations on random pyramidal textured surfaces, using it to find that no metal coating was necessary for a strong confinement of light within the silicon layer.

This model has been used extensively over the years. Figure 2.16 shows one unit texture made using this model, where α is the fraction of the untextured area, L_T is the side of the enclosing cell and L is the base of the pyramid. Figure 2.17 shows a random pyramidal surface obtained using this model. This model was recently used by Baker-Finch *et al.* to include polarization effects to optimize refractive index of AR coatings for randomly textured silicon solar cells [161].

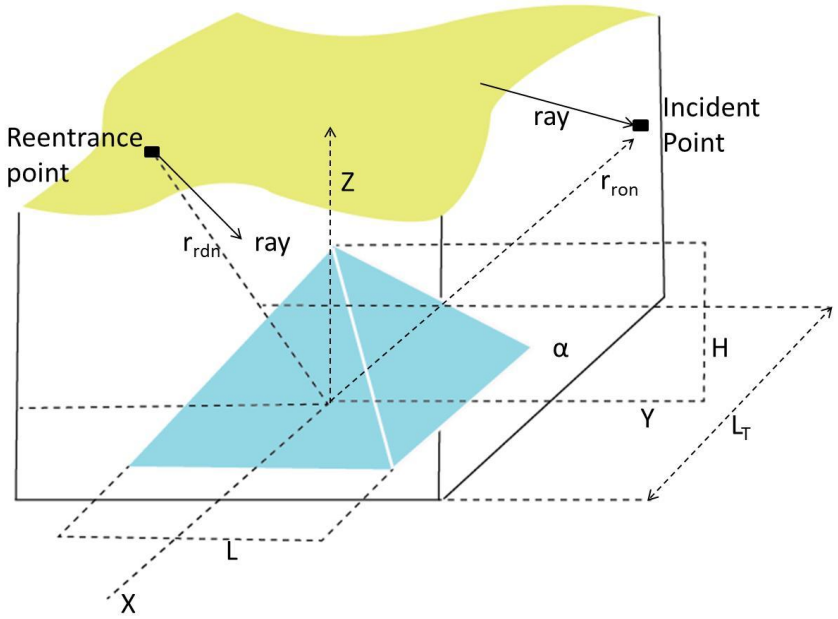

Figure 2.16 *Unit cell***.** In regular textures, the ray reenters through a point that is symmetrical to the incident point. Reconstructed from [160].

Alkaline texture etching of (100) oriented silicon wafers is a standard procedure for manufacturing single crystal silicon solar cells to reduce reflectance and increase their efficiency. This kind of etching, being anisotropic in nature, results in unique textures for each orientation. In the case of multicrystalline silicon wafers, since the grains are randomly oriented, it leads to texture shapes on the surface of each grain that directly correspond to its crystal orientation leading to a unique reflectance value for each crystal orientation. This

provides an opportunity to ascertain the orientation of each grain by the shape of the textures formed on its surface and its corresponding reflectance value.

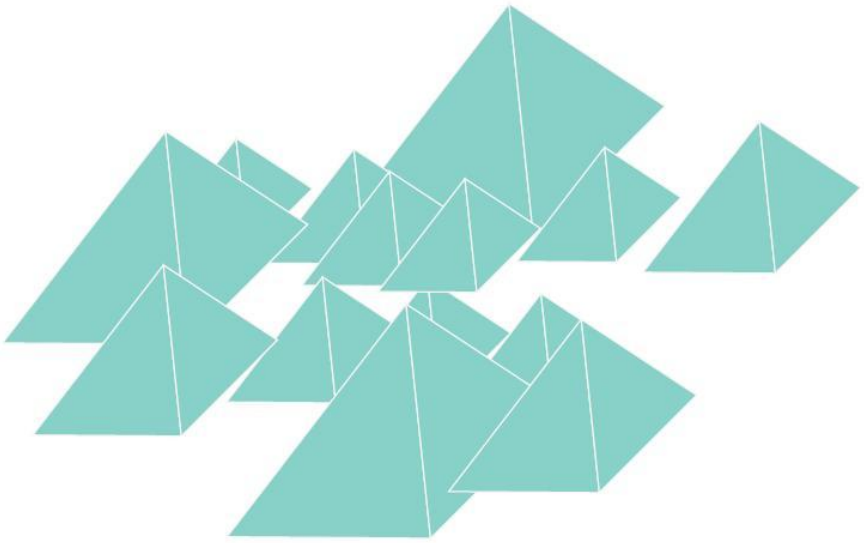

Figure 2.17 Random pyramid surface using Rodriguez's model. Reconstructed from [160].

2.4 Reflectance Calculations of Alkaline Textured Multicrystalline Silicon

The random texturing model given by Rodriguez *et al.* [160] is extended to handle textures for all crystal orientations. A rigorous 3D ray tracing computation is carried out for multiple low index orientations to calculate their reflectance leading to a model for calculation of the total reflectance of a complete 6"X6" multicrystalline silicon wafer. Calculations have also been done for all crystal orientations at a wavelength of 633 nm for a He-Ne laser source to make a one-to-one orientation-to-reflectance map to aid in ascertaining the crystal orientation of each grain by optical reflectance rather than by X-ray Laue patterns or EBSD (Electron Back Scattering Diffraction). The calculated results have been verified

experimentally for each grain along with their crystal orientations. The simulations and experimental results show an excellent agreement [86, 162].

2.4.1 Introduction

Multicrystalline silicon has become the most important base material for silicon solar cells in recent years [89]. This has led to a huge interest in ways to improve the electronic properties of this material. Multicrystalline silicon consists of grains of varying sizes and crystal orientations. It is known that grain boundaries act as carrier recombination centers with the recombination activity dependent on the grain boundary angles [163]. Hence, decreasing the grain boundary area and angles in a multicrystalline silicon wafer is of vital importance in order to improve performance of devices made on these substrates. This makes it imperative for crystal growers to control and optimize the growth parameters of multicrystalline silicon for better material quality and electrical performance. A thorough knowledge of the correlation between crystal growth conditions and grain orientations and grain boundary angles is also desirable. A fast and accurate technique to determine these parameters for a multicrystalline silicon wafer becomes even more important. As has been recently shown [59], the orientation dependence of anisotropic etchants like potassium hydroxide solutions can be exploited towards this end. The difference in reflectance of various grains can also be utilized to increase the contrasts between grains in an optical image and, thereby, used to calculate grain sizes and their distributions by employing image processing techniques [59].

Even though wet chemical isotropic etching has been used in the silicon semiconductor industry during processing since the 1950's [68, 69], it took a little while longer for anisotropic etching of silicon to follow suit [70, 71]. But it was only during the mid-1970's that this process was first introduced for silicon solar cell processing [72]. It is known that the (111) direction has the slowest etch rates [69] to alkaline etches compared to all other orientations. The comparative etch rates of the basic orientations are $R_{100}>R_{110}>R_{111}$, where R_{hkl} is the etch rate in a specific crystallographic direction. This phenomenon results in the exposure of the family of (111) planes nearest to the surface of the silicon substrate, when etched anisotropically for a suitable duration of time.

In order to exploit the anisotropicity of alkaline etches towards silicon to the fullest, a computer program, written in C++, has been developed to model the textured surfaces of any arbitrarily oriented grain and perform rigorous ray tracing simulations to calculate their reflectance. This model is based on the one given by Rodriguez *et al* [160] for random textures on a (100) silicon surface after anisotropic etching, which has been extended to handle textures on silicon surface of any arbitrary crystal orientation after an alkaline etching process. This model is presented here in detail, as there exist nothing in the literature that handles this topic satisfactorily. Furthermore, the technique of ray tracing, being a standard process for optical computations in solar cells [50], is not elaborated in depth. The results of the calculations are also compared with the experimental data available in the literature.

2.4.2 Modeling Textured Silicon Surface

The anisotropic etching of silicon using KOH exposes the family of (111) planes nearest to the crystal surface. The vectors binding these planes are used to define these (111) planes. Fig. 2.18 shows this family of planes in the orthogonal coordinate system. The texture shape is completely dependent on the orientation of the grains in a multicrystalline silicon wafer relative to these planes.

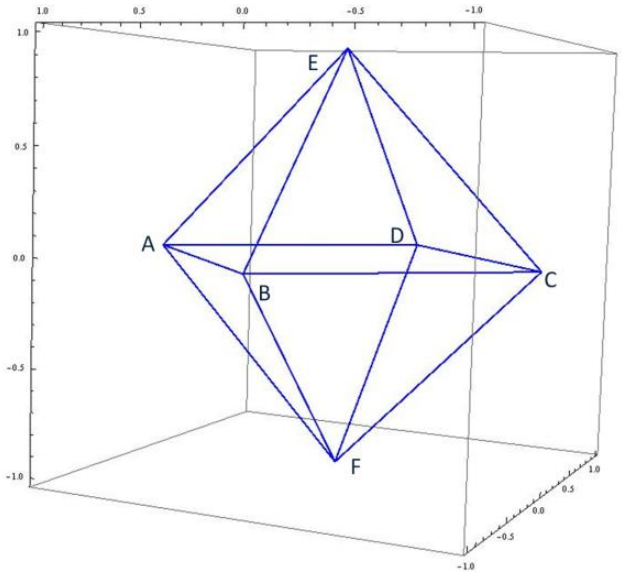

Fig. 2.18: The family of eight (111) planes with respect to the X, Y and Z-axes. The eight planes are ABE, ADE, CDE, BCE, ABF, ADF, CDF and BCF. The planes are symmetric about each of the six vertices, A, B, C, D, E and F.

The blue lines signify the edges of each plane. It should be noted that these planes form two pyramids, one inverted while the other vertical. The set of binding lines for each plane are used as reference to ascertain the texture shape for any given crystal orientation. The points of intersection in Figure 2.18 are marked from A-F. The lines are defined as follows for a texture of unit height of:

$$\overrightarrow{EA} = 0\hat{\imath} - 1\hat{\jmath} - 1\hat{k} \tag{2.9}$$

$$\overrightarrow{EB} = 1\hat{\imath} + 0\hat{\jmath} - 1\hat{k} \tag{2.10}$$

$$\overrightarrow{EC} = 0\hat{\imath} + 1\hat{\jmath} - 1\hat{k} \tag{2.11}$$

$$\overrightarrow{ED} = -1\hat{\imath} + 0\hat{\jmath} - 1\hat{k} \tag{2.12}$$

$$\overrightarrow{FA} = 0\hat{\imath} - 1\hat{\jmath} + 1\hat{k} \tag{2.13}$$

$$\overrightarrow{FB} = 1\hat{\imath} + 0\hat{\jmath} + 1\hat{k} \tag{2.14}$$

$$\overrightarrow{FC} = 0\hat{\imath} + 1\hat{\jmath} + 1\hat{k} \tag{2.15}$$

$$\overrightarrow{FD} = -1\hat{\imath} + 0\hat{\jmath} + 1\hat{k} \tag{2.16}$$

In order to define the surface textures, the crystallographic plane parallel to the wafer surface is also defined mathematically. These planes are denoted in terms of the angle that the normal to the surface of a plane from the origin makes with the X-Y plane and the azimuth. Figure 2.19 shows these two angles used for calculations.

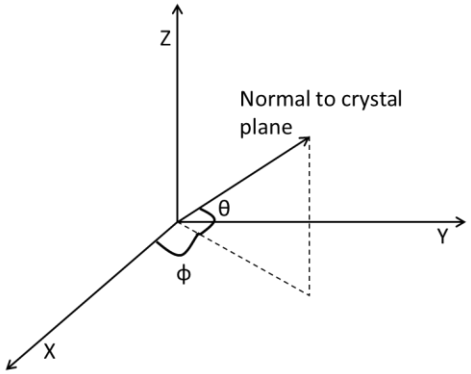

Fig 2.19 The angles θ and φ for the unit normal to the crystallographic plane.

Thus, the surface of a grain of a known orientation can be expressed as a 3D plane passing through the origin and defined in terms of the angles θ and Φ using the equation:

$$z\ \sin\theta = -x\ \cos\theta\cos\varphi - y \tag{2.17}$$

Table 2.1 θ and φ for some low index crystallographic orientations.

Crystal Plane (hkl)	θ	φ
(100)	0°	0°
(310)	0°	18.435°
(210)	0°	26.565°
(311)	17.55°	18.435°
(211)	24.09°	26.565°
(321)	15.5°	33.69°
(110)	0°	45°

(221)	19.47°	45°
(331)	13.26°	45°
(111)	35.265°	45°

where, r is length of surface normal and all the other symbols have their usual meanings. This plane is then translated away from the origin, depending on the desired textured height. Table 2.1 provides the values of θ and φ for some of the low index crystal planes.

The silicon crystal lattice system, being cubic, has a high degree of symmetry. This feature is used to narrow down the entire range of orientations to only a small part of the θ and Φ coordinate system, which is sufficient to represent the entire range of orientations. The shaded area in the graph of Figure 2.20 depicts the area of the cubic lattice system that sufficiently represents all the possible families of crystal planes [164]. This part of the orientation range is bounded by (100), (110) and (111) planes respectively on each side.

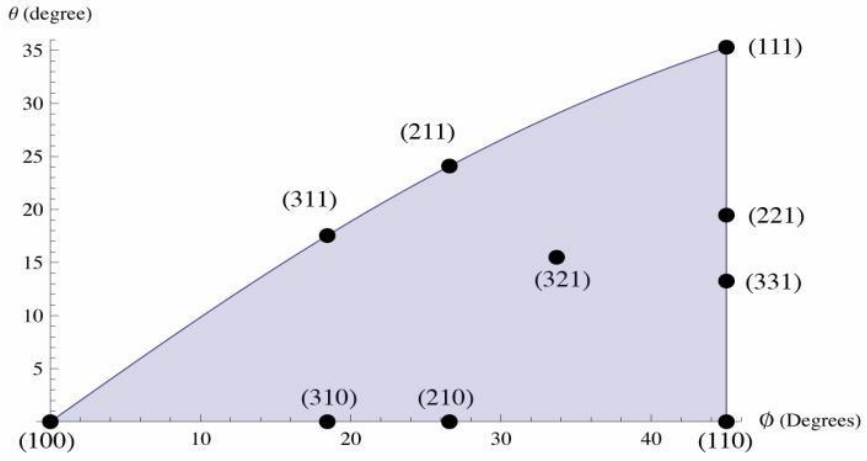

Figure 2.20 Part of θ and Φ coordinate system used for calculations. Some low index crystal orientations are marked for reference.

The determination of the textured surface is based on what is defined as a *Unit Texture*. A unit texture is one that is formed by the intersection of the nearest (111) planes with the silicon crystal surface orientation plane. Such multiple unit textures, when juxtaposed side-by-side, form a periodic anisotropically etched silicon surface. The unit texture shape is calculated by the points of intersection of the vectors forming the (111) planes with the equation of the crystallographic planes, as given in Eq. 2.17. Figures 2.21(a) and (b) depict this process of unit texture formation for (210) crystallographic plane.

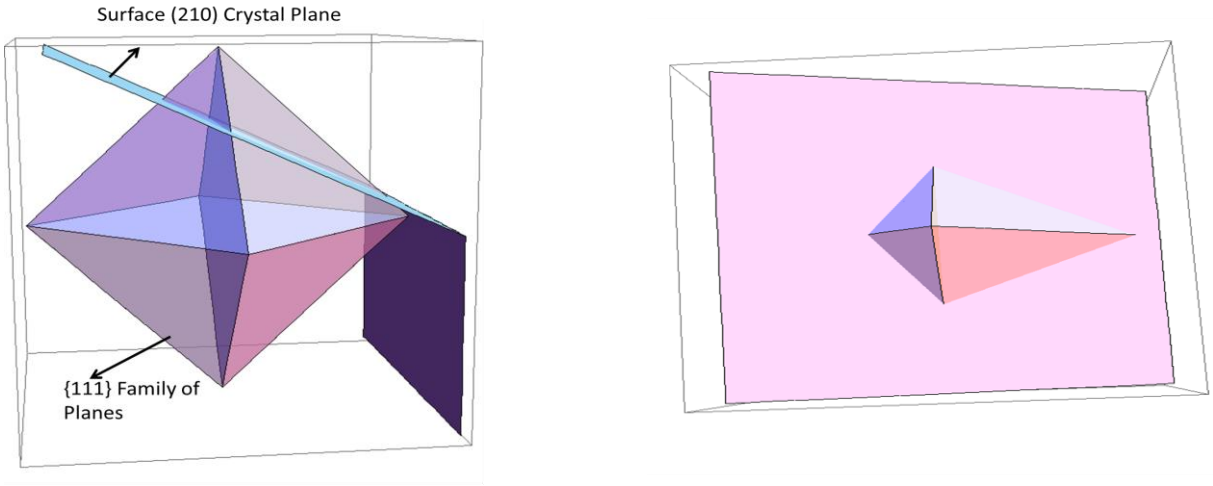

(a) (b)

Figure 2.21 (a) Intersection of the family of (111) planes with the (210) crystal plane, (b) top view of unit texture thus formed.

The (210) plane calculated using Eq. 2.17 passes through the origin. Hence, it is translated along the unit normal from the origin to the plane, so that it intersects the (111) planes only on one side of the X-Y plane. This is shown in Figure 2.21(a) where the surface (210) crystallographic plane is offset from the origin by a unit length normal to it from the origin. Figure 2.21(b) shows the top view of the part of the (111) planes above the (210) plane. The base of the unit

texture so calculated does not coincide with the X-Y plane. For ray tracing computations, the complete silicon wafer structure is made parallel to the X-Y plane. In order to make it lie on the horizontal, 3D rotation matrices [165] are used to rotate the unit texture by θ and φ along the respective axes. Adjusting the intersection points of the unit texture to get the desired texture height follows this step. Once the unit texture is calculated, such multiple structures are placed side by side to form a 4X4 array of surface texture. Figure 2.22 shows the calculated textured surfaces for three low index orientations. These are compared with the data from the literature in the same Figure. The calculated unit textures are the same as those produced upon etching, even though texture coverage area on the silicon surface is dependent on the etching solution and conditions. Using proper etch masks along with etch conditions would lead to surface textures resembling very closely to the calculated periodic textures. Figure 2.23 shows the calculated periodic surface textures for a few other low index crystallographic orientations.

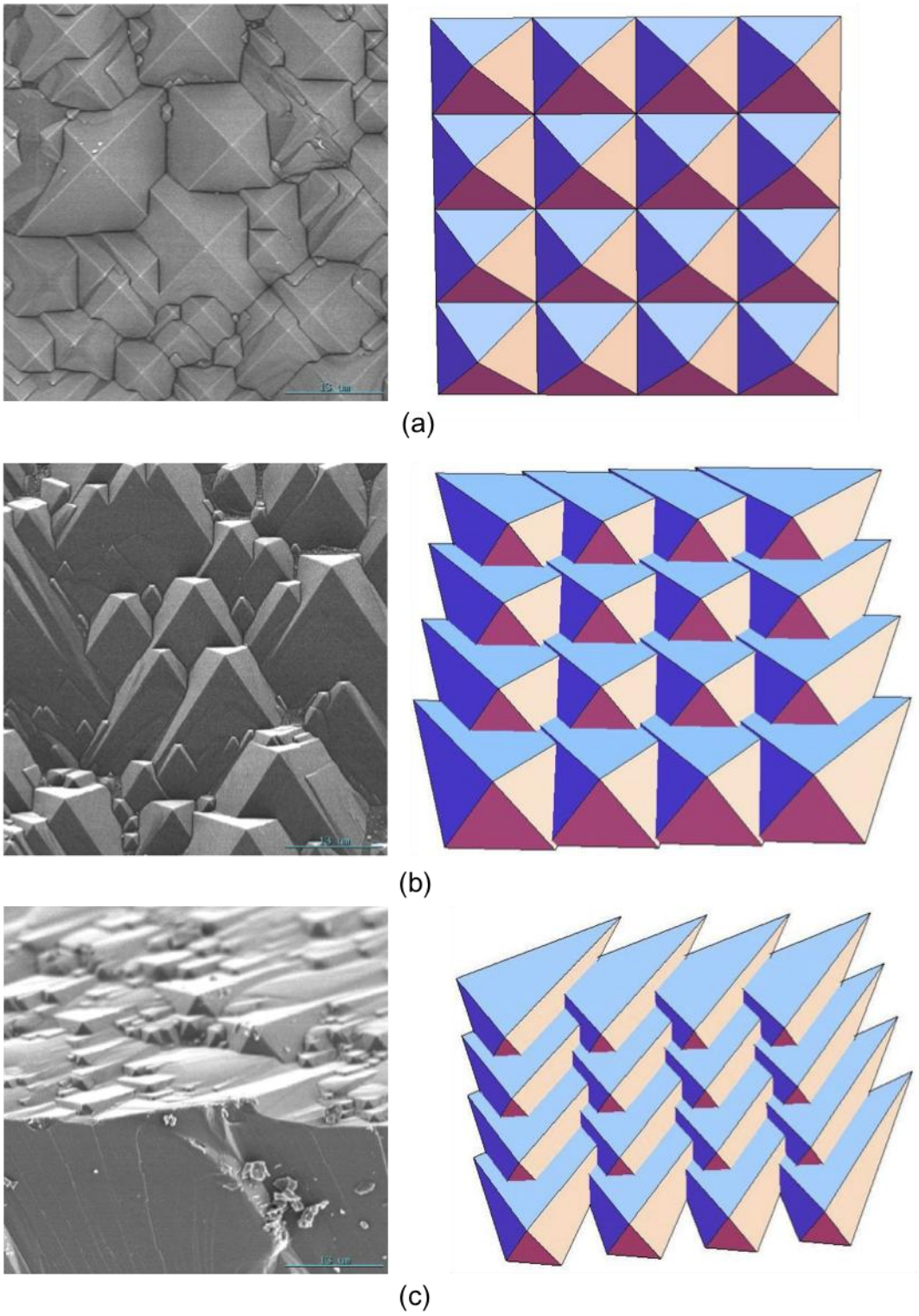

Figure 2.22 SEM images of textured surfaces on the left (taken from [86]) and calculated periodic surface textures on the right for: a. (100), b. (311) and c. (321) crystal orientations.

2.4.3 Ray Tracing algorithm

Ray tracing computations have been done for hemispherical reflectance and transmittance. The structure for reflectance computations consists of the wafer structure constituted by (a) textured front surface, (b) textured back surface, (c) the entire thickness of of the silicon wafer, and the detectors where rays are captured when they leave the wafer, consisting of (d) detector plane on the top to capture reflected rays and (e) detector plane at the bottom to capture the transmitted rays. The wavelength range for computation is from 0.4 µm-1.1 µm. Rays are incident on the middle portion of the texture array for these calculations.

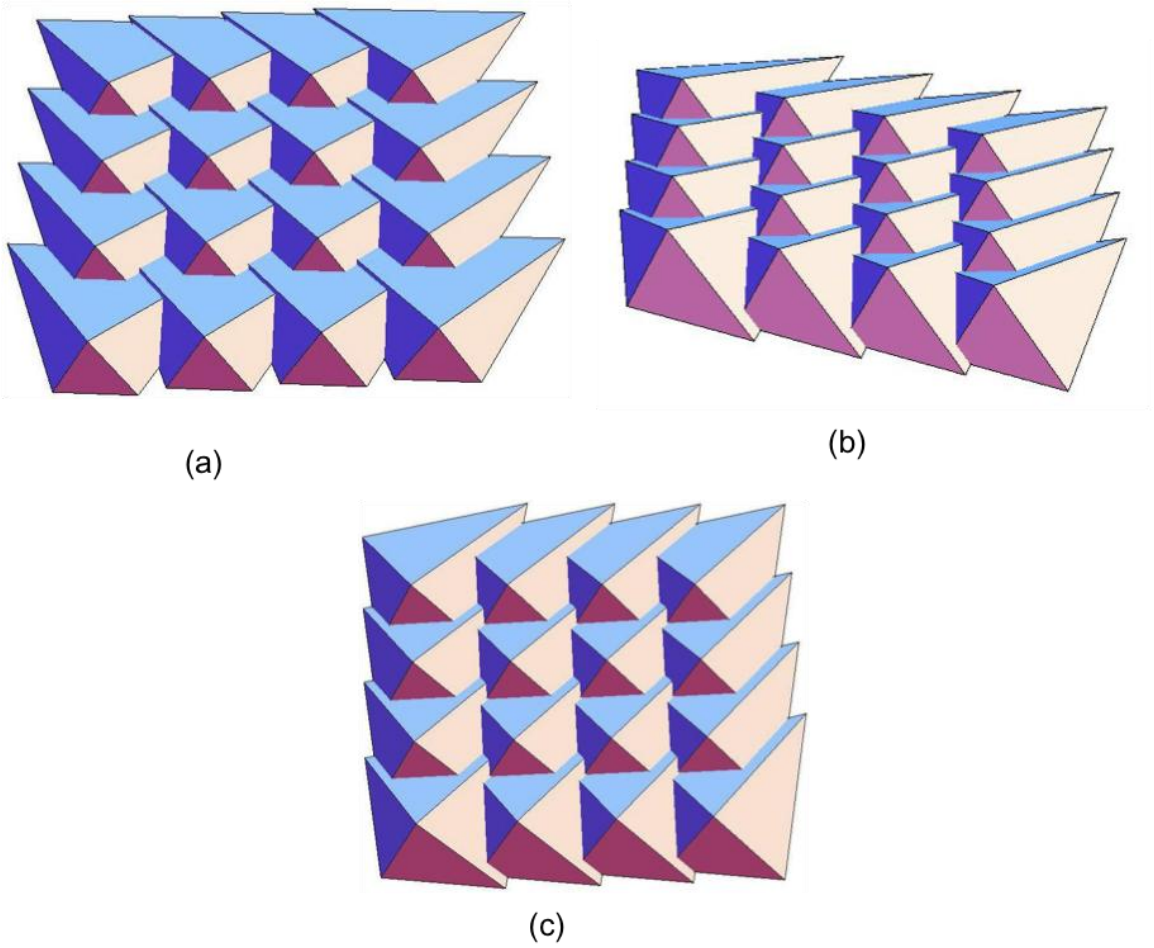

Figure 2.23 Calculated periodic textures for anisotropically etched a. (211), b. (210) and c. (310) silicon.

Each ray is tracked while it bounces about the surface, or gets transmitted into the wafer, till a detector above or below the wafer captures it or when its intensity becomes less than 0.001, or 0.1% of its original intensity. Figure 2.24 shows the full structure including the bounding planes for a (100) texture etched silicon wafer. The sidewalls are made translucent for better representation.

Fig. 2.24 shows the full structure including the bounding planes for a (100) texture etched silicon wafer. The sidewalls are made translucent for better representation.

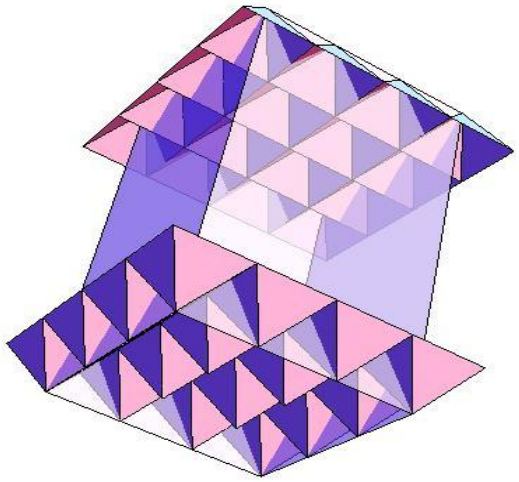

Figure 2.24. The full structure including the sidewalls for periodic boundary condition for a (100) silicon wafer.

All the calculations are done within this structure itself by enforcing the periodic boundary condition. Any ray that is incident on one of the sidewalls is brought back into the structure again from the opposite side by keeping ‘Z’ coordinate constant. At every step, the unit vector (direction cosines) and intensity of the ray is updated and the points of intersection are checked for each of the constituents of the structure shown in Figure 2.24. At any given step, there

will be multiple intersection points with many constituents of the wafer structure. Each point of intersection is checked for validity, i.e., whether it lies within the structure and not outside it, and whether it lies in a region shaded by another structure, till the correct intersection point is identified. The reflection coefficient is also calculated at every valid intersection point. If the ray hits one of the bounding side planes, the reflection coefficient is taken to be 0 while the transmission coefficient is taken to be 1. When the ray gets inside silicon, its intensity is reduced depending on the absorption coefficient of silicon for the wavelength of incident light under calculation.

The reflection and transmission coefficients formulae have already been discussed in Chapter 1 of this dissertation. The intensity of the ray is diminished upon absorbance by:

$$I = I_o e^{-\alpha \boldsymbol{r}.\boldsymbol{s}} \tag{2.18}$$

where, $\alpha = \frac{4\pi}{\lambda} k$ is the absorption coefficient and k is the extinction coefficient. Finally, the reflectance for the entire surface is given by:

$$R_{tot} = \frac{\sum_{i=0}^{n} R_{fi}}{n} \tag{2.19}$$

where, R_{fi} is the final reflection coefficient of the *i*th ray, R_{tot} is the total reflectance of the textured surface and n is total number of incident rays. This entire sequence of calculations is carried out till all the incident rays have either

been absorbed by the substrate or captured by one of the two detectors. The flowchart of the ray trace algorithm, implemented in C++, is shown at the end.

2.4.4 Results and discussion

Two types of calculations have been presented for different purposes:

(1) Complete reflectance curves are shown for seven low index crystallographic orientations due to constraint of space. These are: (100), (110), (111), (210), (310), (311), and (211). These reflectance values are compared with a polished silicon wafer.

(2) Calculations have also been done for silicon in the entire range of crystallographic orientations for a wavelength of 633 nm He-Ne laser source.

Figure 2.25(A) shows the calculated reflectance curves for periodically textured wafers with thickness of 180 μm and texture height of 3 μm while Figure 2.25(B) shows the measured reflectance curves taken from the literature for initial silicon thickness of 525 μm [86]. The trends in the reflectance curves are very similar. The quality of texturing and the texture coverage on the surface of silicon have a very important effect on the reflectance from silicon surface. The variations in the reflectance between the calculated and measured values are attributed to this. A more uniform texturing process than the one used in reference [86] would result in very close match with the calculated values.

Figure 2.26 shows the 3D reflectance curve at a wavelength of 633 nm for crystal orientations spread out in the region shown in Figure 2.20. Silicon, with an orientation of (111), has the highest reflectance while the one at (100) has the lowest reflectance with (110) having a reflectance value in between these two. This is a unique curve where no two points have the same reflectance. The curve increases monotonically from (100) to (111) and also from (110) to (111). This

provides a validation to the technique of using the hemispherical reflectance of textured multicrystalline grains to ascertain their orientation.

(A)

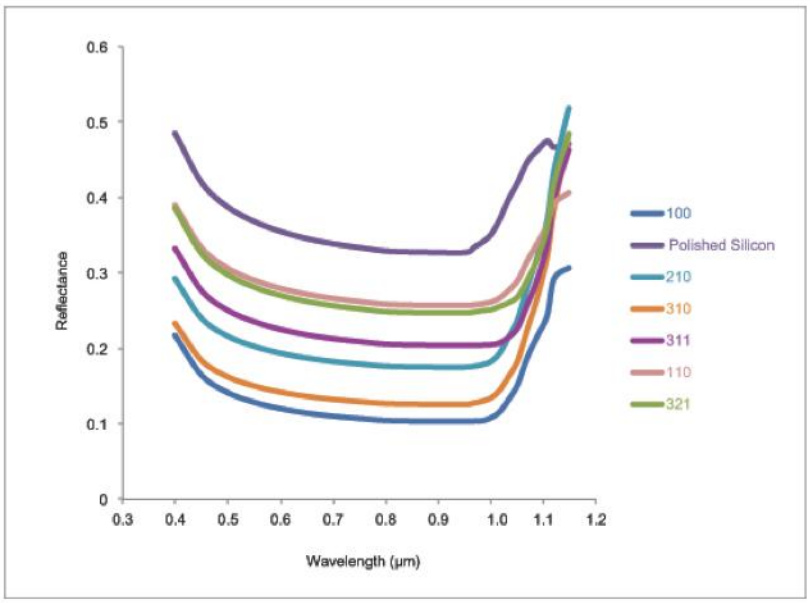

(B)

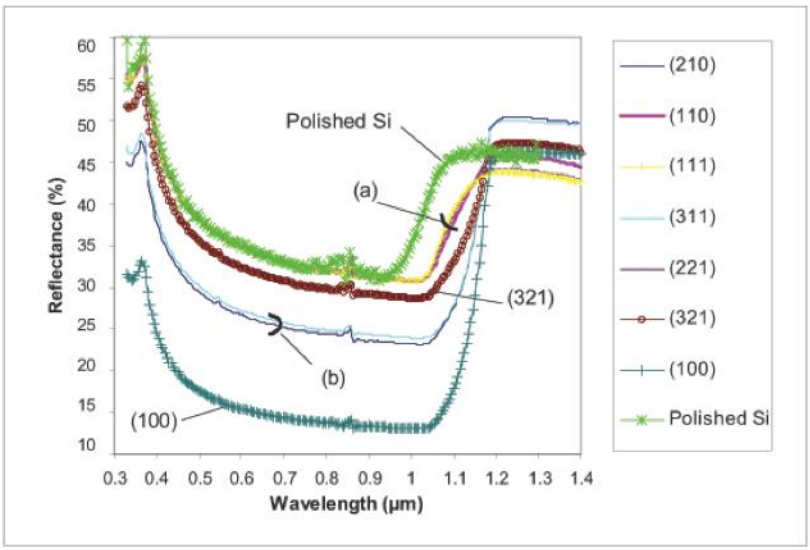

Figure 2.25 (A) Calculated reflectance curves for a few alkaline texture-etched low index crystallographic orientation and polished silicon, (B) Reflectance in air for the texture etched wafers (initial thickness ~525 μm) compared to polished 100 μm silicon. (a) (111), (221) & (110), (b) (311) & (210) orientations [86].

2.4.5 Conclusions

A versatile algorithm to model the texture shapes on alkaline texture etched silicon of any arbitrary (hkl) orientation has been developed. This model has been implemented in a computer program written in C++ to calculate the reflectance of individual grains of a texture etched multicrystalline silicon wafer. Calculated results for various silicon crystal orientations show that the reflectance of alkaline texture etched individual grains can be used to ascertain their crystal orientation with a high degree of accuracy. This, however, would be dependent on the quality of surface texture produced after the etching process.

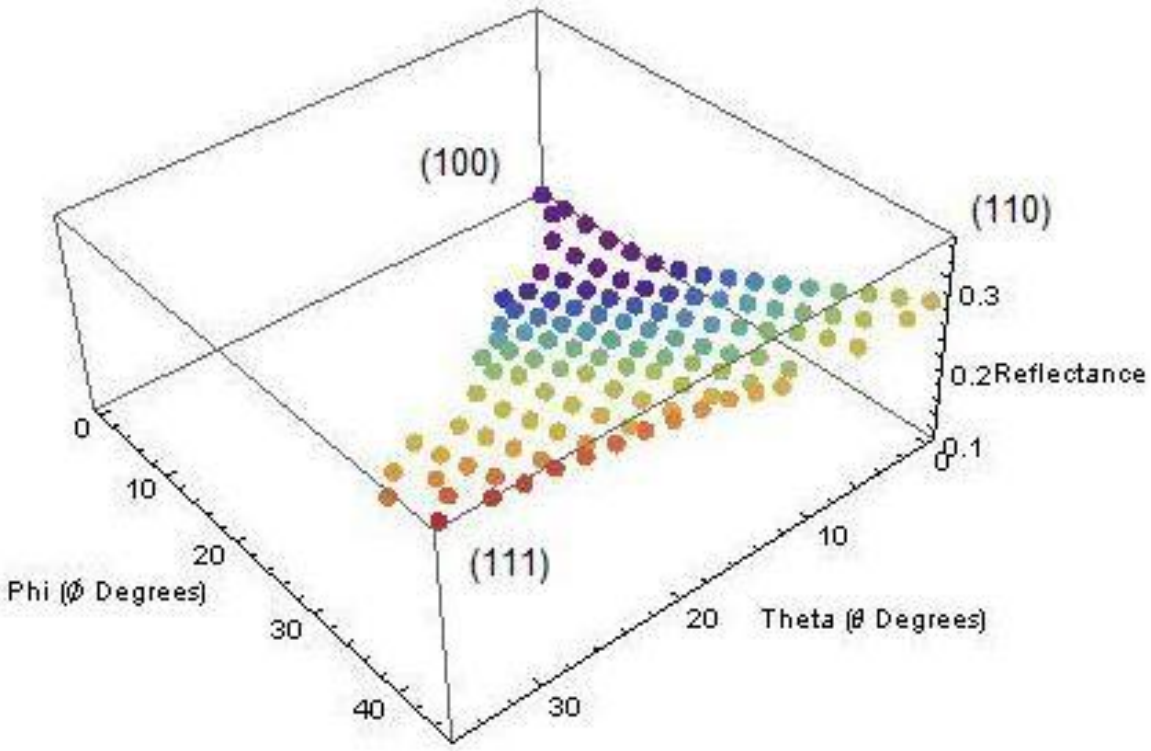

Figure 2.26 The reflectance graphs for numerous alkaline texture etched silicon crystal orientations.

2.5 Summary

In this chapter, a brief overview of various light trapping schemes have been provided. This has been supplemented with an overview of the developments in the field of ray tracing computations for solar cells. The work done by the author of this dissertation to calculate the reflectance of alkaline texture etched multicrystalline silicon wafers and its subsequent use to develop a new and ultra-fast grain orientation mapping technique has also been presented in detail. It is very clear from the literature that optical modeling, using ray tracing, is a powerful tool for the design of solar cells and modules and this chapter will serve as a prelude to the detailed explanation of the new optical model developed for simulations in finished solar cells.

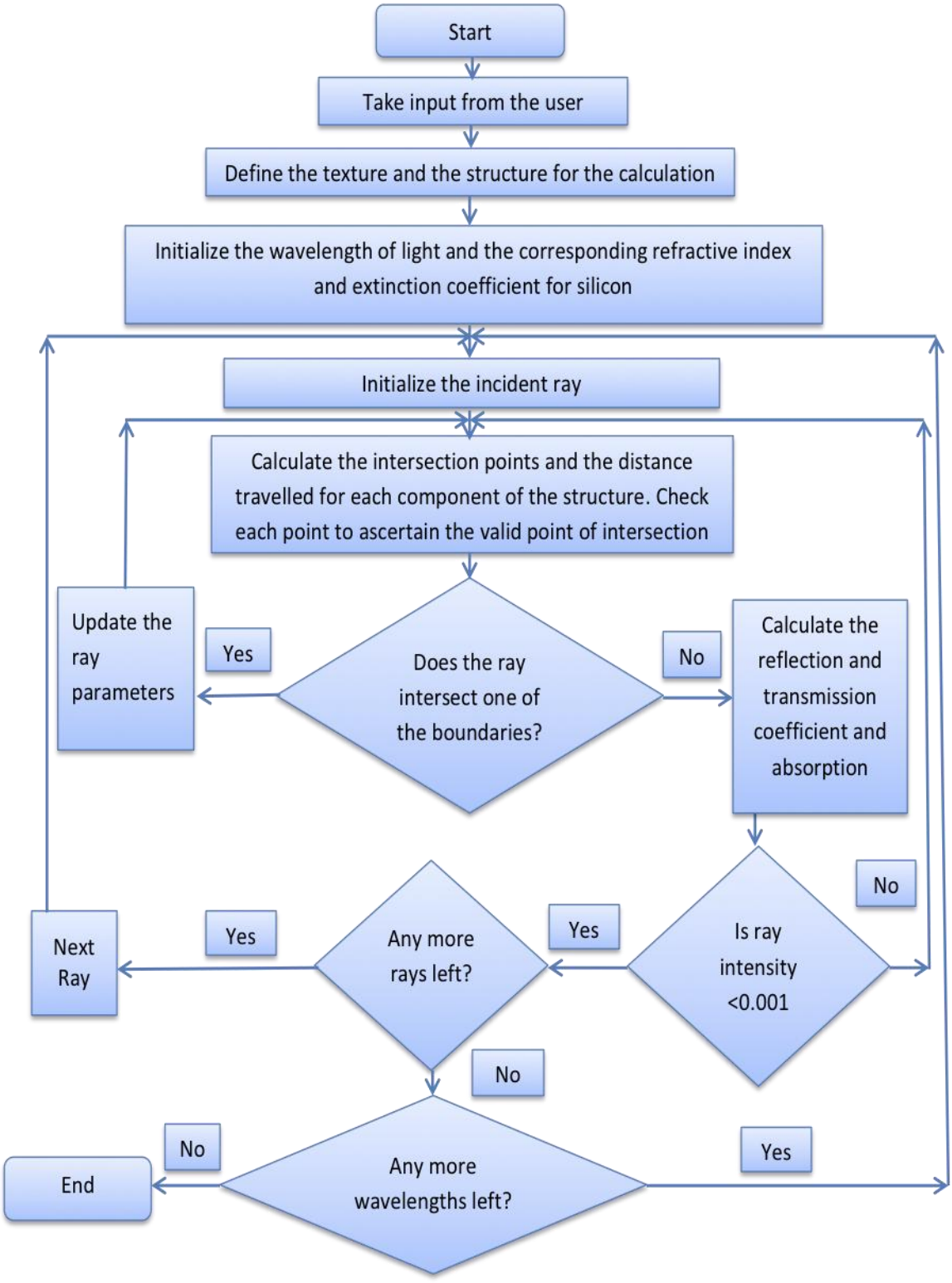

Figure 2.27 Flowchart for ray tracing computation

CHAPTER 3

DETAILED OPTICAL MODEL AND PROGRAM ALGORITHM

3.1 Introduction

There exist a quite a few ray-tracing programs and models that are capable of handling complex surfaces and multiple device layers. Some of them, like *PV Optics*, are excellent in giving meaningful and valuable information about light trapping features for real world solar cell and module designs. However, they do not have any provisions to add front metal architectures into the cell structure. This serves as a major limitation for solar cell and module designers to optimize front metal electrode structures and geometries. The main reason for this shortcoming is the fact that no model has been developed yet to simulate the interaction of light with a complete solar cell device structure including the front metal electrodes.

Introduction of front metal electrodes to the standard device structures renders the simple periodic boundary conditions used in models implemented in various solar cell optical simulation software packages to be useless. Even the most complicated of models like the ones that generate random textures on the surface of a (100) textured silicon wafer in 3-dimensions (3D) deal with only the air and silicon interface at the front end. With the introduction of front metal electrodes, a new metal layer is superimposed on the front textured surface leading to spatial non-uniformities and discontinuities in the cell structure. This requires a new strategy to model the interaction between light and the complete device structure. But before beginning to examine the complete

model, it would be pertinent to briefly explain the reason to use ray tracing over other available numerical techniques.

Choosing the correct and appropriate numerical technique to solve a complex problem like this can be a real challenge in itself. Finite Difference Time Domain (FDTD) is one of the most widely used numerical techniques for optical wave propagation simulations in solar cells and other structures [166-170]. It has a very high rate of accuracy coupled with the ability to handle complex optical wave phenomena. But its main drawback is the very high computing budget required for calculations, which grows roughly as the fourth power of the grid resolution [171]. This makes it challenging for solving large area problems with a limited computing capacity, such as using a desktop or a laptop.

While developing the optical model for solar cells, explained in this dissertation, there were a few clear-cut goals and targets that had to be achieved. Two of the main objectives were: (a) that the model so developed should be highly accurate and stand up to experimental scrutiny, and (b) the software should require the minimum computing budget possible. Creating a harmony between these two seemingly disparate goals was really challenging indeed. The main reasons and motivation behind choosing ray tracing as the preferred path were the following:

- Since the dimensions involved in commercial wafer based silicon solar cells, like thickness, texture heights, front metal contact dimensions etc., are much larger than the wavelength of useful incident light from the sun, which renders ray tracing completely valid.

- Ray tracing has a unique property whereby aspects of explicit wave nature of light, like behavior in anti-reflection coatings etc., can be

readily included without increasing the required computing budget and making this process highly accurate as well [158].

- The computing budget required for this kind of an algorithm or program is smaller compared to other computing methods, as the mesh sizes are lot larger for ray tracing simulations. For example, for good accuracy, the mesh size for FDTD calculations has to be lesser than one-tenth the wavelength of the propagation optical wave (λ/10), also called the Courant Factor [166].

- No need for fast, fancy and expensive computers, thereby enlarging the user base.

This chapter will explain, in detail, the model developed to implement the introduction of front metal architecture in alkaline texture etched (100) single crystal silicon solar cells and the program algorithm implemented in C++. This will include strategies to use the inherent symmetry in surface texture and cell design to reduce the computing area of the cell as well as the computing time while maintaining high calculation accuracy.

3.2 Model for Optical Calculations in a Finished Solar Cell

At present, solar cell technology has matured to an extent where each commercial solar cell is typically made on 6 in. X 6 in. semiconductor substrates. Performing computation on such a large area in a full scale 3D model is both time consuming and redundant. A simpler 2D model has been developed which reduces the computational time by at least an order of magnitude without any loss in accuracy. Furthermore, the software developed has the capability to implement various structural parameters of the device for cell and module study and design.

The starting point for the development of this model is to come up with a way to reduce the 3D device structure to a 2D. This is of paramount importance for two reasons: (a) there is practically no loss in computational accuracy due to this transformation, and (b) the computation time and budget are reduced by at least one order of magnitude.

Once the complex 3D structure is transformed to a corresponding 2D structure, the incident photon flux needs to be defined in terms of ray optics. As discussed in Chapter 1 of this dissertation, the AM 1.5 spectrum is used as the standard for solar cell testing as well as modeling. We do the same in our calculations. The formulation for the photon flux in terms of ray optics has to deal with two issues: (a) the correlation between the intensity of a ray of light to the total area illuminated, and (b) the effect of the angle of incidence on the photon flux density reaching the surface of the solar cell. As will be explained in detail, later, ray optics reduces an optical wave propagation problem to a problem of sampling the surface and volume. This implies that the higher the density of rays incident on the device surface, the higher is the accuracy of the calculations.

The next step in the modeling process is to (a) identify the inherent symmetries in the device structure, and (b) understand the inherent differences arising out of the introduction of front metal contacts. These are important to reduce the computation time and, more importantly, to devise the final integration step for complete device volume over the full range of incident wavelengths of light. This integration step is of vital importance as it provides the final results for the calculations.

In order to exploit the symmetry due to texture and device structure in alkaline etched single crystalline solar cells, the complete device area is divided into three regions for computational purpose, depending on their proximity to the front *fingers* and *bus bars*. This calls for three separate computations, one for each of these regions. Finally, once all the above-mentioned processes and computations have been realized, the results are integrated for complete device volume over the full range of incident wavelengths of light, giving the results for the entire computation.

3.2.1 3D Structure Transformation to 2D

(100) oriented single crystalline substrates are textured by etching with alkaline etchants to reduce reflectance from their surface. The resulting surface is filled with four-sided pyramids with square bases. These pyramids are generally randomly ordered with each of their four faces at an angle of 54.74° to the horizontal. A regular array of these pyramids can also be formed with the use of proper masking on substrate surface.

For the purpose of the new model, a regular array of pyramids is assumed on the back as well as the front surface of a silicon wafer. It has been found to be a very good approximation to a randomly textured surface. Figure 3.1 (a) shows a 2X2 array of such pyramids from the top while Figure 3.2 (b) shows the array from the one side.

As can be seen in the Figure 3.1, one pair of opposite faces of the 3D texture in Figure 3.1(a) can be approximated with the 2D structure shown in Figure 3.1(b), with a few modifications. Figure 3.2 shows the 3D view of the front

and the back side of an alkaline etched (100) silicon substrate. The complete device structure for a standard commercial single crystalline solar cell also consists of a back metal electrode. Figure 3.3 shows the side view of such a device in 2D. The correlation between the 3D structure and the 2D structure in Figures 3.2 and 3.3 is self-evident.

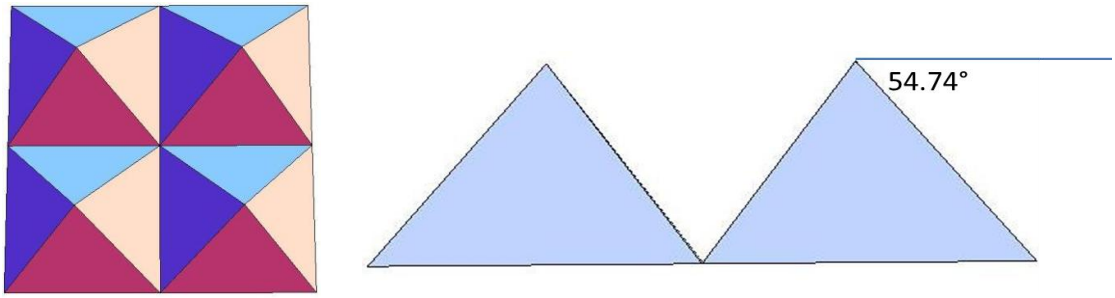

(a) (b)

Figure 3.1 (a) Top view of an array of 2X2 pyramids, (b) side view of the textures.

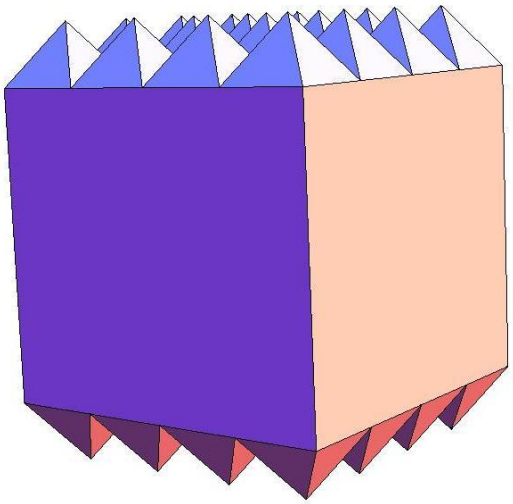

Figure 3.2 A 3D image of the front and backsides of an alkaline texture etched (100) silicon substrate.

As shown in Figure 3.3, the complete 2D structure is made up of *Unit Cells*. A unit cell is a single mesh created for the calculations. In other words, each of the square pyramids shown in Figure 3.1(a) makes up a *unit cell*, which encompasses the full thickness of the device, as shown in Figure 3.4. The dashed blue line in Figure 3.3 shows such a unit cell.

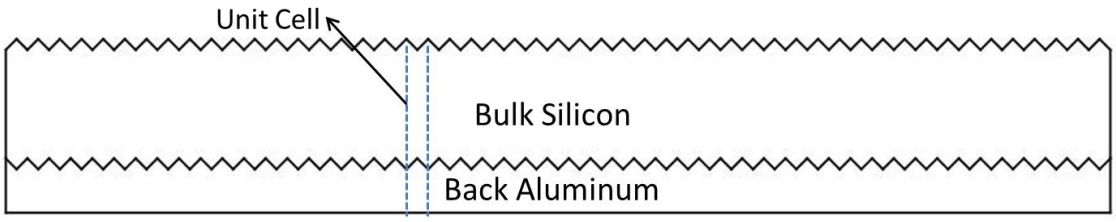

Figure 3.3 The standard structure 2D used for calculations without front metal.

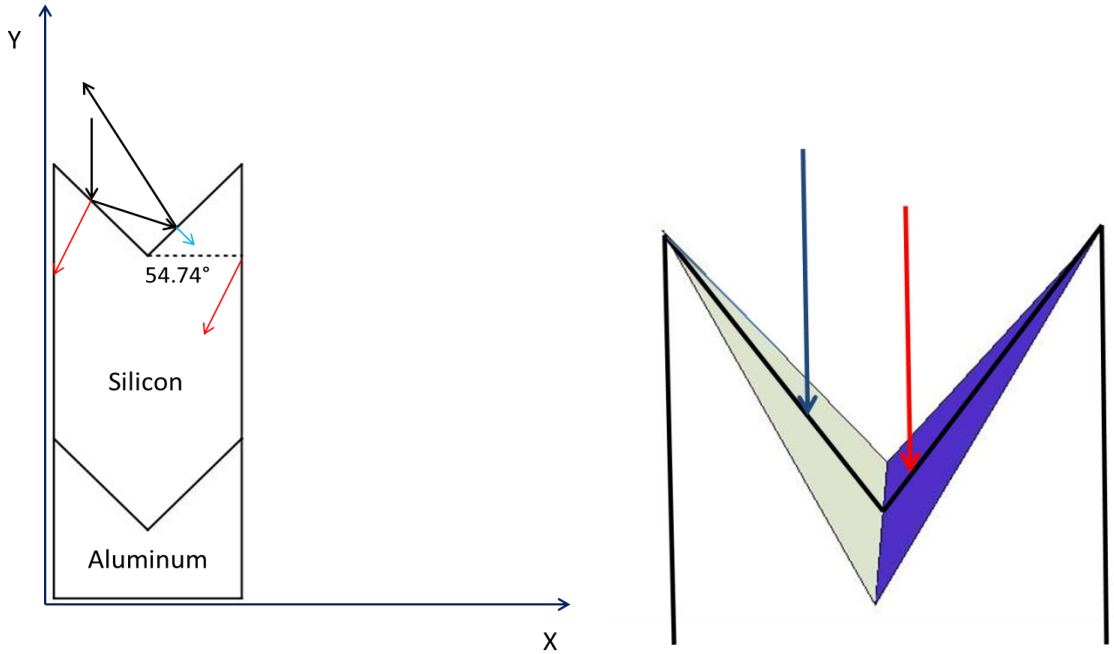

(a) (b)

Figure 3.4 (a) The standard structure used for calculations (marked in blue dashed lines in Figure 3.3), and (b) deduction of this structure from 3D.

Note that the Figure 3.4 is a magnified view of one of the V-shaped textures shown with dashed blue lines in Figure 3.3. This unit cell is the basis of the calculations performed for the complete finished solar cell. This is the same structure used in calculations for *PV Optics*.

The black rays shown in Figure 3.4 show the incident and reflected rays while the red and blue rays show the transmitted light in the device structure. Note that the texture angle equals that of a (100) textured surface shown in Figure 3.1(b).

Figure 3.4(b) shows exactly how two adjacent faces of the pyramidal surface constitute the corresponding 2D surface. The dark blue and the red arrows show incident light on each of these two faces. As can also be seen, this structure does not include the front metal fingers or busbars.

The side boundaries in this structure enforce the periodic boundary conditions for calculations. Whenever a ray of light hits any one of these boundaries, it is translated along the ‘X’ axis and brought into the cell structure from the boundary on the opposite side. The reflection coefficient at these boundaries is taken to be 0 while the transmission coefficient is taken to be 1, i.e., the intensity of the ray does not change upon striking any of the boundaries and then are brought back from the opposite side.

Whenever a ray of light is incident on any of these boundaries, it is translated along the ‘X’ axis and brought into the cell structure from the boundary on the opposite side. The reflection coefficient at these boundaries is taken to be 0 while the transmission coefficient is taken to be 1, i.e., the intensity of the ray

does not change upon striking any of the boundaries and is then brought back from the opposite side.

The structure shown consists of only the silicon absorber layer and the aluminum back contact. The black rays on the front surface denote the incident sunlight while the red and blue rays denote the light that is transmitted into the silicon substrate. The red rays explain the effect of the side boundaries. As can be seen from the figure, once the red ray hits the left side wall, it is brought back into the solar cell structure from the opposite side while keeping the Y coordinate the same.

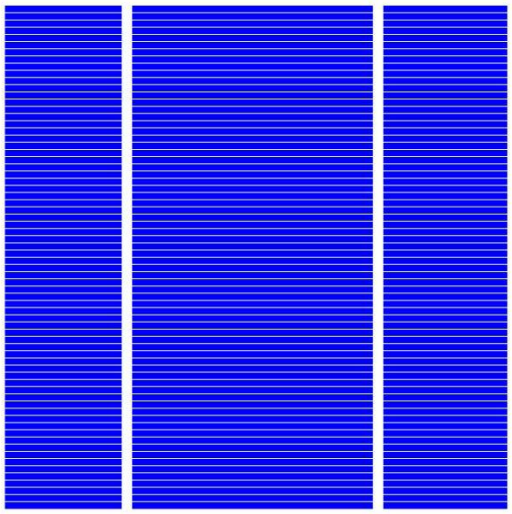

Figure 3.5 The front electrode architecture of a standard solar cell.

In order to include front metal contacts into this structure, it is necessary to observe the structure for a complete solar cell. Figure 3.5 shows the top view of a complete silicon solar cell. The thin white lines of the blue surface are called *Fingers* while the two thick white lines running perpendicular to the fingers are called *Bus bars*. They are made of silver and serve the purpose of extracting the charged carriers generated in the bulk of the alkaline textured semiconductor

substrate lying below and placing them in the external circuit. This bulk semiconductor region is shown in the same Figure in blue color. Figure 3.6 shows the 2D cross sectional view of the complete cell structure for fingers while Figure 3.7 shows the same view for busbars. All these structures are made using vectors. That is, each and every line segment in these structures is made using vectors. Figures 3.4, 3.6 and 3.7 show the three areas that a solar cell is divided into for the purpose of computations.

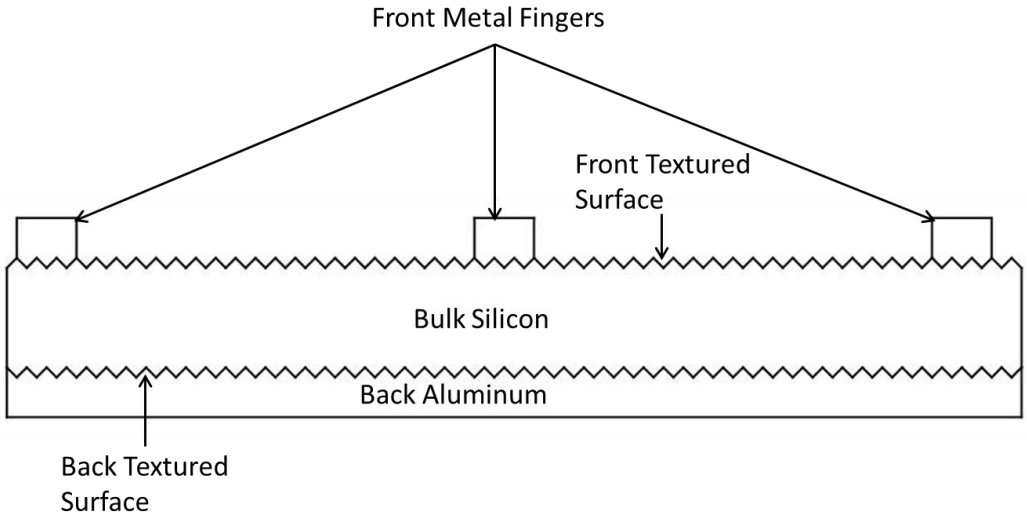

Figure 3.6 The 2D cross-sectional construction of fingers on textured silicon substrate.

In Figure 3.8, the 3D pyramidal structure is actually made up of two 2D structures shown in Figure 3.4. When light is incident on each of the unit textures, it is divided equally amongst each of the four faces. With the regular pyramidal structure assumed for this model, incident light travels either parallel or perpendicular to *X* and the *Y*-axes upon reflection as well as transmission into the device structure. This leads to the possibility of modeling each of the unit textures in 3D by two perpendicular structures shown in Figure 3.4. The rays

marked in black and blue in Figure 3.8 show each of these two perpendicular directions.

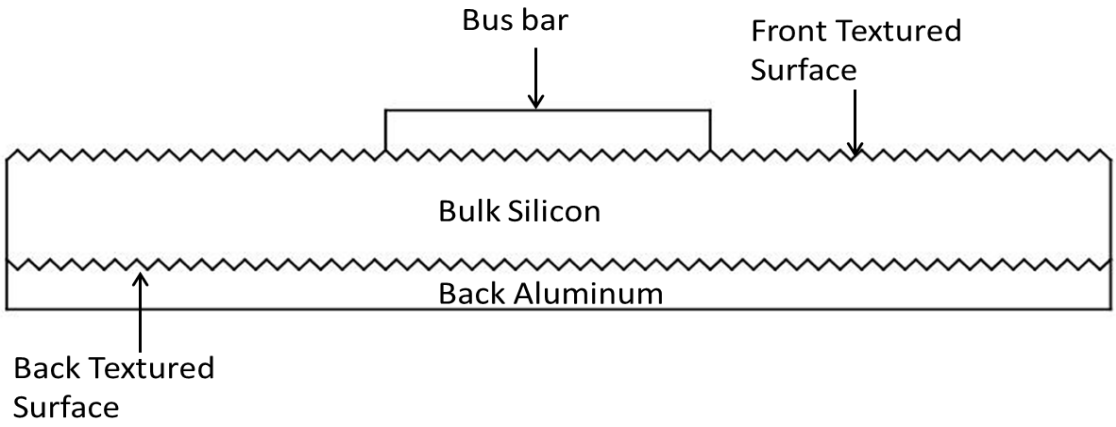

Figure 3.7 2D cross-sectional rendering of a busbar for the complete device structure.

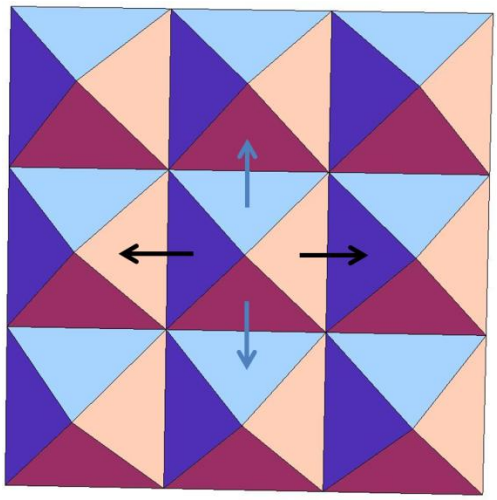

Figure 3.8 The pyramidal texture on (100) silicon surface. Note the pair of blue and black lines denoting the plane of propagation of reflected and transmitted light.

It is also assumed that the edges of each front metal contact starts and ends at the tip of a pyramid. The width and the number of fingers on the front surface vary from solar cell manufacturer to manufacturer. But, as a common rule

of thumb, the thinner and the lesser the number of fingers there are on a solar cell, the better its optical performance should be. This is because the area covered by the front metal electrode that shades the silicon substrate cannot see any sunlight directly. It only has to depend on the diffused transmitted light seeping into this region from the uncovered region.

It also has to be borne in mind that the bus bars and the fingers are lined up perpendicular to each other. This implies that the 2D textured surfaces shown below and on the sides of the fingers and the bus bar are perpendicular to each other as well.

3.2.2 Effect of Photon Flux Incident Angle

After the complete solar cell structure has been defined mathematically, the next step is to define the incident photon flux in terms of rays. The AM 1.5 spectrum, as explained in Chapter 1 of this dissertation, is taken to be the standard photon flux for the calculations. This is given in terms of *per* cm^2. The incoming photon flux is taken to be constant along the plane perpendicular to its direction of incidence. Hence, this has to be weighed according to the incident angles of the incoming rays. Figure 3.9 shows the relationship between the incident angle of the photon flux and the incident photon flux density along the X-axis.

In Figure 3.9, θ is the angle of incidence of the photons, and hence also the incoming rays. The intensity of the photon flux reaching the X-axis is given by the following dot product:

$$I_{Ph} = I_{AM\ 1.5}.\hat{Y} \tag{3.1}$$

where, I_{Ph} is the incident photon flux, $I_{AM\ 1.5}$ is the AM 1.5 photon flux and $\hat{Y}$ is the unit vector along Y- axis.

Eq. (3.1) translates to

$$I_{Ph} = I_{AM\ 1.5}\ \cos\theta_i \tag{3.2}$$

where, θ_i is the angle of incidence of the incoming rays.

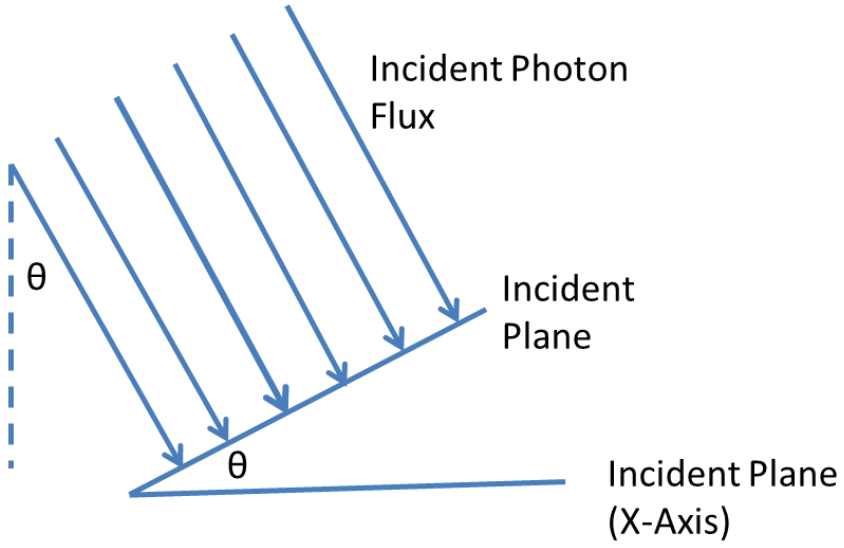

Figure 3.9 The incident photon flux at an angle with respect to the vertical (Y-axis).

The incident plane is divided up into a number of incident rays at equal distances from each other. Each ray has an intensity of 1.0. As the rays move about the computation structure, their intensity is reduced with each reflection and by absorption in the silicon layer. In the end, once the computation for a

region is completed, the results are averaged for the total number of incident rays.

3.2.3 Symmetry in a Solar Cell Structure and Computation Regions

As has been mentioned earlier, the computational area is divided up into three regions, depending on the proximity of each unit cell, under computation, to either the front metal fingers or busbars. This can be understood by examining the differences between calculations on a solar cell with and without the front electrodes. In the case of no front electrodes, the incident rays only interact with either of the two interfaces:

- Air and silicon, and
- Silicon and aluminum.

This is shown in Figure 3.10. The blue arrows denote the incident radiation from the sun while the red arrows denote the transmitted rays into the device structure. Note that the incident and transmitted light interacts with only the two kinds of interfaces as mentioned above.

In the case of a structure with front metal electrodes, this is not quite the case. The incident, reflected and the transmitted light can, in addition to the two interfaces stated above, interact with two other interfaces depending on the position and the direction of propagation: (a) air and silver, and (b) silicon and silver. Figure 3.11 shows the other possibilities.

The incident light is drawn in blue rays while the transmitted light rays are drawn in red and green. As can be seen, the red rays interact with the silicon and silver interface while the green rays behave same way as shown in Figure 3.10.

'*d*' is the distance from the edge of a metal contact to the region where the last transmitted ray interacts with silver-silicon interface. This difference in the two calculation scenarios gives rise to the extra two regions for a structure with metal contacts. The region shown in Figure 3.11 is one of those two regions. The structure is scanned with incoming light rays till it reaches the point at a distance '*d*' shown in the figure. The rest of the region perpendicular to the busbars behaves exactly the same way as the case without any front metal contacts.

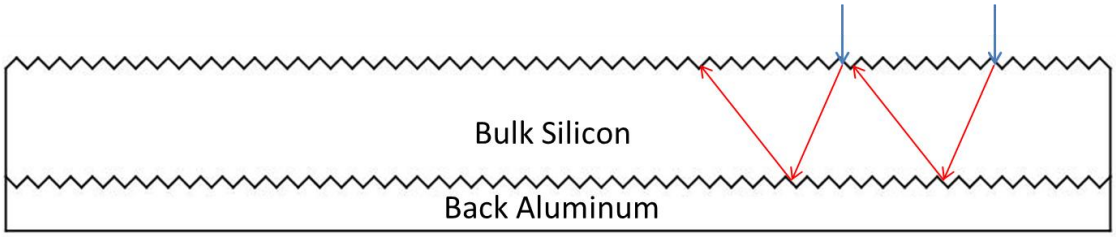

Figure 3.10 2D structure of the cross-section of a finished solar cell with no front metal. The blue arrows denote the incident rays while the red arrows denote the transmitted rays.

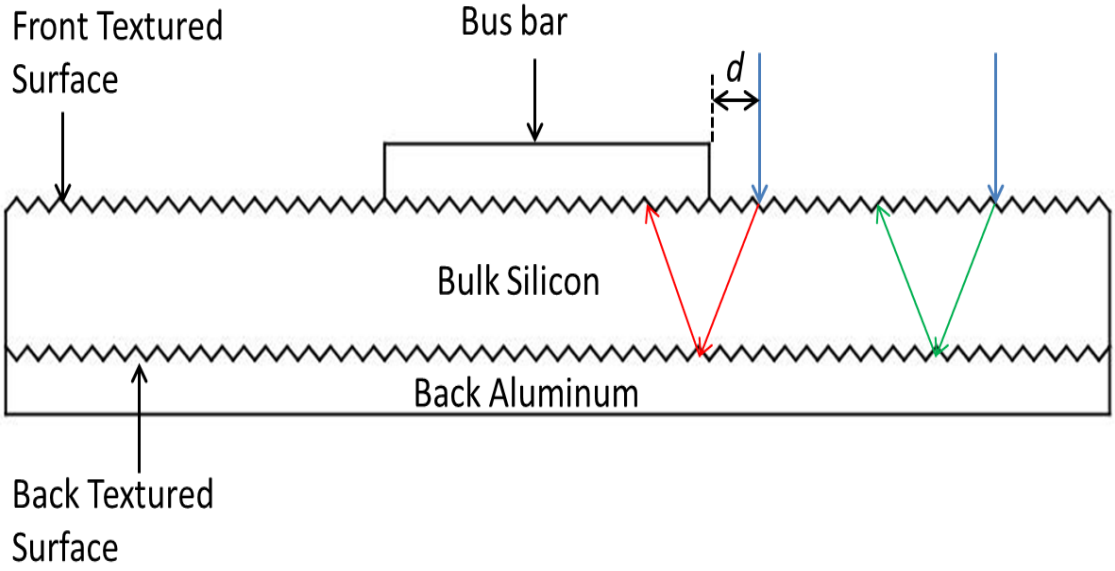

Figure 3.11 The progression of light rays in the case of a structure with front metal electrodes.

The same methodology is used for the area perpendicular to the fingers. Figure 3.12 shows this region in greater detail. It has been found through calculations that, in conventional commercial silicon solar cells, in the region perpendicular to the fingers, light always interacts with the silicon-silver interface. Hence, the scanning region encompasses the whole of the region in between two consecutive fingers.

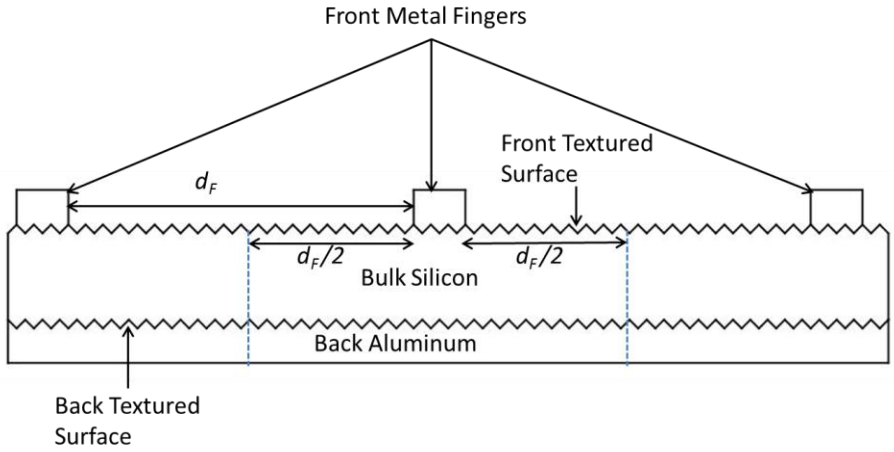

Figure 3.12 The region perpendicular to the metal fingers. 'd_F' is the region in between two metal fingers.

The distance between two fingers is taken to be d_F. By taking symmetry into account, the scanning or computational area in between fingers is taken to be $d_F/2$ on each side of a metal finger. This is the region marked in between the blue dashed lines in Figure 3.12. One such region is called a *Master Cell* which in turn is made up of many *unit cells*. The fingers at either end of the horizontal face of a solar cell are taken to be $d_F/2$ distance away from the edges. This means that once one such region is computed upon, the results can then be multiplied by the number of total fingers in the solar cell under computation. In summary, the three computation regions that a solar cell is broken down into are:

- *Region 1*- The region where there is no interaction of transmitted light with the silicon-silver interface (Figure 3.10)

- *Region 2*- The region near the busbars (perpendicular to the busbars) where the transmitted light interacts with the silicon-silver interface (Figure 3.11).

- *Region 3*- The region in between the fingers denoted by the blue dashed lines as shown in Figure 3.12.

3.2.4 Integration of Calculations over the Entire Solar Cell

Once the calculations over the three regions have been completed, the results have to be integrated over the entire volume of the solar cell to get the final output. As has been mentioned before, the entire solar cell is divided into a mesh for computational purposes. This process is known as *meshing* in numerical calculations. Figure 3.13 shows the meshing pattern for a finished solar cell. Note the array of 4X4 pyramids shown in the mesh for reference. Each unit pyramid shown in Figure 3.1(a) constitutes one unit mesh, with the depth being the entire thickness of the device.

All the structures and regions shown till now lie in this mesh. The integration of the calculated regions is done for each of this mesh at the end. The light incident on each of these meshes is divided into two equal parts: one travelling in the direction of the blue rays, while the other half travelling in the direction of the red rays. Each of these directions is portrayed by any of the three regions explained above, depending on the placement of the unit mesh.

The total current generated in the complete volume of the solar cells is given by:

$$I_{SC} = I_{Region\,1}N_{Region\,1} + I_{Region\,2}N_{Region\,2} + I_{Region\,3}N_{Region\,3} \tag{3.3}$$

where, I_{SC} is the current generated over the entire solar cell, $I_{Region1}$ to $I_{Region3}$ are the currents generated in each unit mesh from region 1-region 3 while $N_{Region1}$ to $N_{Region3}$ are the number of unit meshes in each of the three regions, respectively. The back metal losses and the front metal losses are also calculated in the same way as Eq. (3.3).

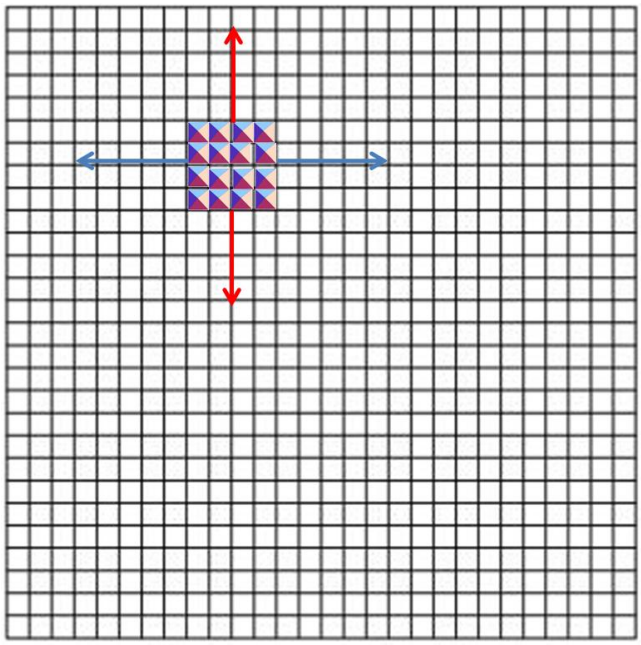

Figure 3.13 The top view of the meshing of a solar cell with a few pyramids shown for reference.

3.3 Conclusions

This chapter explains the full model, procedure and algorithm followed for calculations in a finished solar cell upon the inclusion of front metal electrodes. The complete 3D structure of the solar cell device is reduced to three subsequent 2D structures for computation. The entire volume of the solar cell is divided into three separate 2D regions for the purpose of computation. The computation for each region is done in series with the computation time reduced by at least an

order of magnitude as compared to full 3D computations. The results from each of these regions are then integrated over the entire volume of the given solar cell and over the entire range of useful wavelengths of incident sunlight. Refractive indices and extinction coefficients for silicon, aluminum and silver are taken from the existing database of PV Optics. The main values of interest from these calculations are follows:

- the total maximum current that can be generated from an entire finished solar cell assuming that each absorbed photon results in the generation of one electron-hole pair in the silicon bulk;
- the maximum current that can be generated in the shaded region of the solar cell due to the diffusion of light;
- the back and front metal optical losses over the entire solar cell;
- the absorption profile beneath the shaded region, i.e., below the fingers and the busbars.

CHAPTER 4

SUMMARY OF RESULTS: SOLAR CELL

4.1 Introduction

The standard structure of a commercial solar cell, as explained in Chapter 3 and Chapter 4 of this dissertation, consists of the following:

- a semiconductor absorber layer with textured front and back surfaces to reduce reflectance and hence increase absorbance,
- a p-n junction formed in the semiconductor absorber layer to aid in separation of the optically generated carriers,
- a back metal contact to extract the optically generated charge carriers in the bulk of the absorber semiconductor layer.
- a thin layer of anti-reflection coating on the front surface of the semiconductor absorber layer to further increase light trapping,
- a front metal electrode grid pattern to complete the electrical circuit for carrier extraction from the absorber semiconductor layer.

As explained in Chapter 3 of this dissertation, the new model incorporating all of the above structure components in solar cells has been implemented in a computer program written in C++. This version of the software, *PV Optics 4.0*, will soon be released for common usage. The user using this program will have the freedom and option to vary various material as well as structural parameters of a solar cell. The structural parameters that can be varied by the user include the following:

- the thickness of the silicon absorber layer,
- texture angle and texture height with the option of having planar of textured back and front surfaces of the silicon absorber layer,

- two layer anti-reflection coating at the front surface,
- thickness and material of the back metal contact,
- front metal electrode architecture:
    i. width and height of a metal finger,
    ii. spacing between metal fingers,
    iii. thickness and height of the busbars,
    iv. location of the busbars on the front silicon absorber layer surface.
- thickness and optical parameters of the solar cell encapsulant,
- thickness and optical parameters of the glass enclosure.

These options provide the new software with flexibility and capability in terms of choosing the solar cell structure. Calculations have been performed on many solar cell structures using the new software. The main aim of these calculations is to provide a trend in the optical performance of single crystal texture etched solar cells made on (100) oriented silicon substrates while varying various structural parameters. Table 4.1 specifies the structural parameters that have been maintained constant for this study. This chapter provides the simulation results for a stand-alone un-encapsulated solar cell while the next chapter will summarize the effects of encapsulation of such a solar cell in a module. All the calculations have been done for normally incident light on the cell surface. This is the standard practice to optimize solar cell performance under the effect of normally incident light. The optical parameters have been taken from the existing database in the previous versions of PV Optics.

Table 4.1 The various structural parameters of a solar cell that have been maintained constant for calculations

Structure Parameters	Inputs Used in Calculations
Anti-reflection coating	**Two layers: (a) Native Silicon dioxide (b) Silicon Nitride**
Texture Angle	**70.52° -For (100) texture etched silicon**
Absorber Layer Material	**Silicon**
Back Metal Contact Material	**Aluminum**
Back Metal Contact Thickness	**2 μm**
Front Metal Contact Height	**20 μm**
Front Metal Contact Material	**Silver**

As can be seen from the above table, the front metal contact height and the back metal contact thickness are not varied for these calculations. In the case of back metal contact thickness, because it is known that metals are highly absorbing in nature, the variation in thickness of aluminum used in commercial solar cells does not make any difference as all the light that is transmitted into the metal is absorbed completely very close to the surface. For the case of front metal contact height, any normally incident light would be reflected away from the solar cell surface upon reflection from the sidewalls of front metal fingers. Figure 4.1 elucidates this more clearly. The rays signify the direction of the travelling light. The case of encapsulation of a solar cell in a module and the effect of front metal electrode height has been investigated in the next chapter.

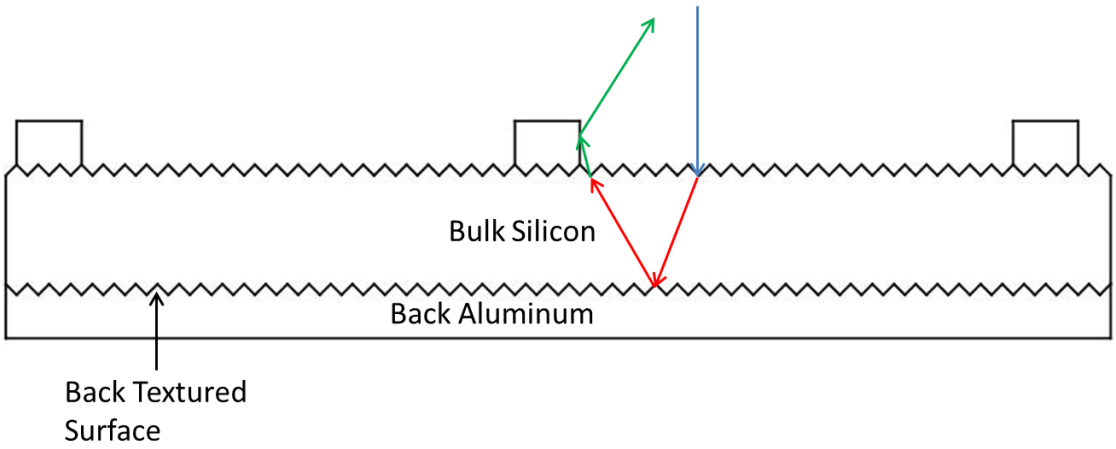

Figure 4.1 The interaction of normally incident light with front metal.

4.2 Simulation Results

The effects of variation in the following structural parameters are investigated:

- silicon absorber layer thickness,
- finger thickness and spacing, and
- texture height.

4.2.1 Variation in Silicon Absorber Layer Thickness

Silicon, being an indirect band-gap semiconductor, has a low absorption coefficient. This effect is especially pronounced as the wavelength of light approaches the band-edge of silicon. Texture etching of silicon, using anisotropic alkaline etches, is an effective method to increase absorption over the entire useful solar spectrum. Hence, this has become a standard processing technique for single crystal (100) oriented silicon solar cells. Thus, it also makes sense that the more the thickness of the silicon absorber layer, the higher the optical absorption, leading to more current being generated from the photovoltaic device.

For the calculations, the thickness of the absorber layer has been varied from 40 µm to 180 µm in five steps- 40 µm, 80 µm, 120 µm, 150 µm and180 µm. Table 4.2 summarizes the various parameters that are kept constant for these calculations and their corresponding values. These are not mentioned in Table 4.1.

Table 4.2 Parameters kept constant to study the effect of thickness on the performance of a solar cell

Parameters Kept Constant	Parameter Values
Texture Height	2 µm
Finger Width	100 µm
Busbar Width	2 mm
Number of Fingers	70
Number of Busbars	2
Solar Cell Dimensions	156 mm X 156 mm

For normal incidence, light is only shown on the exposed region of the solar cell. Table 4.3 summarizes the results of these calculations. The Maximum Achievable Output Current (MAOC) has the unit of Amperes (A) while the other losses are given in terms of milli-Amperes (mA). MAOC is calculated assuming that every photon generates one electron-hole pair and both these carriers have a probability of 1.0 to be extracted from the solar cell bulk through the front and back metal electrodes. Figure 4.2 shows the graphical plot of the calculated MAOC results with respect to the absorber layer thickness. Figure 4.3 plots the reflectance loss and the back metal absorption loss while Figure 4.4 plots the

percentage current generated in the shaded region of the solar cell with respect to the absorber layer thickness. The reflectance loss shown in Table 4.3 is calculated in terms of the number of photons reflected back from the solar cell surface assuming that each photon, if absorbed, would have contributed one electron-hole pair to the MAOC.

Table 4.3 Summary of calculated results for different absorber layer thicknesses and metal finger width of 100 µm

Absorber Layer Thickness (µm)	Maximum Achievable Output Current (A)	Reflectance Loss (mA)	Back Metal Absorption Loss (mA)	Front Metal Absorption Loss (mA)	% age current generated in the shaded region
40	8.46	932.56	674.09	1.02	0.175
80	8.73	771.11	571.56	1.15	0.24
120	8.83	769.94	474.84	1.21	0.30
150	8.94	689.26	445.61	1.14	0.325
180	9.04	614.77	421.69	1.11	0.34

Figures 4.2 and 4.3 provide insight into the effect of the absorber layer thickness on the optics of a solar cell. The plot in Figure 4.2 and the Table 4.3 show that there is a constant increase in the MAOC as the thickness of the silicon absorber layer increases. It is also important to note that the increase in current from 40 µm to 180 µm, an increase of 350%, results in the increase in the MAOC by only 6.855%. This indicates that, with better wafer handling and light

trapping techniques, solar cells with thin absorber layers can perform as well as the current solar cells with a thick silicon absorber layer.

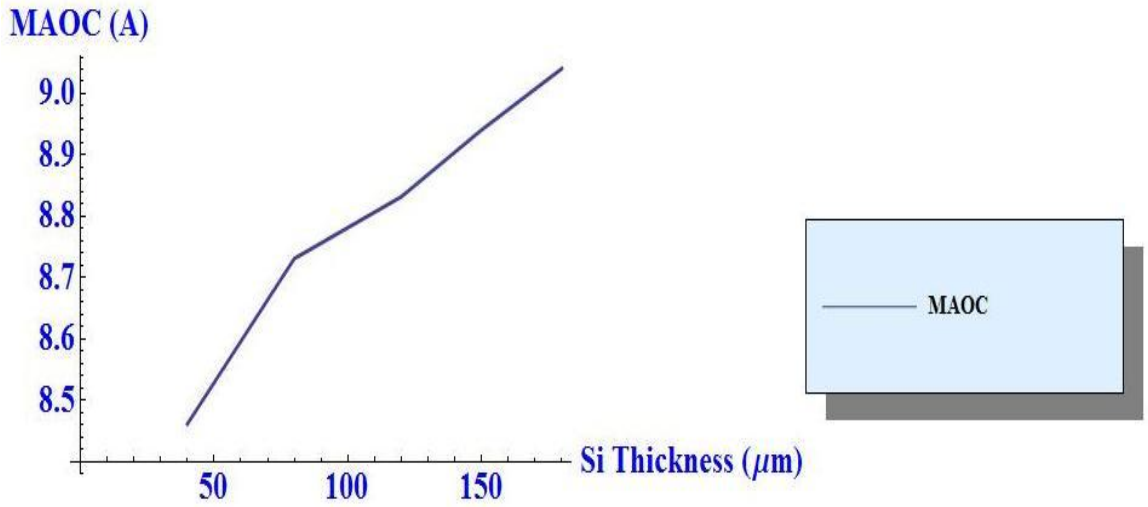

Figure 4.2 Plot of MAOC with respect to silicon thickness.

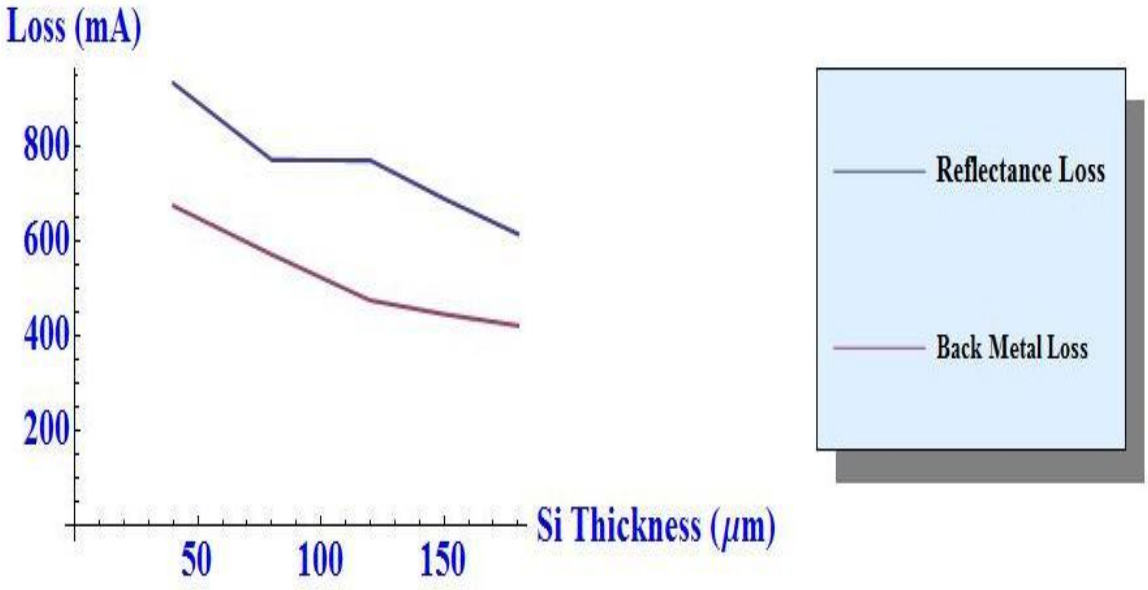

Figure 4.3 Plots of Reflectance Loss and Back Metal Loss with respect to silicon thickness.

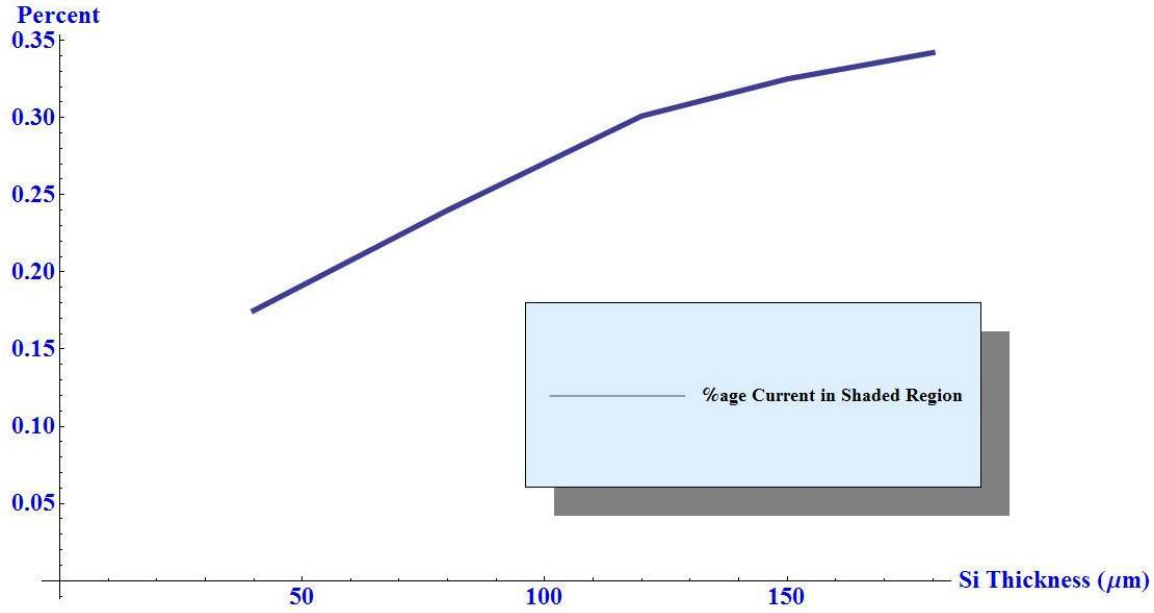

Figure 4.4 Plot of percentage current generated in the shaded region.

Another important set of numbers to be taken into account while designing a solar cell are the various losses accrued during its functioning. Some of the various optical losses have been summarized in Table 4.3. These losses are:

Reflectance Loss: This is caused by the reflection of light from the solar cell and air interface. The plot in Figure 4.3 shows the change in the amount of loss due to reflectance with respect to the change in thickness of the silicon absorber layer. Note that there is a constant decline in the reflectance loss from a solar cell with an increase in the silicon thickness. This should imply that the reduction in reflectance should yield a subsequent gain in the generated current. But on closer examination, it becomes clear that the savings from the reflectance loss add up to an increment in the current generated in the solar cell. This is due to fact that, as the wavelength of light approaches the band edge of silicon, the absorption coefficient decreases exponentially. Hence, the light that is

transmitted into the absorber layer at these wavelengths is not highly absorbed which leads to the light travelling great lengths within the silicon substrate. Due to the texturing of the silicon surfaces and the application of an anti-reflection coating at the front end of the solar cell, the optical path-lengths within the silicon absorber layer at these wavelengths is highly enhanced, leading to higher absorption and hence an increase in the total current generated. As has been stated earlier, better light trapping techniques would mean that this loss can be reduced substantially for thinner silicon substrates than what is achieved commercially at present. This light, upon travelling the entire thickness of the silicon substrate, strikes the silicon-aluminum or the silicon-silver interfaces and is absorbed by the metal at the contacts leading to what is called the *Metal Loss*. Table 4.3 mentions two of these metal losses: back metal loss and the front metal loss.

Back Metal Loss: This is the optical loss that occurs due to the parasitic absorption of light by the metal at the back contact interface without actually resulting in the generation of any electron-hole pairs. Figure 4.3 shows that the amount of light lost due to this loss decreases as the thickness of the silicon layer is increased. This is due to the increase in the optical path-length of light. Any savings in this loss leads to an increase in the current generated by the solar cell. Note that the amount of the back contact loss is at least two orders of magnitude greater than the front metal loss. This is due to two reasons:

- The entire backside of the silicon substrate is covered by metal while only a fraction of the front side of the silicon is covered with metal.

- It is clearly visible from Figure 4.1 that the light travels half the distance in silicon to reach the back metal compared to the front metal. Hence, by the time the light reaches the front metal interface, its intensity is highly reduced.

Front Metal Loss: Front metal loss is caused by light travelling the entire thickness of the silicon twice and then getting absorbed by the front silver contacts. As can be seen from Figure 4.3, this loss is negligible compared to the other losses and any reduction in this will have no perceptible improvement in the performance of a solar cell.

The one loss that has not been stated in Table 4.3 is the *Shading Loss*. This is the optical loss that takes place in a solar cell due to the shading of the semiconductor absorber layer due to the front metal contacts. As the front metal hinders the direct interaction of photons with the absorber layer in the shaded regions, only the uncovered part of the silicon can be considered to be optically active. This is clearly visible in Table 4.3 and the plot in Figure 4.4, where, for a 40 µm thick silicon solar cell, only about 0.175% of the total current generated is due to the optical absorption in the shaded region. But it is also visible that as the thickness of the silicon absorber layer is increased, the percentage of the total current generated in the shaded region keeps on increasing. This is because of the following two reasons:

- light travels a greater distance within the silicon layer before reaching the back metal or the front interfaces, and
- the subsequent reduction in the metal losses.

Figures 4.5 and 4.6 show the pattern of absorption of light in the shaded region of (a) fingers, and (b) busbars for a silicon solar cell with an absorber layer

thickness of 40 µm. In these plots, the absorption is in terms of milli-Amperes in the Y-axis and the distance below a metal finger or the bus bar in the shaded region in X-axis. The distance in the shaded region is in terms of unit cells explained in Chapter 3 of this dissertation. The absorption under the busbars in the silicon, back metal and front metal are plotted in the logarithmic scale on the Y-axis while the absorption under the fingers for the same are plotted in the normal scale. It would be further beneficial to recall that the width of each metal finger is approximately 100 µm while the width of each busbar is about 2 mm.

As can be seen in Figure 4.5, there is a gradual decrease in the absorption and the loss values from the edges towards the center. This is due to comparatively thick nature of the busbars due to which light entering from one end of the shaded region does not get out from the other side. The absorption under the fingers does not follow such a simple pattern. This is due to the relatively thin nature of the fingers, where light can travel from one end and escape from the other side resulting in interesting absorption patterns.

4.2.2 Variation in Metal Finger Width

Front metal electrode architecture is not only important for optical performance of a solar cell but also for its electrical performance. It is known that, as the thickness of a metal contact is increased, its current carrying capacity increases while its resistance decreases. Increasing the thickness of the metal fingers has some major disadvantages though. Thicker fingers would mean a larger shaded area in a solar cell, which in turn would have an adverse effect on its efficiency.

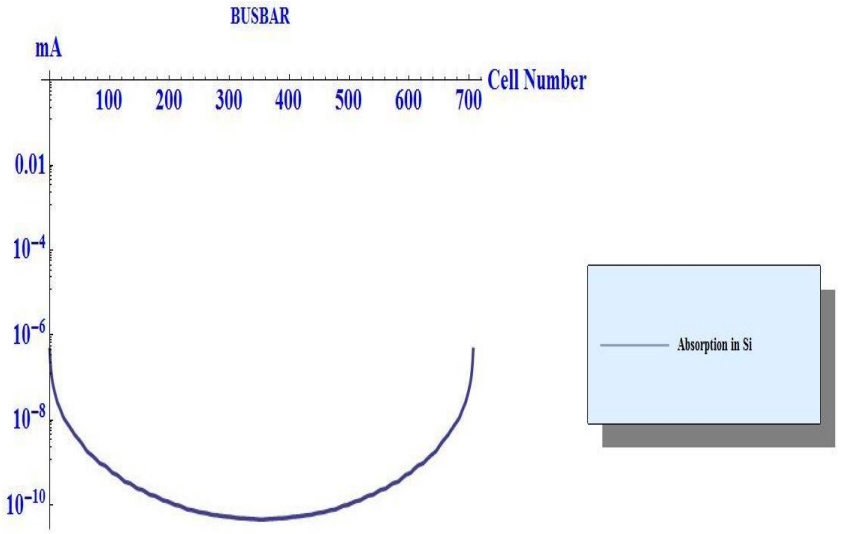

(a)

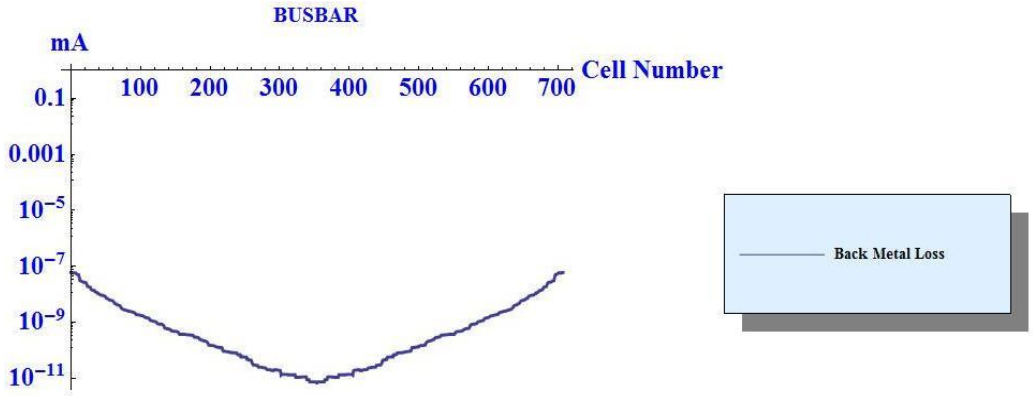

(b)

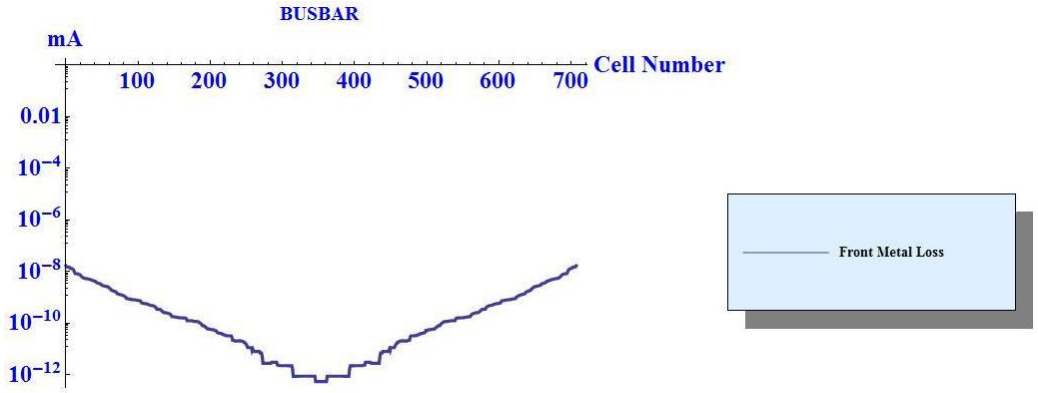

(c)

Figure 4.5 Optical absorption under the busbar in (a) Silicon, (b) Back Metal, and (c) Front Metal for silicon thickness of 40 μm plotted in log scale.

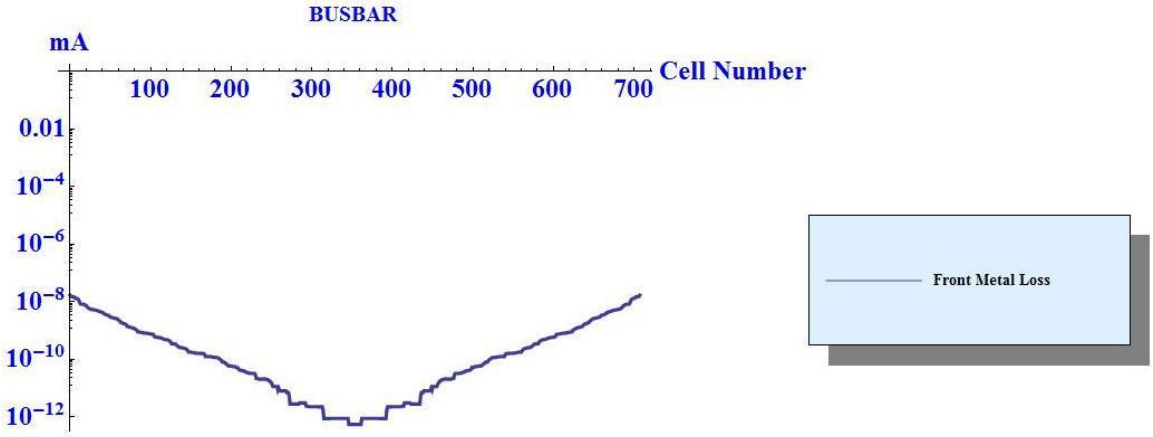

(a)

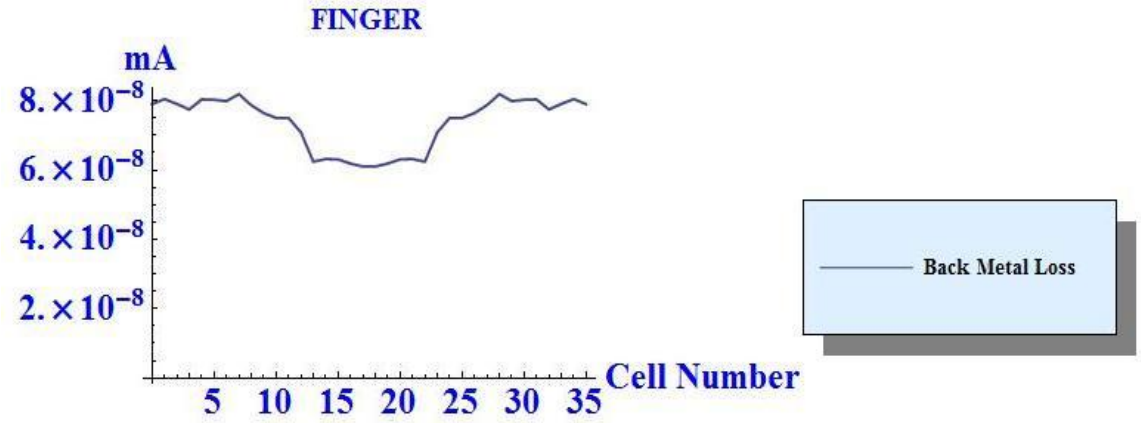

(b)

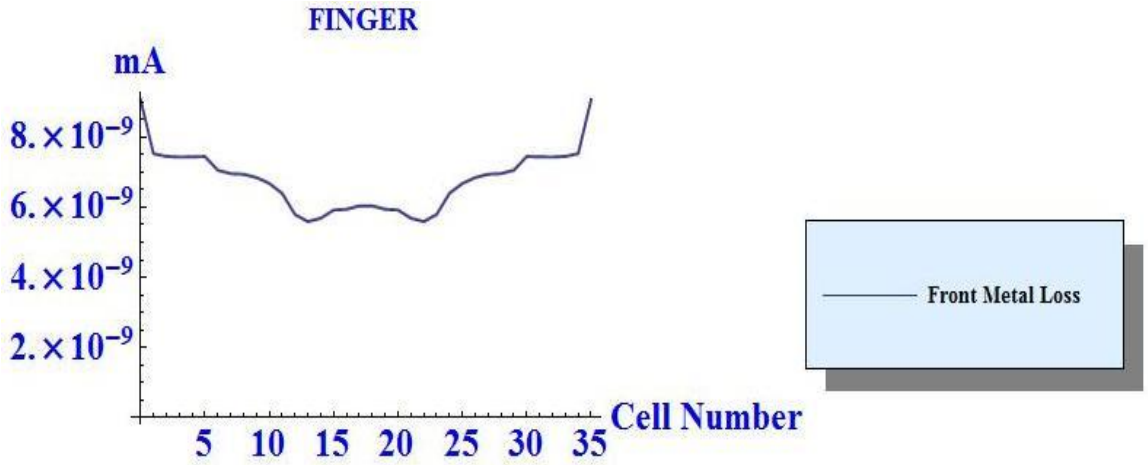

(c)

Figure 4.6 Optical absorption under a metal finger in (a) Silicon, (b) Back Metal, and (c) Front Metal for silicon thickness of 40 µm.

On the other hand, increasing the thickness of fingers and decreasing their total number would mean that the fingers would be farther apart from each other. This would result in the carriers having to travel farther to be captured by the front electrode grid, thereby increasing the probability of them recombining in the silicon bulk or the surface. Hence, the metal finger width and the spacing between them are of vital importance to the performance of a solar cell.

In this section, optical simulation results for three different metal finger widths and the corresponding spacing between them are provided. Calculations have been done for four thickness values for each case in order to see the effect of silicon absorber layer thickness variations along with the variation in metal contact thickness. While varying the finger thickness, it is made sure that the total shaded region in the solar cell remains the same as in the case presented in the previous section. The finger thickness values used for calculations are (a) 75 µm, (b) 50 µm, and (c) 25 µm. This is in addition to the calculations with 100 µm metal finger thickness presented in the earlier section. The four silicon absorber layer thickness, used here, are (a) 40 µm, (b) 80 µm, (c) 120 µm, and (d) 180 µm.

Table 4.4 presents the results for metal fingers of thickness 75 µm for the above mentioned silicon absorber layer thicknesses. Table 4.5 shows the same results for metal finger thickness of 50 µm while Table 4.6 shows the calculated results for metal thickness of 25 µm. Figure 4.7 presents the plots of the MAOC values for all the calculated metal finger widths. Figure 4.8 presents the plots for back metal absorption loss and Figure 4.9 shows the reflectance losses for all

the silicon absorber layer thickness and metal finger width values for comparison. The plot in Figure 4.10 shows the change in the percentage of current generated under the shaded area for all the thicknesses and widths.

Table 4.4 Summary of calculated results for different absorber layer thicknesses and metal finger width of 75 µm

Absorber Layer Thickness (µm)	Maximum Achievable Output Current (A)	Reflectance Loss (mA)	Back Metal Absorption Loss (mA)	Front Metal Absorption Loss (mA)	% current generated in the shaded region
40	8.44	928.45	672.46	1.15	0.22
80	8.69	768.16	569.88	1.25	0.3
120	8.82	767.05	473.48	1.25	0.36
180	9.01	612.33	420.5	1.14	0.4

Table 4.4 shows the same trend in all the calculated values for the ones shown in Table 4.3. The MAOC and the loss values are almost the same as previously stated as well. The only real difference is in the case of percentage current generated in the shaded region of the solar cell. This is because, as the thickness of the metal fingers are decreased while keeping the total shaded area constant, the distance between consecutive fingers decreases which leads to the portion of AM 1.5 spectrum with low absorption in silicon to travel further into the shaded regions as compared to the previous case.

Table 4.5 Summary of calculated results for different absorber layer thicknesses and metal finger width of 50 µm

Absorber Layer Thickness (µm)	Maximum Achievable Output Current (A)	Reflectance Loss (mA)	Back Metal Absorption Loss (mA)	Front Metal Absorption Loss (mA)	% current generated in the shaded region
40	8.46	929.99	675.46	1.33	0.305
80	8.73	770.05	571.94	1.33	0.38
120	8.83	768.77	475.28	1.29	0.43
180	9.04	614.26	421.87	1.15	0.47

Table 4.6 Summary of calculated results for different absorber layer thicknesses and metal finger width of 25 µm

Absorber Layer Thickness (µm)	Maximum Achievable Output Current (A)	Reflectance Loss (mA)	Back Metal Absorption Loss (mA)	Front Metal Absorption Loss (mA)	% current generated in the shaded region
40	8.46	927.72	676.62	1.57	0.48
80	8.73	769.14	572.29	1.31	0.57
120	8.83	768.68	475.27	1.41	0.62
180	9.04	614.17	421.87	1.17	0.64

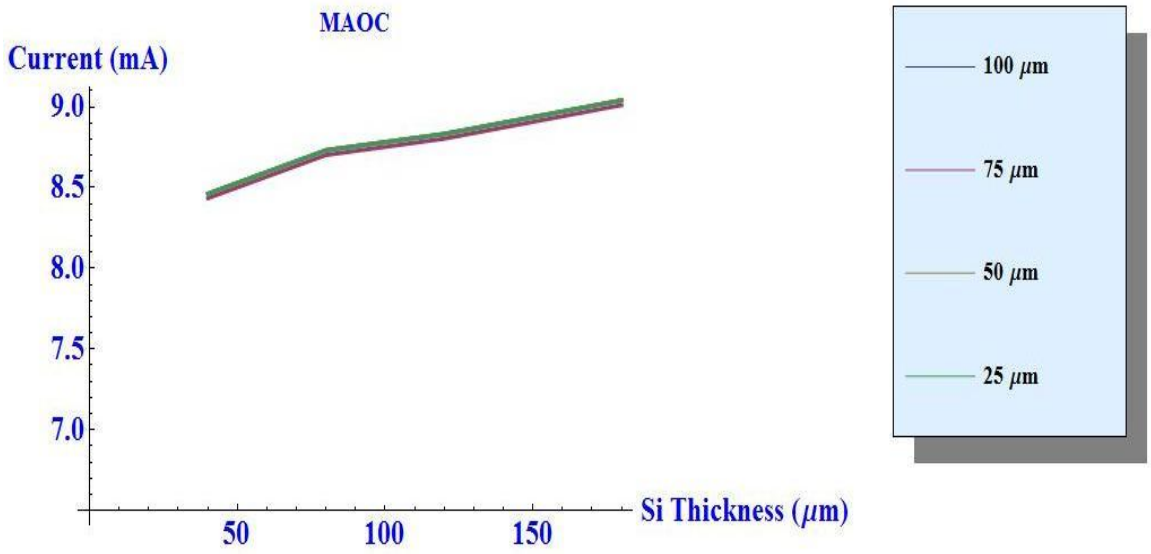

Figure 4.7 Plot of MAOC values with respect to silicon thickness for metal finger width of (a) 100 µm, (b) 75 µm, (c) 50 µm, and (d) 25 µm.

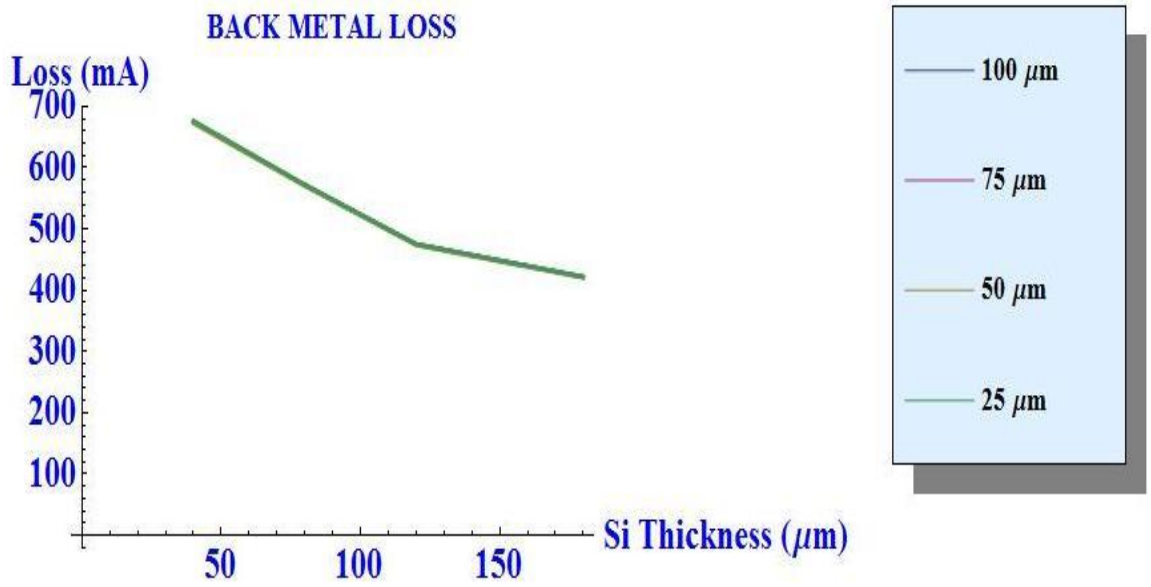

Figure 4.8 Plot of back metal loss with respect to silicon thickness for metal finger width of (a) 100 µm, (b) 75 µm, (c) 50 µm, and (d) 25 µm.

As can be clearly seen in Figure 4.7, the variation in the width of the metal fingers has minimal effect on the MAOC values for all the silicon absorber layer thicknesses. This is to be expected, as the total shaded region on the solar cell is

kept constant in all the cases. The minute differences are because of the difference in the mesh sizes for various metal contact widths.

Figure 4.9 Plot of reflectance loss with respect to silicon thickness for metal finger width of (a) 100 µm, (b) 75 µm, (c) 50 µm, and (d) 25 µm.

As for MAOC values, it is quite clear from the plots in Figure 4.8 and 4.9 that the change in the width of metal fingers has no effect on the losses either due to reflectance or due to back metal absorbance. Hence, when it comes to designing front electrode architectures, optical effects have minimal effect on the output current of a solar cell.

The plots in Figure 4.10 show the current generated in the shaded region of a solar cell with varying front metal contact width. As is clearly visible, the most current generated in the shaded region is in the case of metal fingers of width 25 µm, which decreases as the front metal width increases.

The calculated results presented in this section can be summarized as follows:

- Variation in front metal electrode width has negligible effect on the total MAOC derived from a solar cell of any silicon absorber layer thickness.
- There is negligible influence of the front metal electrode width on the reflectance, back metal, and front metal absorbance losses.
- There is a perceptible difference in the amount of current generated in the shaded region of a solar with varying front electrode width. This current increases as the metal electrode width is reduced while keeping the total shaded region constant.

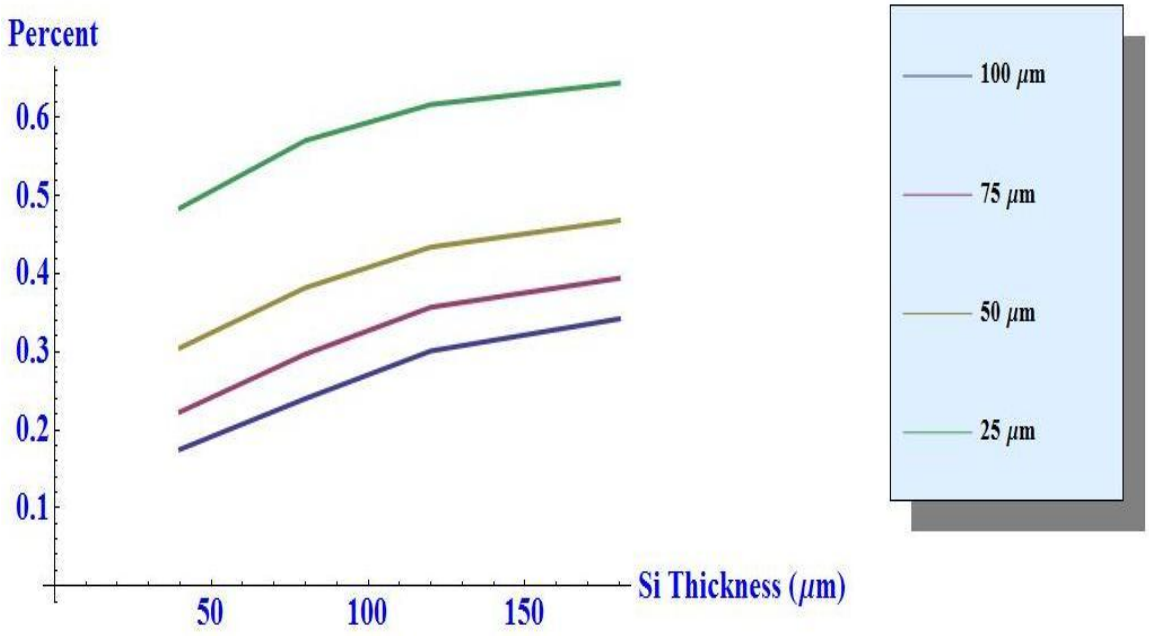

Figure 4.10 Plot of percentage current generated in the shaded region for various silicon absorber layer thickness and front metal contact width.

4.2.3 Effect of Texture Height

The anisotropic alkaline etching process, in practice, produces a textured surface with varied texture height. Hence, it would be worthwhile to study the effect of the texture height on the total MAOC generated in the solar cell and the percentage

of current generated in the shaded region. Figure 4.11 shows the 2D structure of a textured solar cell discussed earlier in Chapter 3. The texture height is marked in the figure for reference. Note that the increase in the texture height in the cell structure has a direct effect of increasing the unit mesh size for calculations. Everything else in the structure remains absolutely the same for any texture height. The calculations in this section are done by taking the finger width to be 100 µm, the busbar width to be 2 mm and the texture height is taken to be 3 µm. All the other variables are kept absolutely the same as in the previous batch of calculations. Table 4.7 compares the total MAOC values and the percentage current generated in a solar cell with the similar structure except for a different texture height of 2 µm.

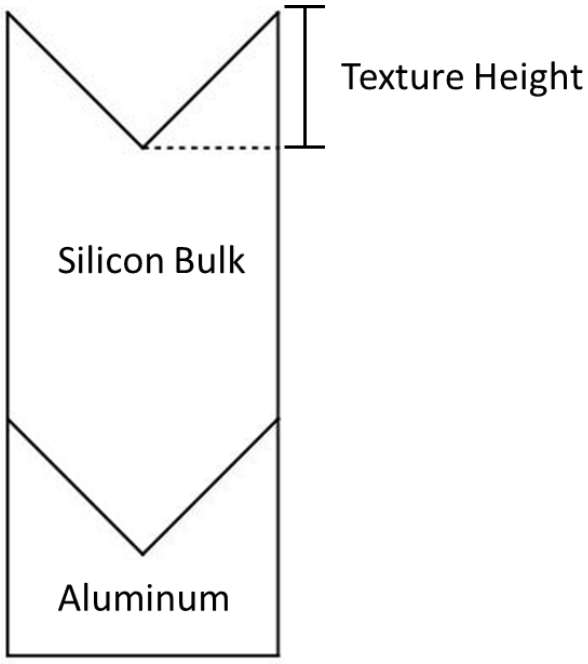

Figure 4.11 The 2D cross-sectional structure of a textured (100) silicon solar cell without front metal electrode. The texture height is marked for reference.

As can be seen in Table 4.7, the MAOC and percentage current generated in the shaded region is almost the same for both the cases, with textures height of 2 µm and 3 µm respectively. These values are plotted in Figure 4.12 and Figure 4.13.

Table 4.7 MAOC values and the percentage current generated in a solar cell with two different texture heights

Cell Thickness (µm)	**MAOC(A)**		**% Current Generated in the Shaded Region**	
40	Texture=2 µm	8.46	Texture=2 µm	0.175
	Texture=3 µm	8.48	Texture=3 µm	0.175
120	Texture=2 µm	8.83	Texture=2 µm	0.3
	Texture=3 µm	8.85	Texture=3 µm	0.3
180	Texture=2 µm	9.04	Texture=2 µm	0.34
	Texture=3 µm	9.02	Texture=3 µm	0.35

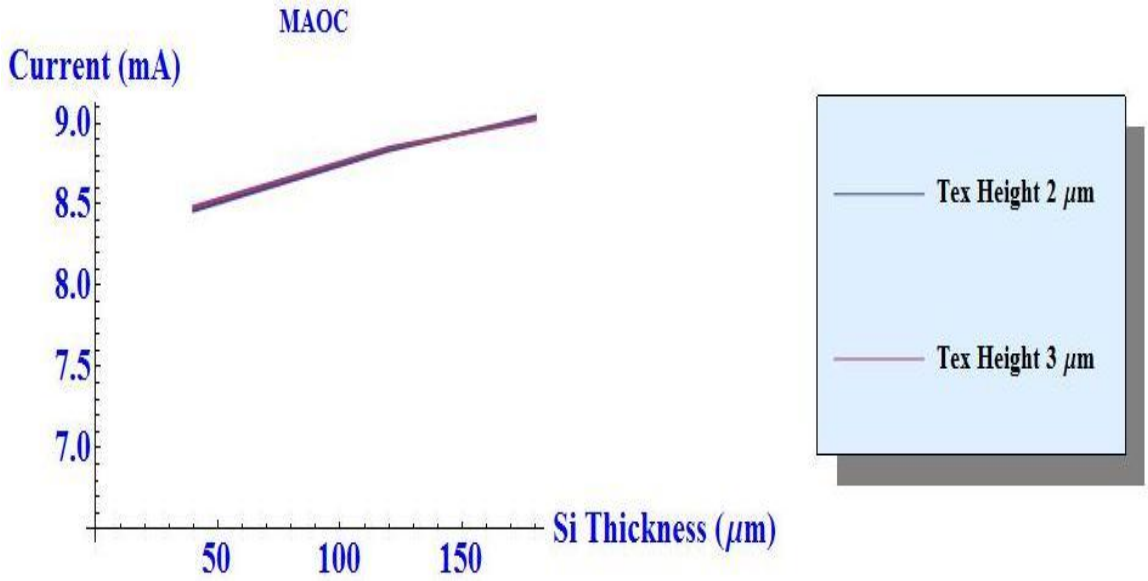

Figure 4.12 Comparison of MAOC values for solar cells with texture height 3 µm and 2 µm.

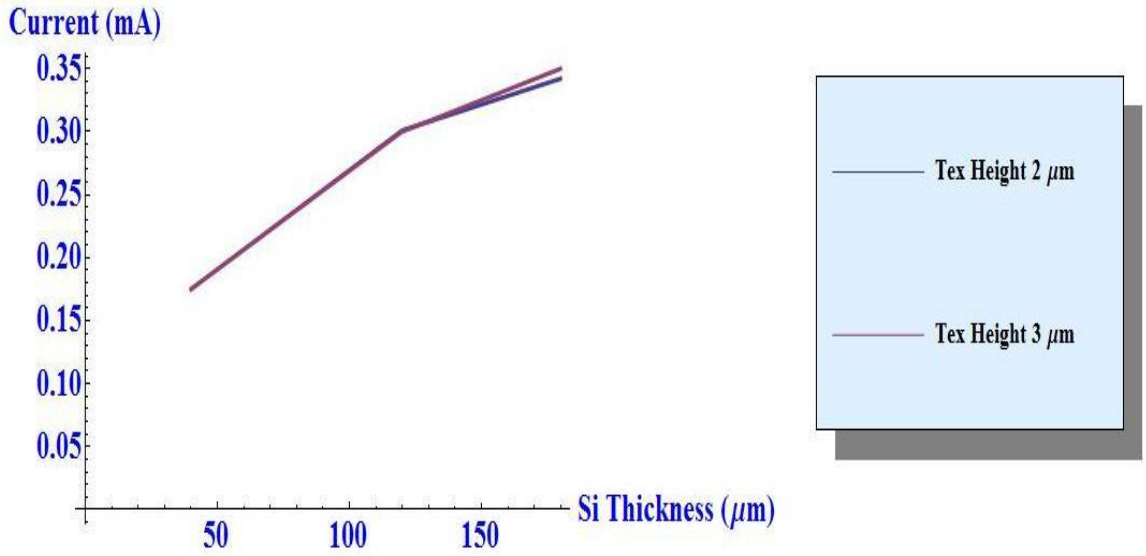

Figure 4.13 Comparison between the current generated in the shaded region for solar cells with texture height 3 µm and 2 µm.

From the plots in Figure 4.12 and 4.13, it is clearly visible that the difference in the MAOC values and the current generated in the shaded region for solar cells with texture heights of 3 µm and 2 µm are negligible, leading to the

conclusion that the effect of texture height can be ignored while designing the structure for a solar cell, as long as the texture size is larger than the wavelength of the incident light.

4.3 Conclusions

The new version of PV Optics has been used to carry out simulations for different solar cell structures in order to identify their optical performance. Calculations were carried out for:

- various silicon absorber layer thicknesses,
- different front metal electrode widths, and
- texture heights.

The results for these calculations have also been summarized to give the effect of each of these parameters on the performance of solar cells.

CHAPTER 5

SUMARY OF RESULTS: SOLAR CELL ENCAPSULATED IN A MODULE

5.1 Introduction

Solar cells, by nature, are very brittle and cannot handle a lot of stress. They have to be packaged in a module, also called solar panels, before installation in order to make them sturdy enough to endure all stresses during installation and functioning. Modules also contain an array of solar cells connected together electrically to give the desired current output. So they contain all the electrical wiring and connections that would lead to proper current extraction from the encapsulated array of solar cells. Modules are generally made using the following constituents:

- top glass enclosure,
- top encapsulant,
- array of solar cells,
- a back sheet for support,
- a junction box, and
- an enclosing fame for mechanical support.

Figure 5.1 shows all these constituents of a solar module and also a finished solar panel. Sunlight is incident from the top of the module. Hence, before reaching the surface of the cell, sunlight has to first pass through the glass and the encapsulant layers. These extra intermediate layers on top of a cell result in the increase in the reflectance losses in the module compared to a stand

alone solar cell. This is accompanied by a saving in further optical losses due to the light trapping capabilities of the intermediate layers. Figure 5.2 elucidates both these optical effects clearly. It is of utmost importance that the refractive indices of the glass layer and the encapsulant layer are matched as closely as possible in order to inhibit any reflectance loss from the glass-encapsulant interface. Figure 5.2 takes this refractive index matching into account.

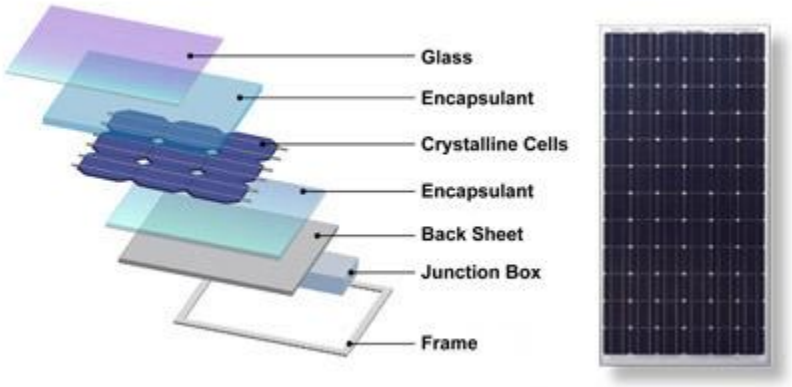

Figure 5.1 The various constituents of a solar module and a solar panel [172].

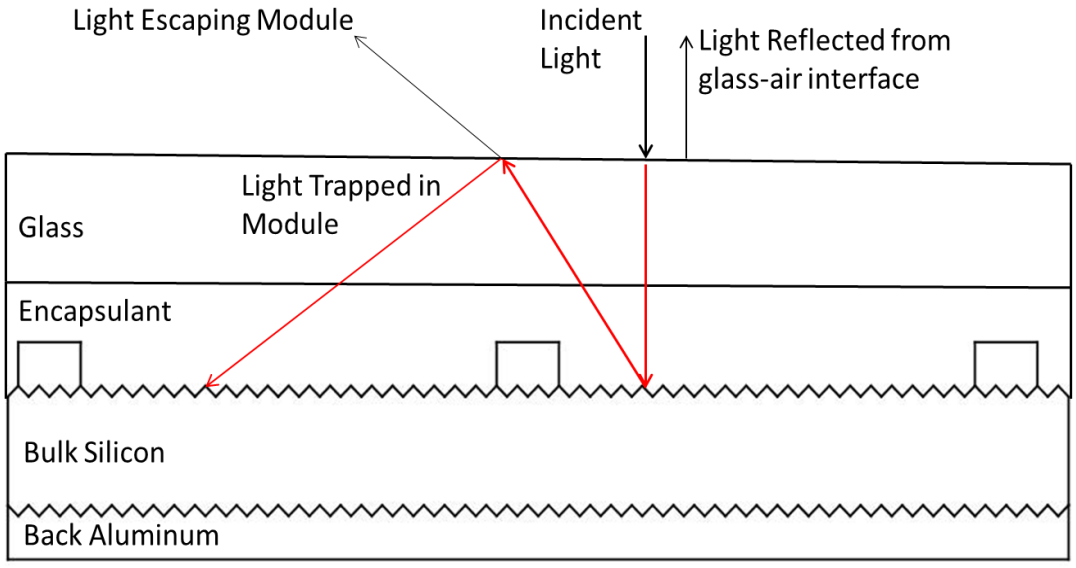

Figure 5.2 Optical effects in a module.

This chapter presents the simulation results of the effect of encapsulation on the performance of solar cells. The glass and encapsulant thicknesses have been kept constant for all calculations in order to spot general trends in module performances depending on the front metal architecture. Table 5.1 spells out the various properties of the glass and encapsulant layers.

Table 5.1 Properties of glass and encapsulant layers used for simulations

Layer	**Properties**	
Glass	Thickness	100 µm
	Refractive Index	1.52
	Extinction Coefficient	0.0
Encapsulant	Thickness	50 µm
	Refractive Index	1.50
	Extinction Coefficient	0.0

5.2 Simulation Results

In order to make a systematic study of the effect of encapsulation on the performance of solar cells, calculations in this chapter are a continuation from Chapter 4. The cell structures are the same as before with the exception that glass and encapsulant layers have been added on top. One difference from the previous chapter is that the effect of texture height, upon encapsulation, has not been presented here due to the previous observation that this makes no

observable difference in the performance of the cell. Another difference is the addition of calculation results for various finger and busbar heights under encapsulation. This has been done to investigate whether metal height variation has any effect on the light trapping characteristics of the glass-air interface.

Two important points have to be noted at the outset in order to make a meaningful study of the effect of encapsulation. Firstly, as shown in Table 5.1, refractive indices of the glass and encapsulant materials have a very close match. This means that, for all practical purposes, there is no optical loss at this interface. Secondly, for the refractive index of glass used for the calculations, at normal incidence, there is a direct loss of 4.258% of the incident light at the air-glass interface. This would lead to the supposition that the total current generated in a cell encapsulated in a module should be reduced by the same amount compared to the case with no encapsulation. But as shown in Figure 5.1, the reduction in current from a solar cell placed in a module would be slightly less than this value of 4.258% because of the inherent light trapping characteristics of the module.

5.2.1 Variation in Silicon Absorber Layer Thickness

Calculations are presented for thicknesses of 40 μm, 80 μm, 120 μm, and 180 μm. All the other structural parameters have been kept the same as for the case of without encapsulation for comparison. Table 5.2 summarizes the results of these calculations. Figures 5.3-5.6 presents all the above results in graphical form along with the results for only a solar cell to elucidate the effect of encapsulation of a solar cell.

Table 5.2 Summary of calculated results for different absorber layer thicknesses and metal finger with of 100 µm

Silicon Thickness (µm)	MOAC (A)	Ref. Loss (mA)	Back Metal Abs. Loss (mA)	Front Metal Abs. Loss (mA)	%age change in MAOC in module
40	8.13	1209.16	681.31	2.55	0.16
80	8.4	1081.5	552.63	2.59	0.22
120	8.55	993.16	496.46	2.73	0.27
150	8.63	964.82	450.05	2.66	0.295
180	8.72	918.4	411.27	2.47	0.32

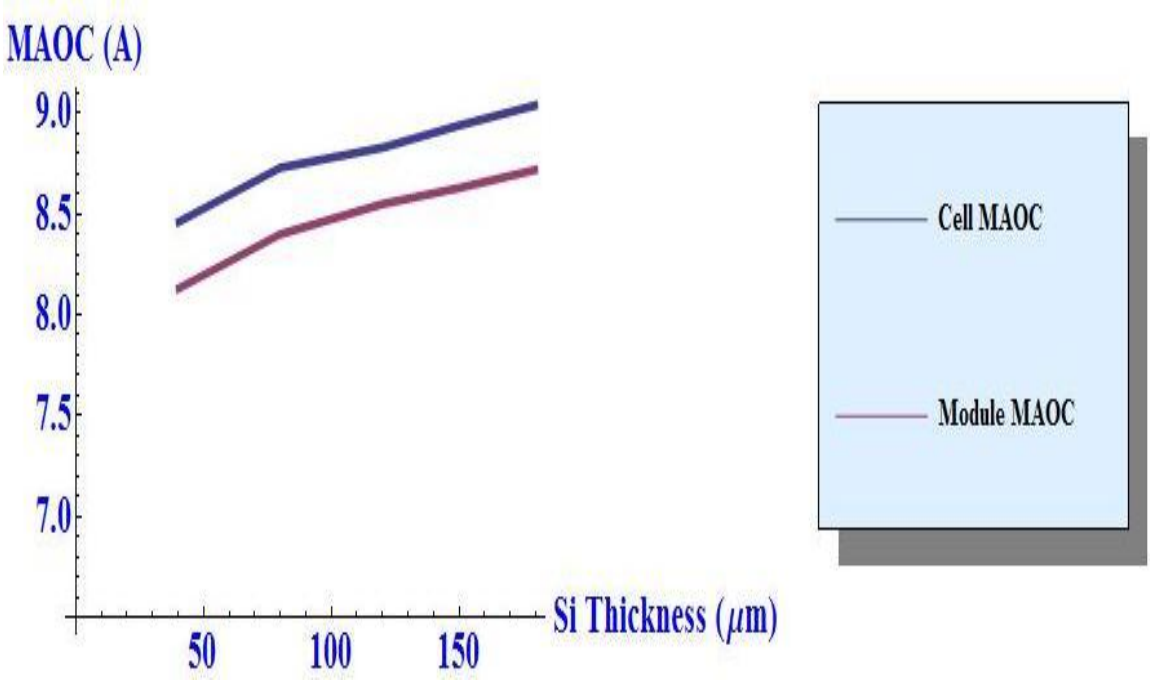

Figure 5.3 Plot of MAOC of (a) cell, and (b) module with respect to silicon thickness.

.

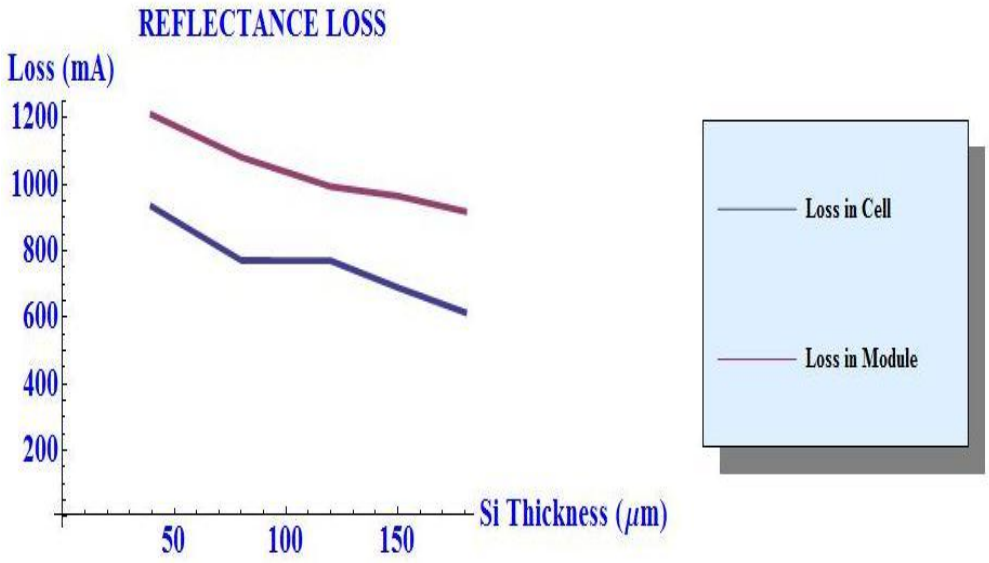

Figure 5.4 Plots of Reflectance Losses for (a) cell, and (b) module.

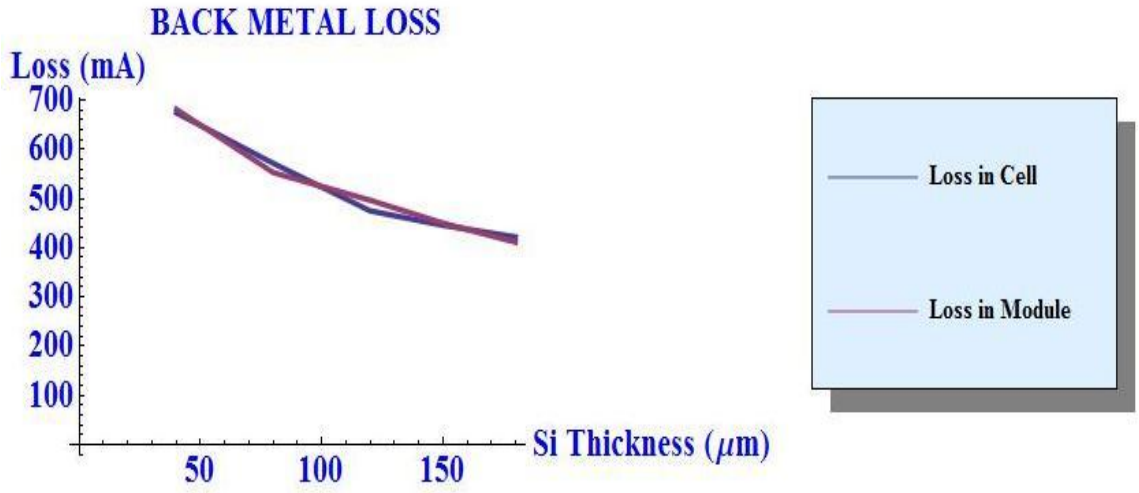

Figure 5.5 Plots of Back Metal Losses for (a) cell, and (b) module.

The total current produced in a solar cell upon encapsulation in a module is always lesser than when un-encapsulated. This change in the current is almost entirely due to the increase in the reflectance loss of a cell upon encapsulation. This is borne out of the plots in Figure 5.5 which shows that there is negligible

change in back metal loss in a cell upon encapsulation. This can be explained by taking into account the light trapping properties of a module.

Some of the photons, which have low absorption coefficient in silicon, upon leaving the cell surface are reflected back in the silicon absorber layer from the glass-air interface. These reflected photons then add to the overall current in the module as well as the back metal loss. This aids in keeping the back metal loss practically the same for a solar cell, within or without a module.

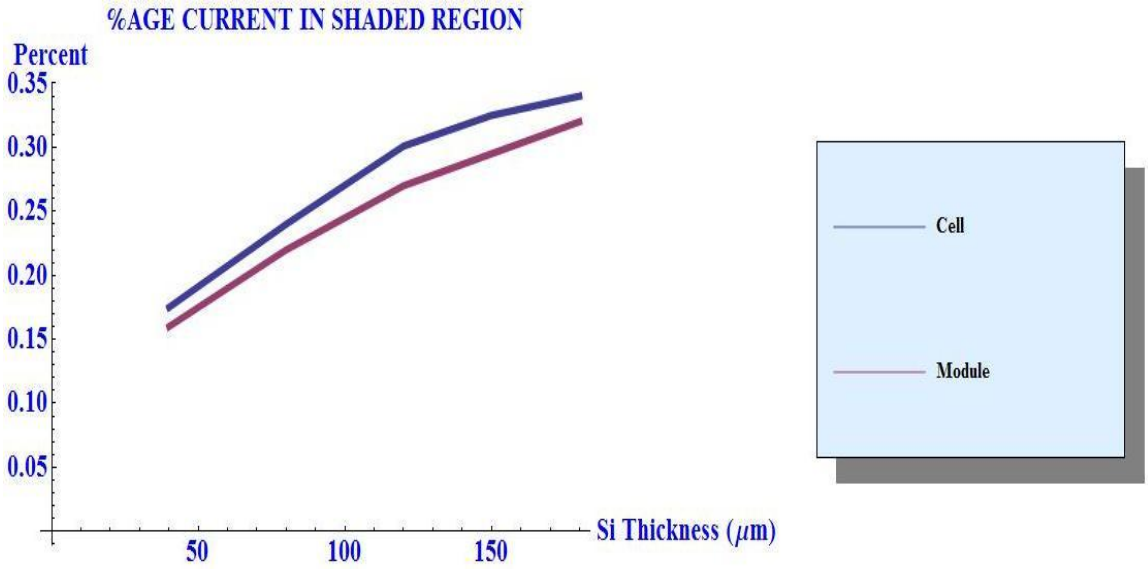

Figure 5.6 Plot of percentage current generated in the shaded region.

Another aspect of encapsulation that is also worth mentioning is the reduction in the total current generated under the shaded region in a module. This is simply an artifact of the increase in the reflectance loss from a cell upon encapsulation due to which less light diffuses into the shaded region of the solar cell. Figures 5.7 and 5.8 show the photon absorption pattern under the shaded region of a module with 40 μm silicon thickness to illustrate this point.

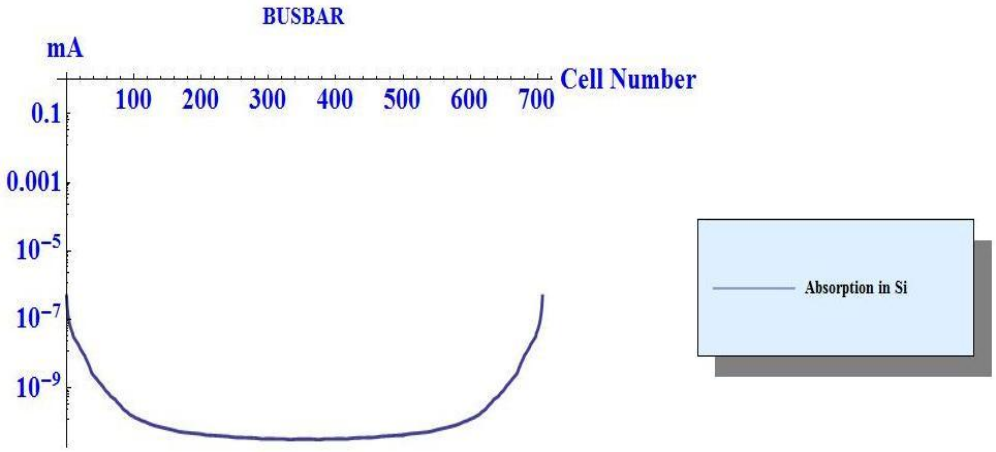

(a)

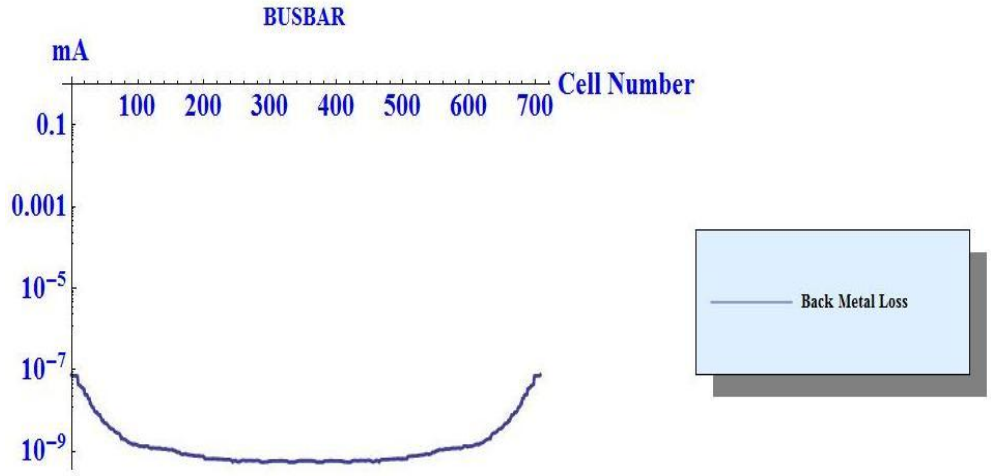

(b)

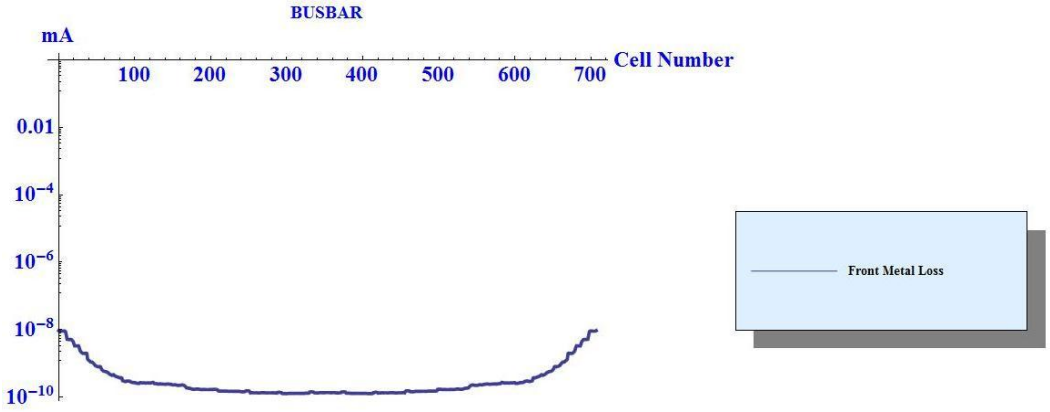

(c)

Figure 5.7 Absorption under busbar in (a) Silicon, (b) Back Metal, and (c) Front Metal for a module with a 40 µm thick silicon absorber layer.

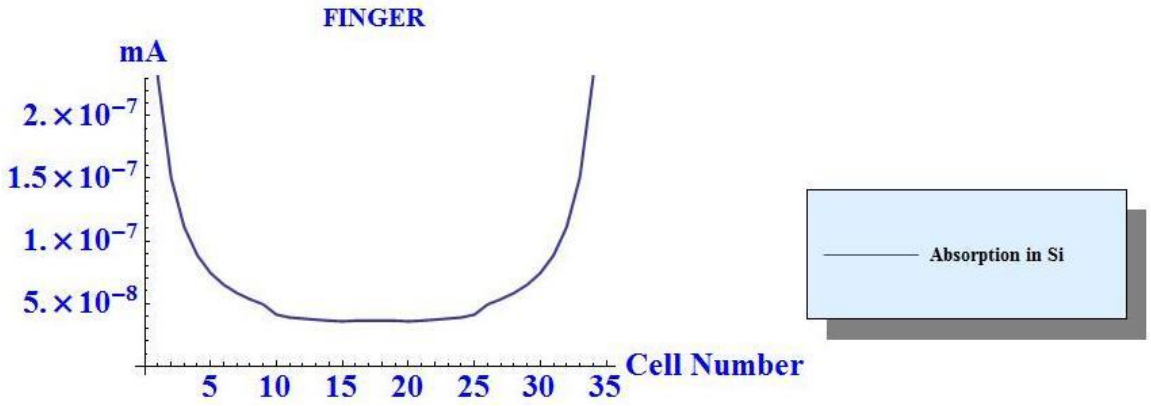

(a)

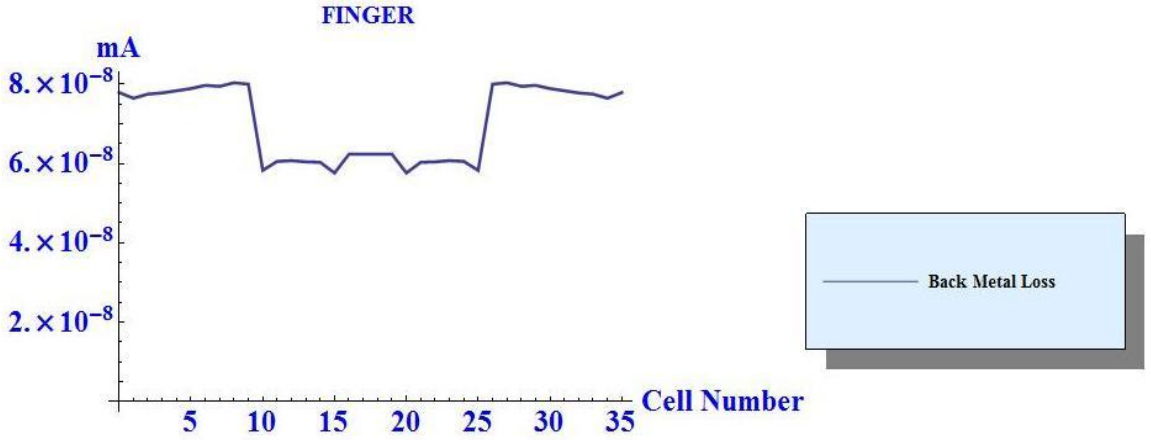

(b)

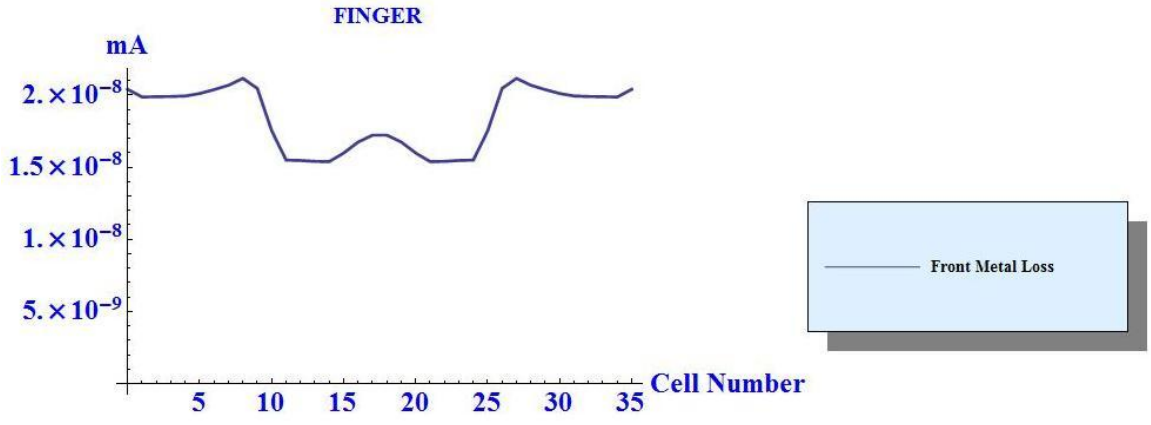

(c)

Figure 5.8 Absorption under a finger in (a) Silicon, (b) Back Metal, and (c) Front Metal for a module with a 40 µm thick silicon absorber layer.

5.2.2 Variation in Metal Finger Width

As in the last chapter, results of the calculation are presented for three different metal finger widths of (a) 25 µm, (b) 50 µm, and (c) 75 µm for silicon thickness of (a) 40 µm, (b) 80 µm, (c) 120 µm, and (d) 180 µm. Tables 5.3-5.5 show the summary of these results. There are two points that are of interest concerning the results shown above. The first one is to see if a change in metal finger height makes any difference in the MAOC, the losses or the amount of current generated in the shaded region in the module. The second point of interest is to compare the above results with the case of an un-encapsulated solar cell. Figures 5.9-5.12 show comparative plots for the first point.

Table 5.3 Summary of calculated results for different absorber layer thicknesses and metal finger width of 25 µm

Absorber Layer Thickness (µm)	Maximum Achievable Output Current (A)	Reflectance Loss (mA)	Back Metal Absorption Loss (mA)	Front Metal Absorption Loss (mA)	% age current generated in the shaded region
40	8.13	1222.69	683.54	3.98	0.46
80	8.4	1098.13	553.15	3.23	0.53
120	8.55	1011.301	496.58	2.9	0.565
180	8.72	937.44	411.281	2.48	0.605

Table 5.4 Summary of calculated results for different absorber layer thicknesses and metal finger width of 50 µm

Absorber Layer Thickness (µm)	Maximum Achievable Output Current (A)	Reflectance Loss (mA)	Back Metal Absorption Loss (mA)	Front Metal Absorption Loss (mA)	% age current generated in the shaded region
40	8.13	1212.78	682.52	3.29	0.28
80	8.4	1085.76	553.26	3.22	0.35
120	8.55	998.88	496.63	2.89	0.39
180	8.72	924.76	411.27	2.48	0.44

Table 5.5 Summary of calculated results for different absorber layer thicknesses and metal finger width of 75 µm

Absorber Layer Thickness (µm)	Maximum Achievable Output Current (A)	Reflectance Loss (mA)	Back Metal Absorption Loss (mA)	Front Metal Absorption Loss (mA)	% age current generated in the shaded region
40	8.11	1208.02	680.74	2.9	0.202
80	8.36	1080.75	552.01	2.93	0.275
120	8.54	992.8	495.88	2.94	0.32
180	8.69	918.93	410.58	2.5	0.37

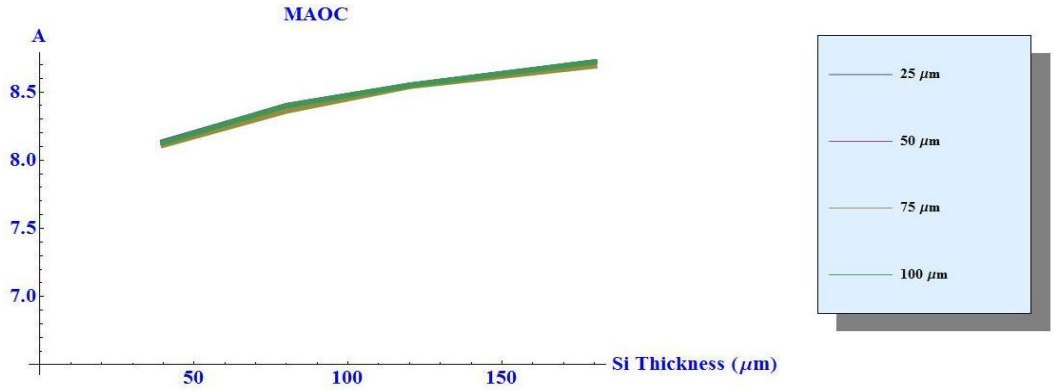

Figure 5.9 Plot of MAOC values for module with respect to silicon thickness for metal finger width of (a) 100 µm, (b) 75 µm, (c) 50 µm, and (d) 25 µm.

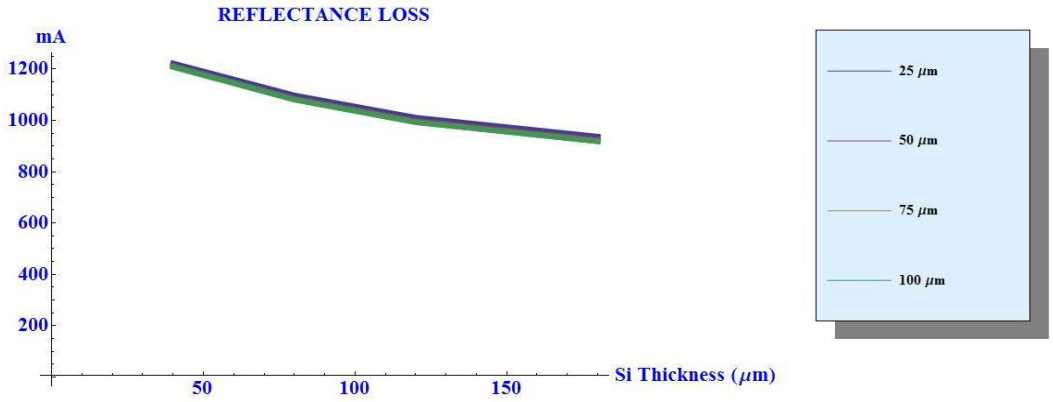

Figure 5.10 Plot of reflectance loss values for module with respect to silicon thickness for metal finger width of (a) 100 µm, (b) 75 µm, (c) 50 µm, and (d) 25 µm.

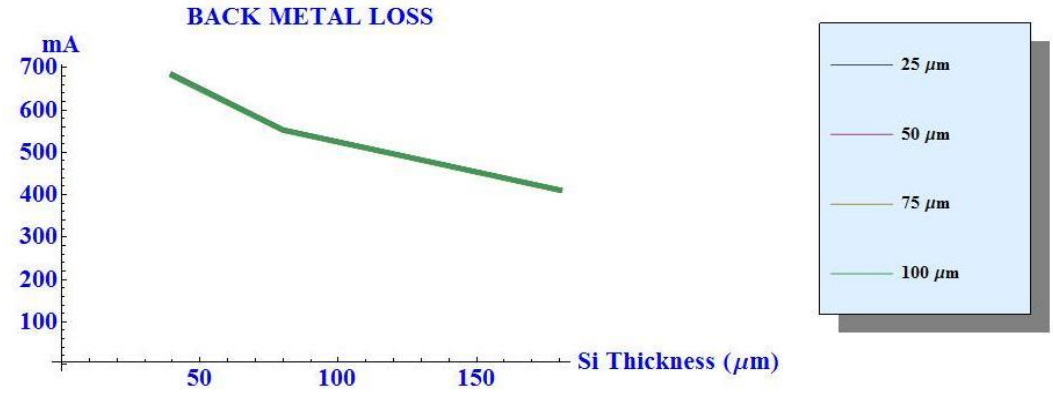

Figure 5.11 Plot of reflectance loss values for module with respect to silicon thickness for metal finger width of (a) 100 µm, (b) 75 µm, (c) 50 µm, and (d) 25 µm.

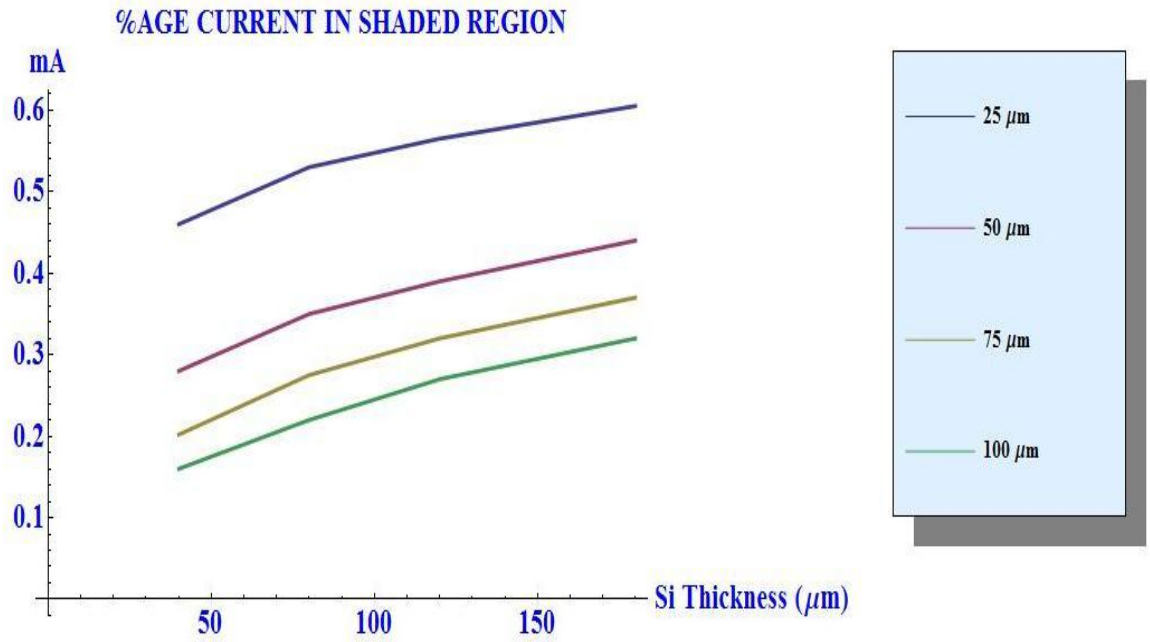

Figure 5.12 Plot of percentage current produced in shaded region for module with respect to silicon thickness for metal finger width of (a) 100 µm, (b) 75 µm, (c) 50 µm, and (d) 25 µm.

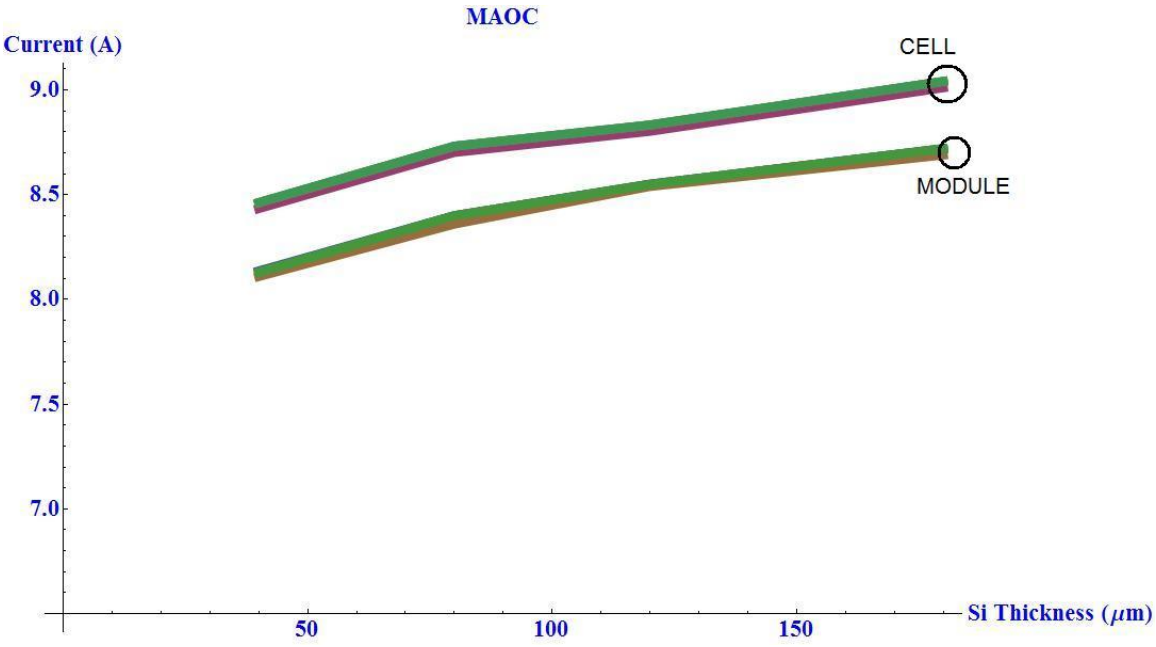

Figure 5.13 Plot of MAOC values for cell and module with respect to silicon thickness for metal finger width of (a) 100 µm, (b) 75 µm, (c) 50 µm, and (d) 25 µm.

Figures 5.12-5.14 clearly show that there is negligible change in the MAOC values as well as the reflectance and the back metal loss values upon varying the width of the metal fingers. It would be pertinent to remember here that while changing their width, the total area under shading was kept constant to facilitate a meaningful comparison. This means that, as the width decreases, the distances between the metal fingers decrease as well. Figure 5.10 shows the plots of the current generated in the shaded region for the various widths of metal fingers in a module.

Figure 5.13 shows the clear segregation of the cell and module MAOC values for different metal finger widths. Figure 5.14 shows a similar plot for reflectance losses for cell and module for reference.

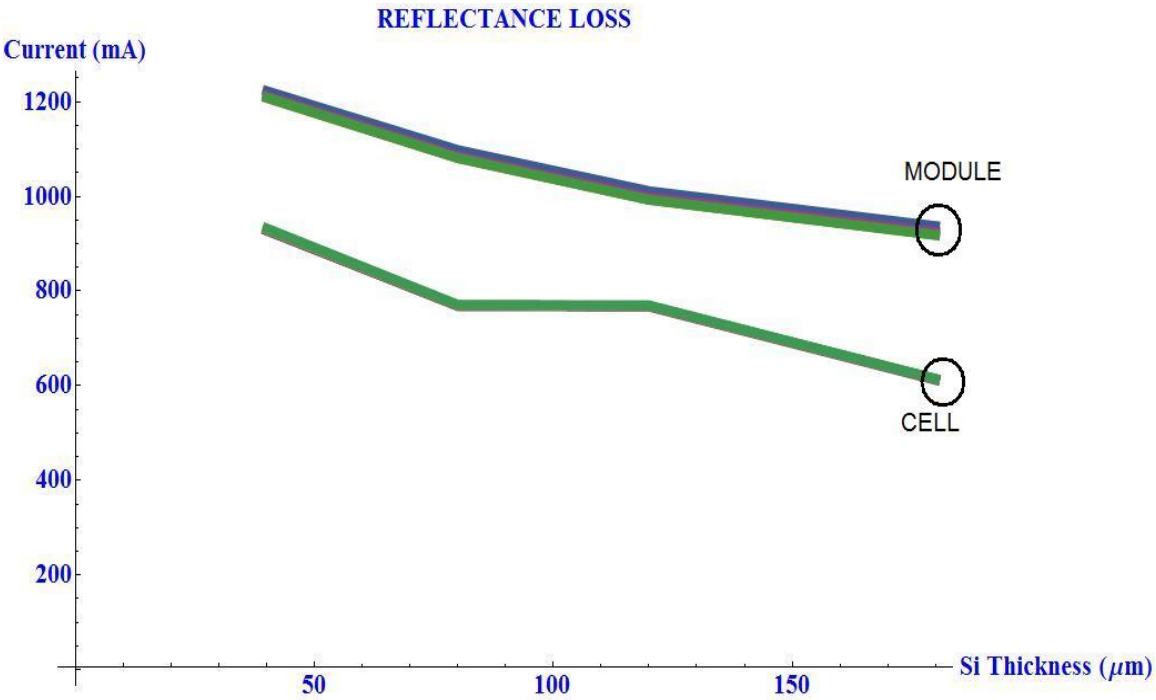

Figure 5.14 Plot of reflectance loss for cell and module with respect to silicon thickness for metal finger width of (a) 100 µm, (b) 75 µm, (c) 50 µm, and (d) 25 µm.

5.2.3 Variation in Front Metal Height

The height of the front metal electrodes, fingers and busbars, is an important parameter in terms of cost as well as carrier extraction. In this section, the effect of the height of the front metal electrode architecture on the optical performance of an encapsulated solar cell is investigated. Simulations have been performed for a total of four front metal heights: (a) 10 µm, (b) 20 µm, (c) 30 µm, and (d) 40 µm, with finger width of 100 µm and a standard busbar width of 2 mm. All the calculations up to this point have been performed on cell structures with front metal heights of 20 µm.

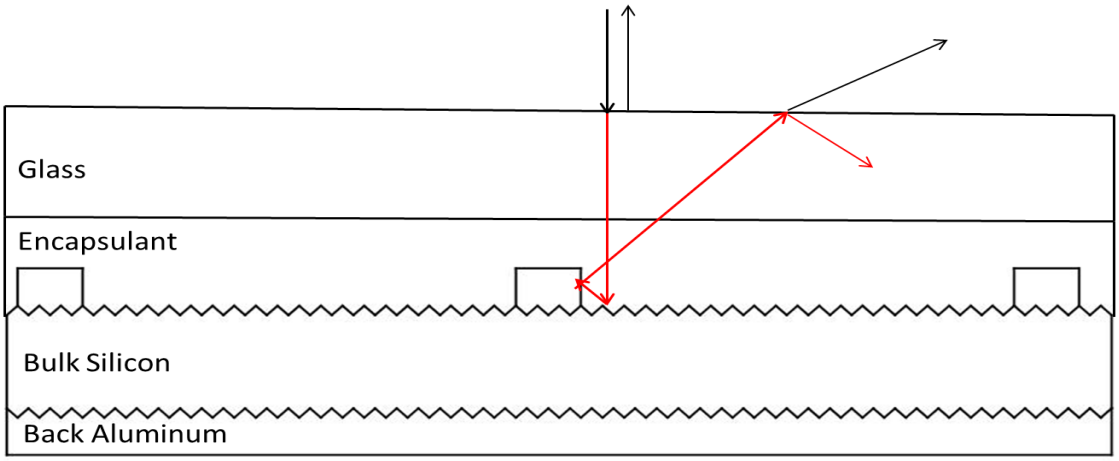

Figure 5.15 Effect of metal height on module optics.

The main reason for investigating the effect of the front metal heights on the optical performance of a module is depicted in Figure 5.15. The red arrows depict the direction of propagation of light in the module while the black arrows depict the light outside of the module. As can be seen from the red arrows, light can be incident on the front surfaces of the front electrode grid and get deflected. This light then strikes the glass-air interface from where, a small fraction remains

Table 5.6 Summary of calculated results for different absorber layer thicknesses and metal finger height of 10 µm

Absorber Layer Thickness (µm)	Maximum Achievable Output Current (A)	Reflectance Loss (mA)	Back Metal Absorption Loss (mA)	Front Metal Absorption Loss (mA)	% age current generated in the shaded region
40	8.13	1209.251	681.34	2.56	0.16
80	8.4	1081.51	552.69	2.61	0.22
120	8.55	993.11	496.52	2.76	0.27
180	8.72	918.43	411.27	2.47	0.32

Table 5.7 Summary of calculated results for different absorber layer thicknesses and metal finger height of 30 µm

Absorber Layer Thickness (µm)	Maximum Achievable Output Current (A)	Reflectance Loss (mA)	Back Metal Absorption Loss (mA)	Front Metal Absorption Loss (mA)	% age current generated in the shaded region
40	8.13	1209.01	681.27	2.56	0.16
80	8.4	1081.29	552.62	2.61	0.22
120	8.55	992.99	496.43	2.76	0.27
180	8.72	918.33	411.3	2.47	0.32

inside the module while the rest is lost as reflectance loss. The amount of light incident on the front metal is related to their height. This might have an effect on

the final light trapping capabilities of the module itself. Tables 5.6-5.8 provide the summary of calculations for the three mentioned front metal heights.

Table 5.8 Summary of calculated results for different absorber layer thicknesses and metal finger height of 40 µm

Absorber Layer Thickness (µm)	Maximum Achievable Output Current (A)	Reflectance Loss (mA)	Back Metal Absorption Loss (mA)	Front Metal Absorption Loss (mA)	% age current generated in the shaded region
40	8.13	1208.88	681.23	2.56	0.16
80	8.4	1081.23	552.57	2.61	0.22
120	8.55	992.87	496.43	2.76	0.27
180	8.72	918.28	411.29	2.47	0.32

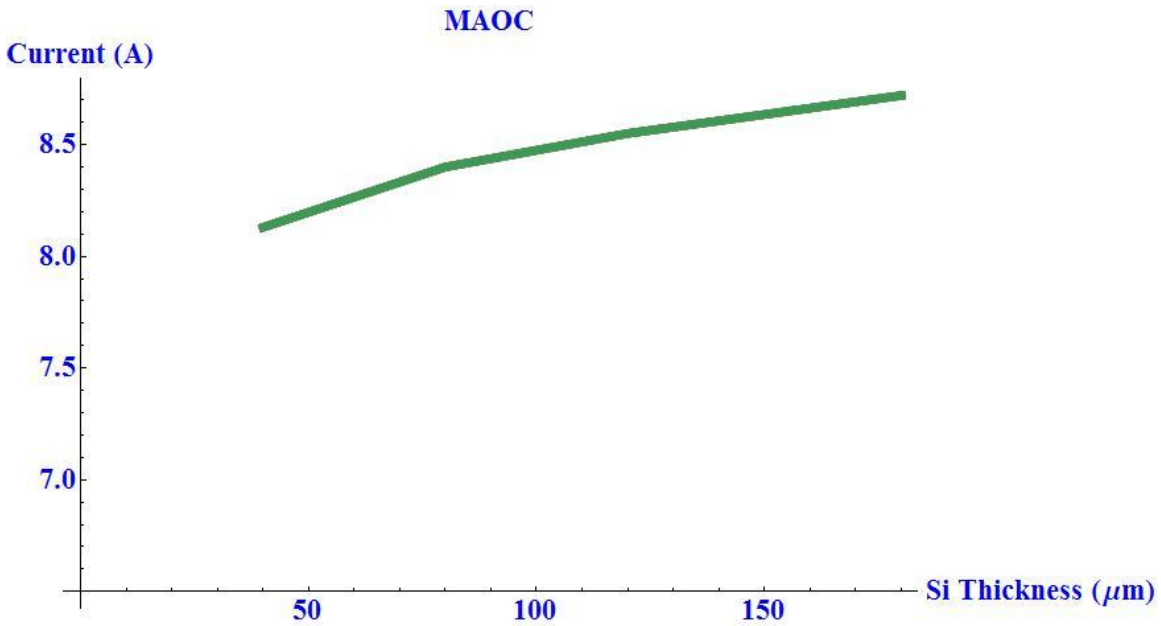

Figure 5.16 MAOC plots for metal height thicknesses of (a) 10 µm, (b) 20 µm, (c) 30 µm, and (d) 40 µm.

It is again interesting to note that the MAOC values for various front metal heights for each silicon absorber layer thickness is unchanging to second decimal. Any change in current due to the heights in silver metal is only beyond this point. Silver, being such a good reflector, does not absorb a huge amount light that is incident on it. This again stresses the point that the optical effects, due to the above mentioned changes in solar cell structure, are minimal and hence, the electrical properties take precedence over the optical effects.

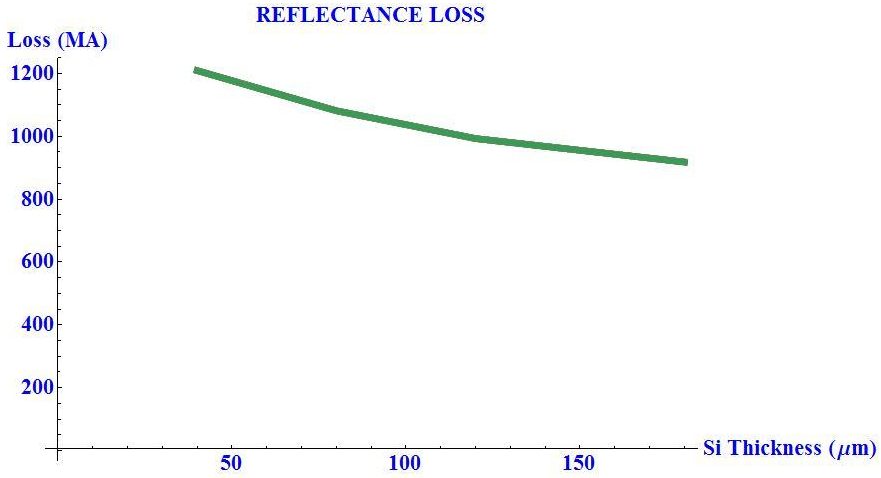

Figure 5.17 Reflectance loss plots for metal height thickness of (a) 10 µm, (b) 20 µm, (c) 30 µm, and (d) 40 µm.

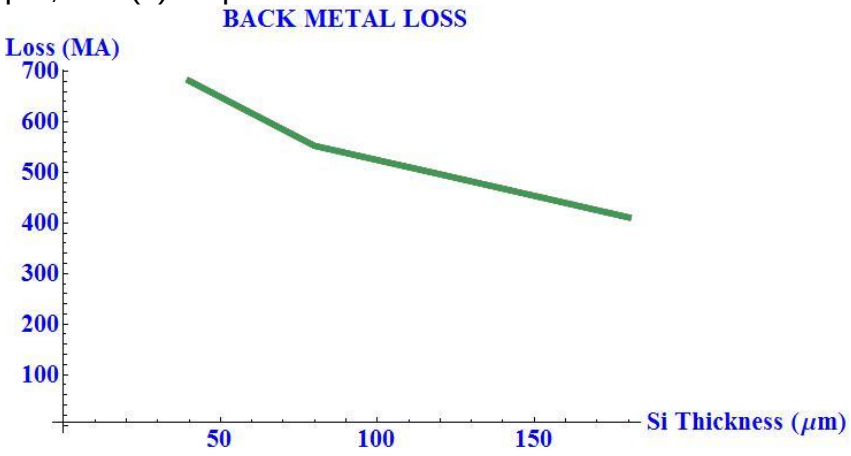

Figure 5.18 Back metal loss plots for metal height thickness of (a) 10 µm, (b) 20 µm, (c) 30 µm, and (d) 40 µm.

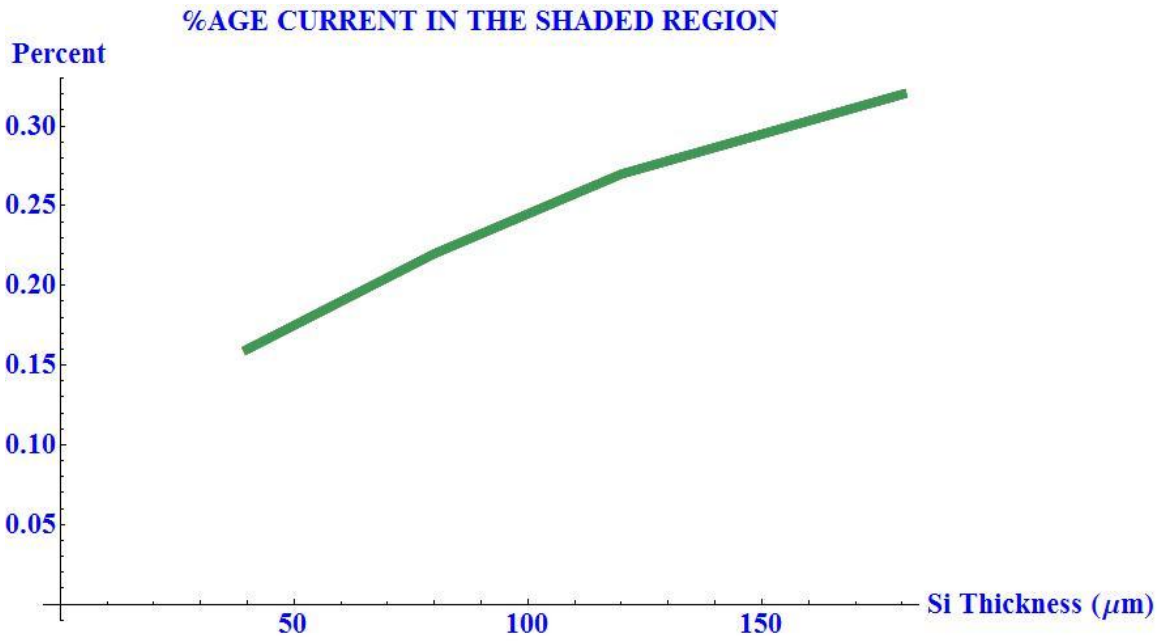

Figure 5.19 Percentage current generated in the shaded region of a module plots for metal height thickness of (a) 10 µm, (b) 20 µm, (c) 30 µm, and (d) 40 µm.

Figures 5.13-5.16 also show that the effect of the front metal is minimal on the optical performance of solar cells.

5.3 Conclusions

All the results of simulations using the new ray tracing C++ code for PV Optics 4.0 have been presented in this Chapter. The structural parameters used for these calculations have been kept the same as in Chapter 4 except for the change that the cells have been encapsulated in a module. Calculations have also been done to see the effect of front metal height on the optical performance of a module. The results show that there is minimal effect of the front metal electrode architecture used presently in commercial single crystal (100) silicon solar cell modules. This emphasizes the fact that carrier transport is the main

factor that should be taken into account while designing the front metal electrode architecture in cells and modules.

CHAPTER 6

CONCLUSIONS AND FUTURE DIRECTIONS

The objective of this dissertation was to develop a new and complete model to incorporate the front metal electrode architecture that are used in commercial single crystal (100) orientation silicon solar cells for optical simulations. This new model was implemented in a computer program written in C++ to be added as a new module to *PV Optics Ver. 4.0*. Investigations have been carried out on various front metal architecture and solar cell structures to study their effect on the performance of solar cells from a purely optics point of view.

6.1 Conclusions on Front Metal Architecture Modeling

It has been established during the course of this research that a simpler 2D structural as well as procedural model can be used to carry out simulations on a 3D structure of single crystal (100) oriented silicon solar cells. Reducing such a complex 3D model into a 2D model has the following advantages:

- The 2D model has the same accuracy as the corresponding 3D model,
- This new model reduces the calculation time and the computing budget for a finished 156 mm X 156 mm solar cell by at least one order of magnitude from the corresponding 3D computation.
- The computational budget required to do the optical simulations using the new model and computer program is also substantially reduced.

The use of this model to study the effect of the front metal architecture of a solar cell on its performance has shown some very interesting results. The total current generated in a finished 156 mm X 156 mm solar cell increases with the

subsequent increase in the silicon absorber layer thickness. It is found that the increase in current, upon increasing the silicon thickness from 40 µm to 180 µm (change in thickness of 350%), results in the increase in the MAOC by only 6.855%. This is a clear indicator that use of better light trapping and wafer handling technologies will lead to a decrease in silicon wafer thickness for solar cell production. The potential to cut production costs due to this is immense and can eventually lead solar energy to become competitive with other forms of energy in the near future.

This research also establishes, for the first time, that there is a very minimal effect of the front metal architecture on the performance of commercial single crystal silicon solar cell structures. Solar cell designers have a simpler task with one less variable, i.e., optical design, to come up with new solar cell architecture. But it is also relevant to mention that the main challenge in designing solar cells would be to keep the shaded region as small as possible to be able to use the maximum volume of the device for current generation.

It has been firmly established that, for optical calculations, 2D models can be used with great accuracy to tackle a 3D problem. This work should act as a catalyst for the incorporation of many other front and back metal electrode architectures for optical simulations. The effect of other metal geometries and architectures are still open to investigation.

6.2 Future Directions

This work should be extended further in order to study the effect of novel front and back metal electrode structures on solar cell performance. Following is the scope for expanding and improving the present research:

1) this model can be expanded to include texture etched multicrystalline silicon solar cells; No such model exists as yet,

2) introduction of novel light trapping technologies, discussed in Chapter 3, into the existing model;

3) extension of this model to also handle thin film solar cells;

4) introduction of new metal architectures such as inter-digitated contacts in the existing model;

5) incorporate parallel processing into the existing C++ code to further reduce the simulation time.

REFERENCES

1. D.O.E., U.S. *The History of Solar*. 2012 [cited 2012 11/06]; Available from: http://www1.eere.energy.gov/solar/pdfs/solar_timeline.pdf.

2. M.Wolf, *Historical Development of Solar Cells*. Solar Cells, ed. C.E. Backus1976, New York: IEEE Press.

3. A.Carr, et al. *How are Solar Cells made?* 1999 [cited 2012 11/06]; Available from: http://www.esdalcollege.nl/eos/vakken/na/zonnecel.htm.

4. B.Averill and P.Eldredge. *General Chemistry: Principles, Patterns, and Applications*. 2007 [cited 2012 11/05]; Available from: http://images.flatworldknowledge.com/averillfwk/averillfwk-fig12_027.jpg.

5. W.U.Boeglin. *P-N Junction*. 2011 [cited 2012 11/05]; Available from: http://wanda.fiu.edu/teaching/courses/Modern_lab_manual/pn_junction.html.

6. N.W.Ashcroft and N.D.Mermin, *Solid State Physics*, 1976, Thompson learning.

7. L.V.Azaroff and J.J.Brophy, *Electronic Processes in Materials*1963: McGraw-Hill.

8. S.Wang, *Solid State Electronics*, 1996, McGraw-Hill: New York.

9. AllAboutCircuits.com. *Diodes*. 2012 [cited 2012 11/05]; Available from: http://solarwiki.ucdavis.edu/The_Science_of_Solar/1._Basics/A._Introductory_Physics_for_Solar_Application/II._Electricity/5._Diodes.

10. D.R.Williams. *Sun Fact Sheet*. 2012 [cited 2012 11/05]; Available from: http://nssdc.gsfc.nasa.gov/planetary/factsheet/sunfact.html.

11. M.P.Thekackara, *The Solar Constant and the Solar Spectrum Measured form a Research Aircraft*, 1970, NASA Technical Report No. R-351.

12. M.A.Green, *Solar Cells: Operating Principles, Technology, and System Applications* 1982, Prentice-Hall: New Jersey. p. 5.

13. P.R.Gast, *Solar Radiation*, in *Handbook of Geophysics*, C.F. Campen, Editor 1960, Macmillan: New York. p. 14-16.

14. Gast, P.R., *Solar Radiation*, in *Handbook of Geophysics*, C.F. Campen, Editor 1960, Macmillan: New York. p. 16-30.

15. F-J.Haug. *Irradiation spectrum*. [cited 2012 11/05]; Available from: http://www.superstrate.net/pv/illumination/spectrum.html.

16. *Terrestrial Photovoltaic Measurement Procedure*, 1977, NASA Report ERDA/NASA/1022-77/16.

17. *Principal Conclusion of the American Physical Society Study Group on Solar Photovoltaic Energy Conversion*, 1979, American Physical Society: New York.

18. D.M.Chapin, C.S.Fuller, and G.L.Pearson, *A New Silicon p-n Junction Photocell for Converting Solar Radiation into Electrical Power.* Journal of Applied Physics, 1954. **25**(5): p. 676.

19. M.S.Green, *Solar Cells*, in *Modern Semiconductor Device Physics*, S.M.Sze, Editor 1998, Wiley Interscience: New York.

20. M.A.Green, *Thin-film solar cells: review of materials, technologies and commercial status.* J Mater Sci: Mater Electron, 2007. **18**: p. S15–S19.

21. A.V.Shah, R.Platz, and H.Keppner, *Thin-film silicon solar cells: A review and selected trends.* Solar Energy Materials and Solar Cells, 1995. **38**(1-4): p. 501-520.

22. M.Gratzel, *Dye-sensitized solar cells.* Jounal of Photochemistry and Photobiology C: Photochemistry Reviews, 2003. **4**(2): p. 145-153.

23. M.Gratzel, *Solar Energy Conversion by Dye-Sensitized Photovoltaic Cells.* Inorg. Chem., 2005. **44**(20): p. 6841-6851.

24. K.L.Chopra, P.D.Paulson, and V.Dutta, *Thin-Film Solar Cells: An overview.* Prog. Photovolt: Res. Appl., 2004. **12**(2-3): p. 69-92.

25. M.Pagliaro, R.Ciriminna, and G.Palmisano, *Flexible Solar Cells.* ChemSusChem, 2008. **1**(11): p. 880-891.

26. A.Romeo, et al., *Development of Thin-film Cu(In,Ga)Se2 and CdTe Solar Cells.* Prog. Photovolt: Res. Appl., 2004. **12**(2-3): p. 93-111.

27. X.Wu, *High-efficiency polycrystalline CdTe thin-film solarcells.* Solar Energy, 2004. **77**(6): p. 803-814.

28. A.Shah, et al., *Photovoltaic Technology: The Case for Thin-Film Solar Cells.* Science, 1999. **285**(5428): p. 692-698.

29. J.H.Bang and P.V.Kamat, *Quantum Dot Sensitized Solar Cells. A Tale of Two Semiconductor Nanocrystals: CdSe and CdTe.* ACS Nano, 2009. **3**(6): p. 1467–1476.

30. R.W.Birkmire and E.Eser, *POLYCRYSTALLINE THIN FILM SOLAR CELLS:Present Status and Future Potential.* Annual Review of Materials Science, 1997. **27**: p. 625-653.

31. Dobson, K.D., et al., *Stability of CdTe/CdS thin-film solarcells.* Solar Energy Materials and Solar Cells, 2000. **62**(3).

32. S.M.Sze, *Semiconductor Devices: Physics and Technology*, 1985, John Wiley & Sons. p. 320.

33. solar-is-future.com. *How Photovoltaics Work: From Light to Electricity*. 2012 [cited 2012 11/05]; Available from: http://www.solar-is-future.com/solar-energy-source/how-photovoltaics-work/from-light-to-electricity/index.html.

34. A.B.Banful, A.Liu, and E.Rodriguez. *How a solar cell works*. 2002 [cited 2012 11/06]; Available from: http://stuff.mit.edu/afs/athena.mit.edu/course/3/3.082/www/team2_f02/Pages/background.html.

35. *Key Solar Cell Parameters and Measurement Techniques*. 2012 [cited 2012 11/06]; Available from: http://www.keithley.nl/solar_cell.

36. M.A.Green, *Solar Cells: Operating Principles, Technology, and System Applications* 1982, New Jersey: Prentice-Hall.

37. M.Born and E.Wolf, *Principles of Optics*, 1999, Cambridge University Press. p. 1-3.

38. M.Born and E.Wolf, *Principles of Optics*, 1999, Cambridge University Press. p. 11.

39. M.Born and E.Wolf, *Principles of Optics*, 1999, Cambridge University Press. p. 14-25.

40. *A representation of a plane wave's electric field shown from an oblique angle.* 2010 [cited 2012 11/05]; Available from: http://commons.wikimedia.org/wiki/File:Plane_Wave_Oblique_View.jpg.

41. M.Born and E.Wolf, *Principles of Optics*, 1999, Cambridge University Press. p. 38-40.

42. *Diagram of reflection and refraction*. 2012 [cited 2011 11/06]; Available from: http://www.glossary.oilfield.slb.com/DisplayImage.cfm?ID=255.

43. M.Born and E.Wolf, *Principles of Optics*, 1999, Cambridge University Press. p. 40-43.

44. M.Born and E.Wolf, *Principles of Optics*, 1999, Cambridge University Press. p. 49-53.

45. M.Born and E.Wolf, *Principles of Optics*, 1999, Cambridge University Press. p. 736.

46. M.Born and E.Wolf, *Principles of Optics*, 1999, Cambridge University Press. p. 737.

47. M.Born and E.Wolf, *Principles of Optics*, 1999, Cambridge University Press. p. 739-749.

48. A.S.Glassner, *An Introduction to Ray tracing* 1989: Morgan Kaufmann.

49. W.J.Smith, *Modern Optical Engineering*. 4 ed2008: McGraw-Hill.

50. B.Sopori, *PV Optics: A software package for solar cell and module design*, in *Optical Modeling and Measurements for Solar Energy Systems*2007, SPIE: San Diego, CA. p. 665206

51. *Ray-Tracing*. 2012 [cited 2012 11/06]; Available from: http://www.ice.rwth-aachen.de/research/tools-projects/grace/ray-traycing/.

52. F.J.Beck, A.Polman, and K.R.Catchpole, *Tunable light trapping for solar cells using localized surface plasmons.* Journal of Applied Physics, 2009. **105**(11): p. 114310- 114317.

53. A.W.Smith and A. Rohatgi, *Raytracing analysis of the inverted pyramid texturing geometry for high efficiency silicon solarcells.* Solar Energy Materials and Solar Cells, 1993. **29**(1): p. 37–49.

54. M.A.Green, *Lambertian Light Trapping in Textured Solar Cells and Light-Emitting Diodes: Analytical Solutions.* Prog. Photovolt: Res. Appl. , 2002. **10**: p. 235–241.

55. P.Campbell and M.A.Green, *Light trapping properties of pyramidally textured surfaces.* Journal of Applied Physics, 1987. **62**: p. 243.

56. B.L.Sopori, et al., *Light-Trapping in a-Si Solar Cells: A Summary of the Results from PV Optics*, in *National Center for Photovoltaics Program Review Meeting* 1998, NREL: Denver, CO.

57. A.E.St.John, *Multiple internal reflection structure in a silicon detector which is obtained by sandblasting*, 1969: U.S. Patent No. 3,487,223.

58. O.Krumpholz and S.Maslowski, *Schnelle Photodioden mit wellenlagnenunabhangigen Demodulatonseigenschaften.* Z. Angew. Phys., 1968. **25**: p. 156.

59. B.Sopori, et al., *A new method for rapid measurement of orientations and sizes of grains in multicrystalline silicon wafers*, in *37th IEEE PVSC* 2011, IEEE: Seattle, WA. p. 001680- 001685

60. J.A.Rand and P.A.Basore, *Light-trapping in silicon solar cells-experimental results and analysis*, in *22nd IEEE PVSC*1991. p. 192-197.

61. P.Campbell, *Light trapping in textured solar-cells.* Solar Energy Materials 1990. **21**: p. 165-172.

62. P.Campbell, *Enhancement of light-absorbing from randomizing and geometric textures.* J. Opt. Soc. Am. B, 1993. **10**: p. 2410-2415.

63. P.Campbell and M.A.Green, *High performance light trapping textures for monocrystalline silicon solar cells.* Solar Energy Materials and Solar Cells, 2001. **65**: p. 369-375.

64. V.Y.Yerokhov, et al., *Cost-effective methods of texturing for silicon solar cells.* Solar Energy Materials and Solar Cells, 2002. **72**: p. 291-298.

65. J.D.Hylton, A.R.Burgers, and W.C.Sinke, *Light trapping in alkaline texture etched crystalline silicon wafers*, in *16th European Photovoltaic Solar Energy Conference*, H. Scheer, et al., Editors. 2000: Glasgow, UK. p. 1434-1437.

66. J.W.Mueller, A.Metz, and R.Hezel. *A new and simple approach for fabricating inverted pyramids on crystalline silicon solar cells*. in *17th European Photovoltaic Solar Energy Conference*. 2001. Munich.

67. P.Panek, M.Lipinski, and J.Dutkiewicz, *Texturization of multicrystalline silicon by wet chemical etching for silicon solar cells.* Journal of Material Science, 2005. **40**(6): p. 1459-1463.

68. D.R.Turner, *Electropolishing of siilcon in hydroflouric acid solutions.* Journal of the Electrochemical Society, 1958. **105**: p. 402-408.

69. B.Schwartz and H.Robbins, *Chemical etching of silicon, Part I, The system HF, HNO_3, H_2O, $HC_2H_3O_2$.* Journal of Electrochemical Society, 1959. **106**(6): p. 505-508.

70. K.E.Bean, *Anisotropic etching of silicon* Electron Devices, IEEE Transactions, 1978. **25**(10): p. 1185-1193.

71. P.J.Holmes, *The Electrochemistry of Semiconductors*, 1962, Academic Press: London. p. 329.

72. W.L.Bailey, et al., *Texture Etching of Silicon: Method*, 1979: U.S. Patent No. 4,137,123.

73. H.Seidel, et al., *Anisotropic Etching of Crystalline Silicon in Alkaline Solutions I. Orientation Dependence and Behavior of Passivation Layers.* Journal of Electrochemical Society, 1990. **137**(11): p. 3612-3626.

74. P.Papet, et al., *Pyramidal texturing of silicon solar cell with TMAH chemical anisotropic etching.* Solar Energy Materials and Solar Cells, 2005. **90**(15): p. 2319–2328.

75. A.J.Nijdam, et al., *Etching of silicon in alkaline solutions: a critical look at the {111} minimum.* Journal of Crystal Growth, 1999. **198/199**: p. 430-434.

76. *Theory, technology, diagnostics and application of silicon solar cells*. [cited 2012 11/10]; Available from: http://cellstester.narod.ru/technology_en.html.

77. C.Honsberg and S.Bowden. *Surface Texturing*. [cited 2012 11/08]; Available from: http://www.pveducation.org/pvcdrom/design/surface-texturing.

78. E.D.Palik, H.F.Gray, and P.B.Klein, *A Raman Study of Etching Silicon in Aqueous KOH.* J. Electrochem. Soc. , 1983. **130**: p. 956-959.

79. V.A.Burrows, et al., *Infrared spectroscopy of Si (111) surfaces after HF treatment: hydrogen termination and surface morphology.* Appl. Phys. Lett., 1998. **53**: p. 998-1000.

80. G.S.Higashi, et al., *Ideal hydrogen termination of the Si (111) surface.* Appl. Phys. Lett., 1990. **56**: p. 656-658.

81. N.Hirashita, et al., *Effects of surface hydrogen on the air oxidation at room temperature of HF-treated Si (100) surfaces.* Appl. Phys. Lett., 1990. **56**: p. 451-453.

82. R.M.Finne and D.L.Klein, *A Water-Amine-Complexing Agent System for "Etching Silicon.* J. Electrochem. Soc., 1967. **114**(9): p. 965-970.
83. E.D.Palik, V.M.Bermudez, and O.J.Glembocki, *Ellipsometric Study of OrientationDependent Etching of Silicon in Aqueous KOH.* J. Electrochem. Soc. (Solid-State Science & Technology), 1998. **132**: p. 871-884.

84. W-J.Cho, W-K.Chin, and C-T.Kuo, *Effect of alcoholic moderators on anisotropic etching of silicon in aqueous potassium hydroxide solutions.* Sensors and Actuators A: Physical, 2004. **118**(2): p. 357-368.

85. J.B.Price, *Anisotropic Etching of Silicon with KOH-H_20-Isopropyl Alcohol*. Semiconductor Silicon, ed. R.R. Burfess and H.R. Huff1973, Princeton, NJ: The Electrochemical Society Softbound Proceedings Series.

86. J.D.Hylton, *Light coupling and light trapping in alkaline etched multicrystalline silicon wafers for solar cells*, in *Department of Physics* 2006, Universitiet Utrecht: Netherlands.

87. Z-f.Zhou, et al., *A cellular automaton-based simulator for silicon anisotropic etching processes considering high index planes.* J. Micromech. Microeng., 2007. **17**: p. S38–S49.

88. B.Mills, *Ball-and-stick model of the unit cell of silicon*, Silicon-unit-cell-3D-balls.png, Editor 2007, Wikipedia: USA.

89. P.Maycock, Renewable Energy World, 2003. **7**(PV marked update): p. 84-111.

90. D.L.King and M.E.Buck, *Experimental Optimisation of an Anisotropic Etching Process for Random Texturisation of Silicon Solar Cells*, in *22nd IEEE PVSC*1991. p. 303-308.

91. R.Einhaus, et al., *Isotropic texturing of multicrystalline silicon wafers with acidic texturing solutions*, in *26th IEEE PVSC*1997: Anaheim. p. 167-170.

92. M.J.Stocks, A.J.Carr, and A.W.Blakers, *Texturing of polycrystalline silicon*, in *1st WCPEC*1994: Hawaii. p. 1551-1554

93. M.J.Stocks, A.J.Carr, and A.W.Blakers, *Texturing of polycrystalline silicon.* Solar Energy Materials and Solar Cells, 1996. **40**: p. 33-42.

94. H.Robbins and B.Schwartz, *Chemical Etching of Silicon: II . The System HF, HNO_3, H_2O, and $HC_2H_3O_2$.* J.Electrochem. Soc., 1960. **107**(2): p. 108-111

95. B.Schwartz and H.Robbins, *Chemical Etching of Silicon: III . A Temperature Study in the Acid System.* J. Electrochem. Soc., 1961. **108**(4): p. 365-372.

96. B.Schwartz and H.Robbins, *Chemical Etching of Silicon: IV . Etching Technology.* J. Electrochem. Soc., 1976. **123**(12): p. 1903-1909.

97. S.Zhou, et al., *Experimental study on the elimination of over-plating problems in industrial manufacturing of large-area acidic-textured laser-doped multicrystalline solar cells.* Solar Energy Materials and Solar Cells, 2013. **108**: p. 44-49.

98. T.Nunoi, et al., *Cast polycrystalline silicon solar cell with grooved surface*, in *21st IEEE PVSC*1990: Kissimmee p. 664-665.

99. G.Willeke, et al., *A simple and effective light trapping technique for polycrystalline silicon solar cells.* Solar Energy Materials and Solar Cells, 1992. **26**: p. 345-356.

100. H.Nakaya, et al., *Polycrystalline silicon solar cells with V-grooved surface.* Solar Energy Materials and Solar Cells, 1994. **34**: p. 219-225.

101. Y.Hayashi, et al., in *10th EC PVSEC* 1991, Kluwer Academic Publishers: Lisbon. p. 254.

102. M.B.Rabha, et al., *Optoelectronic enhancement of monocrystalline silicon solar cells by porous silicon-assisted mechanical grooving.* Phus. Status Solidi C, 2011. **8**(3): p. 887-890.

103. W.A.Nositschka, et al., *Texturisation of multicyrstalline silicon wafers for solar cells by reactive ion etching through colloidal masks.* Solar Energy Materials & Solar Cells, 2003. **76**: p. 155-166.

104. H.Jansen, et al., *A survey on the reactive ion etching of silicon in microtechnology.* J. Micromech. Microeng., 1996. **6**: p. 14-28.

105. H.Jansen, et al., *The black silicon method: a universal method for determining the parameter setting of a fluorine-based reactive ion etcher in deep silicon trench etching with profile control.* J. Micromech. Micoreng. , 1995. **5**: p. 115-120.

106. A.R.Burgers and J.H.Bultman, *SIlicon Solar Cells Textured By Reactive Ion Etching With Natural Lithography*, in *16th European Photovoltaic Solar Energy Conference and Exhibition*2000: Glasgow.

107. *Dry etching*. [cited 2012 11/10]; Available from: https://http://www.mems-exchange.org/MEMS/processes/etch.html.

108. H.F.Winters, *The role of chemisorption in plasma etching.* J. Appl. Phys. , 1978. **49**: p. 5165-5170.

109. K.-s.Lee, et al., *Damage-free reactive ion etch for high-efficiency large-area multi-crystalline silicon solar cells.* Solar Energy Materials and Solar Cells, 2011. **95**(1): p. 66–68.

110. G.Willeke and P.Faith, *Texturisation methods for multicrystalline silicon solar cells*, in *13th EPVSEC*1995: Nice. p. 399-402.

111. J.C.Zolper, et al., *Applied Physics Letters.* 16.7% efficient, laser textured, buried contact, polycrystalline silicon solar cell, 1989. **55**(22): p. 2363-2365.

112. M.Abbott and J.Cotter, *Optical and Electrical Properties of Laser Texturing for High-efficiency Solar Cells.* Prog. Photovolt: Res. Appl., 2006. **14**: p. 225-235.

113. B.K.Nayak, V.V.Iyengar, and M.C.Gupta, *Efficient light trapping in silicon solar cells by ultrafast-laser-induced self-assembled micro/nano structures.* Prog. Photovolt: Res. Appl., 2011. **19**: p. 631-639.

114. T-H.Her, et al., *Microstructuring of silicon with femtosecond laser pulses.* Appl. Phys. Lett., 1998. **73**(12): p. 1673-1675.

115. A.J.Pedraza, J.D.Fowlkes, and D.H.Lowndes, *Silicon micro-column arrays grown by nanosecond pulsed-excimer laser irradiation.* Appl. Phys. Lett., 1999. **74**(16): p. 2322-2324.

116. B.K.Nayak, M.C.Gupta, and K.W.Kolasinski, *Ultrafast-laser-assisted chemical restructuring of silicon and germanium surfaces.* Applied Surface Science, 2007. **253**(15): p. 6580-6583.

117. M.Halbwax, et al., *Micro and nano-structuration of silicon by femto-secon laser: application to silicon photovoltaic cells fabrication.* Thin Solid Films, 2008. **516**(20): p. 6791-6795.

118. M.D.Abbott, et al., *Laser-induced defects in crystalline silicon solar cells*, in *31st IEEE Photovoltaic Specialist Conference*January 2005: Orlando. p. 1241-1244.

119. K-R.Kima, et al., *UV laser direct texturing for high efficiency multicrystalline silicon solar cell.* Applied Surface Science, 2012.

120. *Using Nanotechnology to Improve Performance of Solar Cell*. 2008 [cited 2012 10/11]; Available from: http://www.azonano.com/news.aspx?newsID=7055.

121. M.A.Green, in *High Efficiency Solar Cells* 1987, Trans Tech: Aedermannsdorf, Switzerland/Brookfield, VT. p. 70.

122. J.Nelson, in *The Physics of Solar Cells* 2003, Imperial College: London. p. 279 and 282.

123. E.Hecht, *The Diffraction Grating*, in *Optics*1998, Addison Wesley Longman: Reading, MA. p. 465.

124. C.Heine and R.H.Morf, *Submicrometer gratings for solar energy applications.* Applied Optics, 1995. **34**(14): p. 2476-2482.

125. C.Eisele, E.Nebel, and M.Stutzmann, *Periodic light coupler gratings in amorphous thin film solar cells.* J. Appl. Phys., 2001. **89**: p. 7722-7726.

126. F.Llopis and I.Tobías, *The role of rear surface in thin silicon solar cells.* Solar Energy Materials and Solar Cells, 2005. **87**(1-4): p. 481-492.

127. J.D.Joannopoulos, et al., *Photonic Crystals: Modelling the Flow of Light*. 2nd ed2007, Princeton and Oxford: Princeton University Press.

128. E.Yablonovitch, *Inhibited Spontaneous Emission in Solid-State Physics and Electronics* Physical Review Letters, 1987. **58**(20): p. 2059-2062.

129. S.John, *Strong localization of photons in certain disordered dielectric superlattices.* Physical Review Letters, 1987. **58**(23): p. 2486–2489.

130. R.B.Wehrspohn and J.Upping, *3D photonic crystals for photon management in solar cells.* J. Opt. , 2012. **14**: p. 024003 (9pp).

131. D.C.Johnson, et al., *Advances in Bragg stack quantum well solar cells.* Solar Energy Materials and Solar Cells, 2005. **87**(1-4): p. 169-179.

132. M.Z.Shvarts, et al., *Radiation resistant AlGaAs/GaAs concentrator solar cells with internal Bragg reflector.* Solar Energy Materials and Solar Cells, 2001. **68**(1): p. 105-122.

133. L.Zeng, et al., *Efficiency enhancement in Si solar cells by textured photonic crystal back reflector.* Appl. Phys. Lett., 2006. **89**(11): p. 111111-111113.

134. *Enhancement of Spontaneous Emission in Microcavities*, in *Vertical-Cavity Surface-Emitting Lasers: Design, Fabrication, Characerization, and Applications*, C.W. Wilmsen, H. Temkin, and L.A. Coldren, Editors. 1999, Cambridge University Press: Cambridge. p. 72.

135. P.Bermel, et al., *Improving thin-film cyrstalline silicon solar cell efficiencies with photonic crystals.* Optics Express, 2007. **15**(25): p. 16986-14000.

136. S.Nie and R.Emory, *Probing single molecules and single nanoparticles by surface-enhanced Raman scattering.* Science, 1997. **275**: p. 1102-1106.

137. M.Moskovits, *Surface-enhanced spectroscopy.* Rev. Mod. Phys., 1985. **57**(3): p. 783-826.

138. H.R.Stuart and D.G.Hall, *Island size effect in nanoparticle-enhanced photodetectors.* Appl. Phys. Lett., 1998. **73**(26): p. 3815-3817.

139. D.M.Schaadt, B.Feng, and E.T.Yu, *Enhanced semiconductor optical absorption via surface plasmon excitation in metal nanoparticles.* Appl. Phys. Lett., 2005. **86**(6): p. 063106-063108.

140. D.Derkacs, et al., *Improved performance of amorphous silicon solar cells via scattering from surface plasmon polaritons in nearby metallic nanoparticles.* Appl. Phys. Lett., 2006. **89**(9): p. 093103-093105.

141. M.A.Green and S.Pillai, *Harnessing plasmonics for solar cells.* Nature Photonics, 2012. **6**: p. 130–132.

142. H.Dai, et al., *Effective light trapping enhancement by plasmonic Ag nanoparticles on silicon pyramid surface.* Optics Express, 2012. **7**(9): p. A502-A509.

143. K.R.Catchpole and A.Polman, *Plasmonic solar cells.* Optics Express, 2008. **16**(26): p. 21793-21800.

144. D.A.Clugston and P.A.Basore, *PC1D version 5: 32-bit solar cell modeling on personal computers*, in *26th IEEE PVSC* 1997: Anaheim, CA. p. 207-210.

145. R.Stangl, M.Kriegel, and M.Schmidt. *AFORS-HET, Version 2.2, A numerical Computer Program for Simulation of Heterojunction Solar Cells and Measurements*. in *Photovoltaic Energy Conversion, Conference Record of the 2006 IEEE 4th World Conference* 2006. IEEE.

146. R.Stangl, C.Leendertz, and J.Haschke, *Numerical simulation of solar and solar cell characterization methods: the open source on demand program*

AFORS-HET, in *Solar Energy, INTECH*, R.D.Rugescu, Editor 2010: Croatia. p. 319-352.\

147. D.Thorp and S.R.Wenham, *Ray-tracing of arbitrary surface textures for light-trapping in thin silicon solar cells.* Solar Energy Materials and Solar Cells, 1997. **48**: p. 295-301.

148. R.Brendel. *SUNRAYS: A versatile ray tracing program for photovoltaic community*. in *12th EPVSEC*. 1994. Amsterdam.

149. A.W.Smith, A.Rohatgi, and S.C.Neel, *Texture: A ray tracing program for the photovoltaic community*, in *21st IEEE PVSC*1990, IEEE: Kissimmee, FL. p. 426-43.

150. CROSSLIGHT. *APSYS*. 2011 [cited 2012 11/11]; Available from: http://crosslight.com/products/apsys.shtml.

151. Z.Q.Li, Y.G.Xiao, and Z.S.Li. *Modeling of multi-juntion solar cells by Crosslight APSYS*. in *SPIE*. 2006.

152. D.Redfield, *Multiple-pass thin-film silicon solar cell.* Appl. Phys. Lett., 1974. **25**(11): p. 647-648.

153. E.Yablonovitch, *Statistical ray optics.* Opt. Soc. Am., 1982. **72**(7): p. 899-907.

154. R.J.Roedel and P.M.Holm, *The design of anisotropically etched III-V solar cells.* Solar cells, 1984. **11**(3): p. 221-239.

155. A.Wang, J.Zhao, and M.A.Green, *24% efficient silicon solar cells.* Appl. Phys. Lett., 1990. **57**(6): p. 602-604.

156. R.Brendel, *Coupling of light into mechanically textured silicon solar cells: A ray tracing study.* Prog. Photovolt: Res. Appl., 1995. **3**(1): p. 25-38.

157. D.O.E., U.S. *Industry Awards*. 2012 [cited 2012 11/11]; Available from: www1.eere.energy.gov/solar/sunshot/accomplishments.html.

158. B.L.Sopori, et al., *Modeling Emissivity of Rough andTextured Silicon Wafers.* Journal of Electronic Materials, 1998. **27**(12): p. 1341-1346.

159. Y.Nishimoto, T.Ishihara, and K.Namba, *Investigation of Acidic Texturization for Multicrystalline Silicon Solar Cells.* J. Electrochem. Soc., 1999. **146**(2): p. 457-461.

160. J.M.Rodriguez, I.Tobias, and A.Luque, *Random pyramidal texture modelling.* Solar Energy Materials and Solar Cells, 1995. **45**(3): p. 241-253.
161. S.C.Baker-Finch and K.R.McIntosh, *Reflection of normally incident light from silicon solar cells with pyramidal texture.* Prog. Photovolt: Res. Appl., 2011. **19**(4): p. 406-413.

162. B.Sopori, et al., *An Optical Technique for Measurement of Grain Orientation and Sizes in Multicrystalline Silicon Wafers. (Manuscript submitted for publication).* 2012.

163. H.Seager, C., *Grain boundary recombination: Theory and experiment in silicon.* J. Appl. Phys., 1981. **52**(6): p. 3960-3968.

164. B.D.Cullity and S.R.Stock, *Elements of X-Ray Diffraction*. 3rd ed2001: Prentice Hall.

165. G.Arfken, *Mathematical Methods for Physicists* 3rd ed1985, Orlando, FL: Academic Press.

166. A.Taflove, *Computational Electrodynamics: The Finite-Difference Time-Domain Method*. 3rd ed2005, Norwood, MA: Artech House.

167. P.Spinelli, et al., *Plasmonic anti-reflection coating for thin film solar cells*, in *Optical Nanostructions for Photovoltaics*2010, Optical Society of America: Karlsruhe, Germany.

168. J.Lacombe, et al., *Optical modeling of light trapping in thin film silicon solar cells using the FDTD method*, in *35th IEEE PVSC*2010: Honolulu, HI. p. 001535-001539.

169. J.Buencuerpo, et al., *3D-FDTD analysis of absorption enhancement in nanostructured thin film solar cells*, in *Optical Nanostructures and Advanced Materials for Photovoltaics*2011, Optical Society of America: Austin, TX.

170. C-H.Poh, et al., *FDTD modeling to enhancethe performance of an organic solar cell emedded with gold nanoparticles.* Optical Materials Express, 2011. **1**(7): p. 1326-1331.

171. P.T.Kuruganti and J.Nutaro, *A comparative study of wireless propagation smulation methodologies: Ray tracing, GDTD, and event based TLM*, in *Huntsville Simulation Conf.*2006.

172. *Solar Energy 101: Introduction to Solar Energy*. 2012 [cited 2012 11/30]; Available from: http://www.dowcorning.com/content/solar/solarworld/solar101.aspx.